DEPARTAMENTO DE INGENIERÍA DE SISTEMAS Y AUTOMÁTICA
ESCUELA SUPERIOR DE INGENIERÍA
UNIVERSIDAD DE SEVILLA

Modelling and Control of Aerial Manipulators

por

Antonio Enrique Jiménez Cano

Ingeniero en Automática y Electrónica Industrial

PROPUESTA DE TESIS DOCTORAL
PARA LA OBTENCIÓN DEL TÍTULO DE

DOCTOR POR LA UNIVERSIDAD DE SEVILLA

SEVILLA, 2019

Directores

Dr.-Ing. Guillermo Heredia Benot, Catedrático

Dr.-Ing. Aníbal Ollero Baturone, Catedrático

UNIVERSIDAD DE SEVILLA

Memoria para optar al grado de Doctor por la Universidad de Sevilla

Autor: **Antonio Enrique Jiménez Cano**

Título: **Modelling and Control of Aerial Manipulators**

Departamento: **Departamento de Ingeniería de Sistemas y Automática**

V° B° Director:

Guillermo Heredia Benot

V° B° Director:

Aníbal Ollero Baturone

El autor:

Antonio Enrique Jiménez Cano

I try to pin her down
but she's always on the run
I wanna catch her
but I can't slow her down

Abstract

Born in the last years inside the aerial robotics field, aerial manipulation is a topic whose impact has been increasing day by day. The reason is the large number of new applications that could be developed with these robotics systems. An aerial manipulation system consists of an aerial platform equipped with one or several robotic arms. This concept opens up many new applications and possibilities for aerial robots. Furthermore, the possibility to carry out autonomously industrial and infrastructure inspections and assembly tasks at locations that are difficult to access has fostered the interest of the research community and the public for these robots.

This thesis focuses on the study of aerial manipulation systems and, particularly in the design of a control strategy for the aerial platform of these aerial systems. Thanks to mathematical models of the system dynamics, the aerial manipulator behaviour can be analysed when robotic arms carry out manipulation tasks, allowing the development and implementation of control techniques for these systems. The aim of this thesis has been not only the design of control techniques but also the implementation in real aerial manipulation system with the capability to carry out manipulation tasks in outdoor scenarios. This aim involves the study of the hardware needed and even, in one application, the mechanical design and implementation of a compliant arm, moreover the development of its controller.

The main contribution of this thesis is the study of the dynamic model for different kinds of aerial manipulator systems, and especially the analysis of these dynamics and the development of controllers to carry out manipulation tasks, while the system stability is guaranteed. To achieve it, the mechanical design of the different prototypes has been implemented, thanks to the study of the hardware specifications needed

for each particular application case. Prototypes for assembly tasks and structure inspection have been developed having into account the final goals for each application and the scenario in which it has been tested. The validation of the proposed methods and applications have been accomplished by the design of tests in outdoor scenarios, analysing in detail each experiment result to correct mistakes and to adapt or add any structural or hardware modification needed.

Resumen

Hace unos años, dentro de la robótica aérea, surgió la manipulación aérea como campo de investigación. Desde su nacimiento, su impacto ha ido incrementándose poco a poco debido, sobretodo, al gran número de aplicaciones que podrían llevarse a cabo con este tipo de sistemas. Un manipulador aéreo puede definirse como una plataforma aérea la cual ha sido equipada con uno o varios brazos robóticos. Este nuevo concepto ha abierto un mundo de posibilidades para este tipo de robots aéreos. Además, gracias a la posibilidad de este tipo de robots aéreos de interactuar con su entorno, podrían llevar a cabo inspecciones de estructuras civiles o incluso, tareas de ensamblaje de estructuras y todo ello, por supuesto, de forma autónoma.

Esta tesis se centra en el estudio e implementación de sistemas de manipulación aérea y, en particular, en el diseño de estrategias de control para la plataforma aérea. Este estudio comienza con el cáculo de las ecuaciones que representan la dinámica del sistema, y que nos permite analizar su comportamiento y la influencia del movimiento de los brazos robóticos en la estabilidad de la plataforma.El análisis de estas ecuaciones nos permite diseñar de esquemas de control tales como los basados en Backstepping. Pero el objetivo de esta tesis no es solo el diseño sino también la implementación de estas técnicas de control en sistemas de manipulación aérea reales y con capacidad de llevar a cabo tareas de manipulación en escenarios al aire libre.

La principales contribuciones de esta tesis son el cálculo de los modelos dinámicos para cada uno de los tipos de manipuladores aéreos estudiados he implementados durante el desarrollo de la tesis. Además del uso de estas modelos para la diseño de una estrategia de control adaptable a cada una de las plataformas. También se ha diseñado un mecanismo compliant que ha sido integrado en un manipulador para

llevar a cabo tareas de inspección estructuras por contacto, además de un control de fuerza-posición.

Cada manipulador aéreo implementado durante esta tesis, excepto el en caso del helicóptero, va unido a un estudio de las especificaciones hardware necesarias para la realización de una validación del sistema mediante experimentos de vuelo en escenarios al aire libre, y en el caso de los manipuladores aéreos para inspección de estructuras, en un puente real. Cada experimento realizado ha sido analizado en detalle para corregir errores, además de para adaptar o agregar cualquier modificación estructural o de hardware necesaria.

Acknowledgment

First of all, I would like to thank my supervisors and mentors Prof. Guillermo Heredia and Prof. Anibal Ollero, for their guidance and support all along this thesis. In particular,I would like to express my deep gratitude and admiration to Prof. Guillermo Heredia for the personal teaching and time spent in this work.

I also express my sincere gratitude to all my colleagues, professors and friends in the Robotics, Vision and Control Group. I would like with special affection to express my gratitude to Fran Real, Victor Vega, Arturo Torres, Pedro Sanchez, Manuel Fernandez, Rafa Salmoral (the "bossi"), María Polvillo, Alejandro Suarez, Ángel Rodríguez, Rebeca Pérez, Alejandro Sánchez, Honorio Romero, Agustín Ramos and Dimas Fuego. In addition, I wish to acknowledge Juan Braga and Jesús Martin for their helpful, friendship and passion for burgers.

A very special thanks go to Ainhoa (this adventure started with you), Riki (my partner and friend), The Ezkorpiants (my friends forever and ever), the Pauleles (my Seville family) and Almudena (my happiness, my strength).

Finally, I also would like to thank my family for the support and love they provided me through my entire life.

This work, developed within the Robotics, Vision and Control Group at the University of Seville (Spain), has been funded by the FP7 ARCAS and H2020 AEROBI European Projects, and by the AEROMAIN (DPI2014-5983-C2-1-R) and the AEROCROS (DPI2015-71524-R) Spanish projects.

Acronyms

eSRA European Robotics Strategic Research Agenda

DoF Degrees of Freedrom

EKF Extended Kalman Filter

GPS Global Positioning System

IMU Inertial Measurement Unit

LAN Local Area Network

MAV Micro Aerial Vehicle

OS Operating System

POE Product of Exponentials

RC Radio Controlled

ROS Robot Operating System

RO-SLAM Range-Only Simultaneous Localization and Mapping

UAS Unmanned Aerial System

UAV Unmanned Aerial Vehicle

GCS Gound Control Station

CATEC Center for Advanced Aerospace Technologies

CoG Center of Gravity

PCM Passive Compliance Mechanism

PLA Polylactic Acid

ABS Acrylonitrile Butadiene Styrene

PFI Potential FLow with the method of images

TRL Technology Readiness Level

DH Denavit-Hartenberg

SHCS Shared Memory Communication System

Contents

List of Figures

Chapter 1

Introduction

1.1 Introduction to Aerial Manipulation

In the research community, the interest in unmanned aerial vehicles and the possibilities of its applications have been increasing during the last decade. The demonstrations of UAVs capabilities have resulted in the addition of industrial companies to this interest and therefore, the growth of investment for the development of this technology. One example is the idea launched by an famous commerce company to use UAVs for parcel delivery to their customers (Amazon, 2016), or the increasingly frequent use in the cinema and television industry and the widening number of business related to the sale of these aerial robots. Therefore, applications are continually emerging: monitoring and inspection of civilian infrastructures, helping in the agriculture to pest surveillance or in the rescue of survivors in natural disasters (GeoSocial, 2014), or even archaeologists have used UAVs to digitally reconstruction of medieval towns (Mattino, 2014). UAVs are popular inside the public opinion and, we could affirm that it is the golden period of the aerial robotics.

In the last years, UAVs are also experiencing an evolution. UAVs have been commonly used in passive tasks like surveillance, inspection, monitoring or remote sensing; Recently, active tasks like grasping and assembling have been also joined to these skills thanks to the development of prototypes with manipulation and environment interaction capabilities. In fact, According to the European Robotics

Strategic Research Agenda (eSRA)(for Robotics in Europe, 2013) aerial robots have to be endowed with manipulation skills to done grasping, transporting, assembly and disassembly of mechanical parts, etc; with the intent in a near future, to be employed as robotics workers, robots for exploration and inspection or logistic. These new UAVs capabilities can be helpful in those jobs that are considered dangerous for a human operator, whether to carry out these activities or, at least, to assist in hazardous and critical situations.

As a result of to endow UAVs with manipulation and environment interaction skills, the *aerial manipulation* has emerged as a new robotic research field. This field proposes the integration between a vertical take-off and landing (VTOL) unmanned aerial vehicles (multirotors or helicopters) and a tool to perform manipulation tasks in the air. According to (Ruggiero et al., 2018), the most adopted solutions are a *flying hand*(FH) or an *unmanned aerial manipulator*(UAM):

A. Flying Hands

A FH is an aerial vehicle equipped with a gripper or a multi-finger hand that can be directly attached to the UAV or using some cables or tether mechanism. In this case, the robot can grasp and manipulate an object when it is flying. However, the robot tasks are limited to transport objects or performing contacts with surfaces and this is not enough to carry out active tasks. From a theoretical point of view, (Nguyen et al., 2015) demonstrates that for the system stabilization, it is better a gripper positioned above the aerial vehicle.However, most studies presented in bibliography show the gripper placed below the aerial vehicle. The reason is that to grasp an object, it is easier to do it from the top. Furthermore, to maximize the payload of the system, it is convenient to design low-complexity grippers with light-weight. In (Mellinger et al., 2011) and (Lindsey et al., 2011), the designs of two kinds (impactive and ingressive) of light-weight and low-complexity grippers are presented. The grippers are attached to quadrotors to grasp and perch on branches or beams and pick up and transport payloads. In particular, in (Lindsey et al., 2011), a team of these FHs is used to carry out the construction of a cubic structure in a coordinated manner. FH are also designed and used with helicopters. (Backus et al., 2014) presents the Yale Aerial Manipulator. It is a robot hand placed directly on the bottom of a helicopter. The

design presented uses an actuator per finger and studies the impact of external forces in the palm and grasping efficiency for different object sizes depending on the palm size. In (Pounds et al., 2011), the Yale Aerial Manipulator is used to analyse the disturbances due to the load mass and its position concerning to the prototype center of gravity and experiments grasping objects while hovering.

A FH can be also considered as a UAV equipped with a tool to interact with the environment. For example, (Nguyen and Lee, 2013) presents a hybrid force/motion control framework multirotors with rigid/light tool attached to it. Furthermore, in (Bellens et al., 2012) hybrid pose / wrench control framework for quadrotor helicopters, allowing direct contact of the quadrotor with its environment and stable motion while in contact was presented. The design of a tri-tiltrotor aerial manipulator for forceful interaction is presented in (Papachristos et al., 2014). This prototype can hold an end effector in contact with a surface while hovering. Application examples have been also presented, i.e, a prototype with perching and door-opening capability is presented in (Tsukagoshi et al., 2015) and another example can be seen in (Darivianakis et al., 2014), this case was designed for inspection operations by contact.

Figure 1.1: Example of a FH for bridge inspection by contact developed at the University of Seville within the AEROBI-project.

The aerial manipulators in which the objects are transported through cables or tether mechanism are considered as FHs as well. (Cruz and Fierro, 2014) addresses the problem of lifting from the ground a cable-suspended load by a quadrotor aerial vehicle considering that the mass is unknown. The behavior of a helicopter linked to the

ground through a cable is studied in (Sandino et al., 2016). The challenge of a tethered aerial robot taking off and landing on slopes surfaces is presented in (Tognon et al., 2016), analysing the safe and manoeuvre conditions. The dynamics model for tethered aerial robots is studied in (Tognon and Franchi, 2017), furthermore, they propose two nonlinear control for smooth trajectories based on the differential flatness properties of the system. In (Bernard et al., 2011), a system composed of multiple aerial robots cooperate in search and rescue missions. The outdoor experiments presented in this work shown autonomous helicopters transporting loads through cables to assist victims during a rescue phase operation. Another example of multiple tethered UAVs cooperating to manipulate and transport objects is shown in (Michael et al., 2011) and (Fink et al., 2011). Using Newton-Euler recursive method, in (Sreenath and Kumar, 2013), the dynamics model of multiple quadrotors cooperating to transport a payload suspended by cables is derived and using the differential flatness property of the system, they find dynamically feasible trajectories for the system formed by both payload and quadrotors. (Palunko, 2012) is textbook showing the last advances in control and planning trajectory of UAVs with suspended loads.

B. Unmanned Aerial Manipulator

The second case mentioned above is the UAM. In an UAM, an aerial vehicle is equipped with one or more robotic arms. This solution provides to the aerial vehicle with the capability of performing dexterous manipulation tasks and, therefore, to accomplish more complex actions than with a simple gripper. The design of an efficient UAM represents a difficult challenge. In bibliography there can be found several solution approaches to solve the problem of equipping an aerial vehicle with one or multiple robot arms. Moreover, there are examples of UAM mounting commercial and custom robots arms. In (Heredia et al., 2014), a coaxial octocopter is equipped with a 7-DoF commercial arm model *Robai Cyton gamma 1500* to accomplish grasping task. Other approach using commercial arm can be found in (Huber et al., 2013) wherein a 7-DoF anthropomorphic robot manipulator like the *KUKA LWR* is mounted in a helicopter. Alternatively, there are also cases in which researchers have chosen to develop their own robot arms. This option can be desirable because of the most commercial robot arm are too heavy to be mounted in a multirotor. Which could

reduce the time flight or have to use an oversized aerial platform and, that fact would affect the system operability in real scenarios. In (Kim et al., 2013), the authors design and develop an aerial manipulator consisting in a 2-DoF robot arm mounted in a quadrotor, showing autonomous flight experiments picking and delivering an object, with the purpose of validating the sliding mode controller proposed. In (Jimenez-Cano et al., 2013) an innovative backstepping-based control for aerial manipulators was tested in flight with a lightweight prototype formed by a quadrotor equipped with a 3-DoF robot arm which links were built from polymer powder by Rapid Manufacturing. In (Cano et al., 2013), the mechanical design of a 6-DoF lightweight manipulator for assembling bar structures is presented. This arm prototype was specifically designed to be mounted in a rotary-wing UAV. The robotic arm was equipped with an end-effector developed for grasping bars. Subsequently, this prototype of UAM was used in the experiments done to prove the multilayer control for aerial manipulators proposed in (Ruggiero et al., 2015). Reviewing the works mentioned above, we can focus on all of these have been designed with rotational rigid joints. Nevertheless, UAMs with prismatic joints can be also found (Forte et al., 2012) and even prototypes with compliant joints (Suarez et al., 2015).

Figure 1.2: Examples of AUMs developed for the ARCAS-project.

Additionally, in the last year, some works with UAMs with dual arms have been presented. The range of aerial manipulator operations can increase thanks to the use of a dual arm system, i. e., with the possibility to grasp heavy objects or long bars as well as to carry out a task with an arm while the other is grabbed at a point or holds a

camera to assist in the operation. Some examples of works about aerial manipulators with dual arms can be found in (Danko et al., 2015), (Suarez et al., 2017) and (Suarez et al., 2018a).

Figure 1.3: Examples of dual arm aerial manipulators developed at the University of Seville within the AEROARMS-project.(Suarez et al., 2018b)

During assembly tasks or inspection operations, the arm movements generate a displacement of the system center of mass and changes in the moments of inertia. Moreover, dynamic reaction forces and torques can appear inducing stability problems in the aerial platform. In (Pounds et al., 2012), an analysis of the stability bounds for these changes of mass is studied. In (Suarez et al., 2018b), the interactions between the arms and the platform are identified in testbench, showing the reaction torques generated. The use of redundant manipulators can be also used to planning the arm trajectories to reduce these disturbances acting over the aerial platform (Sanchez et al., 2015). Typically, two approaches are considered to handle planning and control problems for an aerial manipulator: a decentralized approach, in which the arm an the aerial platform are considered as independent systems and the coupled effects are then defined as external perturbations between each system. An example of this approach can be seen in (Ruggiero and Lippiello, 2015) in which the authors design a momentum-based observer to compensate the arm dynamics and aerodynamic effects. In the other hand, we have a centralized approach in which the aerial platform and the arm is considered as a unique system and, therefore, the solutions proposed for

planning and control are designed taken into account the full dynamics and kinematics of the system (Lippiello and Ruggiero, 2012).

The relevance of aerial manipulation in the last years is reflected in the number of European projects with the goal of advancing in this field robotics. The first European project related with aerial manipulation field was the ARCAS-project (Aerial Robotics Cooperative Assembly System,(ARCAS-project, 2013)). The project aims were the development and experimental validation of the first cooperative free-flying robot system for assembly and structure construction. Many innovative European projects have been undertaken, as a result of the ARCAS-project. With the goal of carrying out autonomous in-depth structural bridge inspections emerged the AEROBI-project (AErial RObotic System for In-Depth Bridge Inspection by Contact,(AEROBI-project, 2016)). The AEROARMS-project (AErial RObotic system integrating multiple ARMS and advanced manipulation capabilities for inspection and maintenance,(AEROARMS-project, 2016)) aims is to perform industrial inspection and maintenance tasks using aerial manipulators equipped with dual arms. Another related projects are AEROWORKS (Collaborative aerial robotic workers), (AEROWORKS-project, 2015), where the objective was to perform inspection and maintenance tasks in infrastructure environments developing aerial robotic workers that cooperate among themselves; and HYFLIERS (HYbrid FLying-rollIng with-snakE-aRm robot for contact inspection,(HYFLIERS-project, 2018)) where the objective is to design and implement hybrid robots with ground mobility and flight capability which will be equipped with a manipulator arm to inspect industrial pipelines.

1.2 Contributions of this work

This section is dedicated to review the main scientific contributions provided by this thesis. The scope of this work have been the study, analysis, develop and implementation of aerial manipulation system to carry out useful tasks in real applications. In the following, we briefly present a list of these contributions:

1. **Dynamic model of Aerial Manipulator Systems:** To obtain the dynamic equations of a mechanical system is a fundamental first step to understand its

behavior and design control methods. During this thesis, we are working with several kind of aerial manipulation prototypes. For each one its dynamic model has been derived. Depending on the case we have explored the Lagrange-Euler formalism, the Newton-Euler recursive formulation or even the Kane's method. Afterwards, this model have been used analyse the behaviour of the aerial manipulator, to develop a simulator or to design a controller.

2. **Analysis of dynamic behavior of the aerial manipulators:** Thanks to the mathematical models and real experiments done, the influence of arms movements over the aerial platform has been studied and analyzed. For example, the changes in the system inertia matrix and gravity terms when the arm is carrying out any task have been characterized in chapter 2. The analysis of these interaction in a dual-arm case has been also studied.

3. **Design of an nonlinear control method for aerial manipulator(multirotor and helicopter):** A generic non linear Backstepping-based control scheme has been proposed for aerial platforms equipped with robotic arms. This control technique has been adapted to the different aerial manipulators studied during this thesis and validated in real flight experiments.

4. **Design and implementation of a custom compliant aerial manipulator:** An passive compliance mechanism has been designed and developed. Thanks to this mechanism the torque over a joint can be estimated and it has been used to implement a 4-DoF compliant robotic arm for bridge inspection by contact. Furthermore, it allows us to develop a force position control (chapter 4).

5. **Design of a force-position controller for compliant arms:** A control technique for compliant aerial manipulator has been designed and implemented in a real system. This controller allows applying a desired force over a contact surface while rejecting the disturbance due to the natural aerial platform oscillations and holds a desired position. The controller has been designed to carry out bridge inspection by contact and has been tested through real flight experiments in a bridge.

6. **Implementation of a new full-actuated multirotor configuration:** Most common configurations for multirotors are underactuated systems and it could not be the best characteristic to perform aerial manipulation tasks. In chapter 4, we propose a new configuration in which the aerial platform can flight forward without generating any torque over roll and pitch angles.

7. **Design of a nonlinear controller to take advantage of the ceiling effect for bridge inspection by contact:** In bridge inspections, when the rotors of an aerial platform are closed to the structure surface appear an aerodynamic effect called ceiling effect. This effect can destabilize the system and even cause an accident. However it can be also profitable because it can be useful saving energy and increasing the flight time of the platform. In chapter 4, we propose and develop a nonlinear control scheme which using an analytical model of the ceiling effect can generate smooth transitions between the states of into and without contact, and even to minimize the signal thrust to save the platform energy. The solution approach has been also tested in experiments done in a real bridge.

All of these contributions are justified by the publications done during this thesis. In the next section, we present a list of these publications.

1.3 List of publications

[**1.**]AE Jimenez-Cano, J Martin, G Heredia, A Ollero, R Cano. "Control of an aerial robot with multi-link arm for assembly tasks," in 2013 IEEE International Conference on Robotics and Automation (ICRA), 4916-492.

[**2.**]G Heredia, AE Jimenez-Cano, I Sanchez, D Llorente, V Vega, J Braga, JA Acosta, A. Ollero. "Control of a multirotor outdoor aerial manipulator," in 2014 IEEE/RSJ International Conference on Intelligent Robots and Systems (IROS), 3417-3422.

[**3.**]AE Jimenez-Cano, J Braga, G Heredia, A Ollero. "Aerial manipulator for structure inspection by contact from the underside," in 2015 IEEE/RSJ international conference on intelligent robots and systems (IROS), 1879-1884.

[**4.**]AE Jimenez-Cano, G Heredia, M Bejar, K Kondak, A Ollero. "Modelling and control of an aerial manipulator consisting of an autonomous helicopter equipped with a multi-link robotic arm," in 2016 Proceedings of the Institution of Mechanical Engineers, Part G: Journal of Aerospace Engineering, Vol. 230, Num. 10, 1860-1870.

[**5.**]A Torres-Gonzalez, JR Martinez-de Dios, A Jimenez-Cano, A Ollero. "An Efficient Fast-Mapping SLAM Method for UAS Applications Using Only Range Measurements," in 2016 Unmanned Systems 4 (02), 155-165.

[**6.**]A Suarez, AE Jimenez-Cano, VM Vega, G Heredia, A Rodriguez-Castano, A Ollero. "Lightweight and human-size dual arm aerial manipulator," in 2017 International Conference on Unmanned Aircraft Systems (ICUAS), 1778-1784.

[**7.**]AE Jimenez-Cano, G Heredia, A Ollero. "Aerial manipulator with a compliant arm for bridge inspection," in 2017 International Conference on Unmanned Aircraft Systems (ICUAS), 1217-1222.

[**8.**]A Suarez, AE Jimenez-Cano, VM Vega, G Heredia, A Rodriguez-Castano, A. Ollero. "Design of a lightweight dual arm system for aerial manipulation," in 2018 Mechatronics 50, 30-44

[**9.**]G. Heredia, R. Cano, AE Jimenez-Cano and A. Ollero, "Modeling and Design of Multirotors with Multi-joint Arms", in "Aerial Robotic Manipulation", Eds. A. Ollero and B. Siciliano, Springer Tracts on Advanced Robotics, 2019.

[**10.**]AE Jimenez-Cano, G. Heredia, and A. Ollero, "Centralized Control of Multirotors with Manipulators", in "Aerial Robotic Manipulation", Eds. A. Ollero and B. Siciliano, Springer Tracts on Advanced Robotics, 2019.

[**11.**]AE. Jimenez-Cano, PJ. Sanchez-Cuevas, P. Grau, G. Heredia and A. Ollero, "Contact-based Bridge Inspection Multirotors: Design, Modelling and Control Considering the Ceiling Effect," in IEEE Robotics and Automation Letters, 2019.[Accepted]

1.4 Organization of this thesis

This thesis is organized in the following way (see Figure 1.4). Chapter 2 describes the methods used to derive the dynamics equations of aerial manipulator systems. By way example, using the Langrange-Euler Formalism, we obtain the dynamic model of a dual arm aerial manipulator and we use it to analyze the interaction between the manipulators and the aerial platform. As an essential part in the analytical study of aerial robots, we also introduce the most relevant aerodynamic forces and torque of this system. Finally, in chapter 2, we propose a model based control scheme for aerial manipulation systems.

Chapter 3 is dedicated a the aerial manipulation applications for assembly task developed during the thesis. First, we describes the QARM1 and AMUSE systems. The QARM1 prototype was an aerial manipulator consisting in a quadrotor equipped with a custom robot arm made using Rapid prototypes system. It was a pioneer UAM prototype inside ARCAS European proyect. In AMUSE prototype a Robai Cyton1500 7-DoF robot arm was mounted in an octorotor in coaxial configuration. This full equipped aerial manipulator was used in the outdoor final experiments of the ARCAS-project. The system analysis and description as well as these experiments results will be showed in this chapter. Furthermore, in chapter 3, we propose an adaption for a helicopter aerial manipulation of the control approach described in chapter 2, exploring the Kane's method to derive the dynamic model and showing experiments results to test and validate this approach.

Chapter 4 describes the developed aerial manipulators for structure inspection proposed in this thesis. The first case presented is a prototype of an octorotor in coaxial configuration equipped with a custom arm attached on the top of the mechanical structure to perform bridge inspections by contact. A full description of the system

is presented, analyzing the effects generated in the system due to the contact with the bridge surface. A control scheme is proposed and the results of experiments in a real bridge are shown. Furthermore, we present the design, development and implementation of an aerial compliant manipulator for structure inspection. In this case, we describe the lightweight compliance mechanism implemented and used in the compliant arm built, an aerial platform with a new configuration specially designed for aerial manipulation and a force-position controller to carry out inspection task. Some experiment in real scenarios are also presented. Finally, we present a FH system specially developed for measuring the bridge girder deflections. A nonlinear controller that benefits from the prototype design and the ceiling effect is proposed and tested in real scenarios.

The last chapter of this thesis has been dedicated to conclusions and future works.

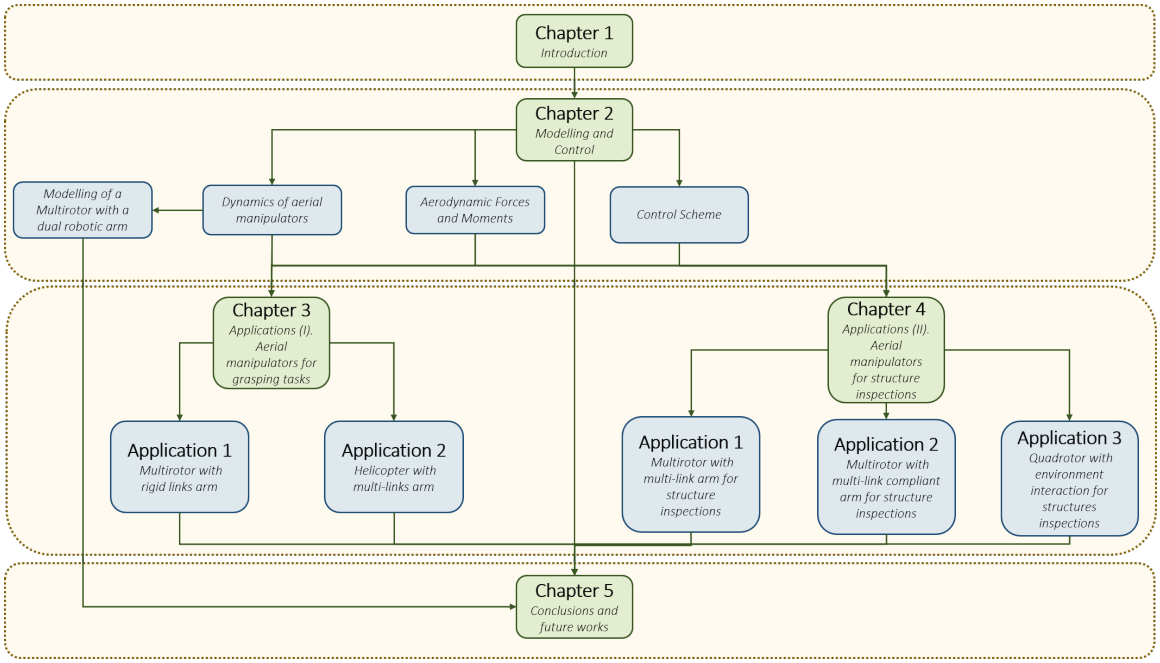

Figure 1.4: Graphical representation of the thesis organization.

Chapter 2

Modelling and Control

In this chapter, first, we briefly review the theoretical methods used to derive the dynamic model of an aerial manipulator. In the Introduction, following the criteria given in (Ruggiero et al., 2018), we have presented two different cases of aerial manipulators, *flying hand*(FH) and *unmanned aerial manipulator*(UAM). For mechanical systems, the typical approaches to derive the dynamic model are the Lagrange-Euler method and the Newton-Euler recursive formulation. Although, these two solutions are equivalent, the procedure to follow differs in both methods and the resulting equations have different properties in therms of efficiency, computational cost, etc. That is, while in the Lagrange-Euler formalism it is possible to obtain the whole dynamic model in symbolic matrix form, using the Newton-Euler recursive formulation, the resulting model is more computationally efficient. An example in the use of the Lagrange-Euler formalism for an aerial manipulator system can be seen in (Lippiello and Ruggiero, 2012). A case in which the Newton-Euler recursive formulation was used is (Kannan et al., 2013). There is, however, another approach that can be used to derive the dynamic model of an aerial manipulator, the Kane's method. This method presents the advantages of both the above approaches. These three solutions have been used in the analysis of the dynamics of the different aerial manipulators carried out during this thesis and, for this reason, these will be introduced briefly in the next section.

For modelling and control design in aerial manipulators it is important to consider the aerodynamic forces and torques of the UAV, since it will have to fly very close to

objects and the environment, and the airflow from the rotors may interfere with them. The derivation of the full aerodynamic model for a rotorcraft UAV is very complex and is out of the scope of this thesis. Nevertheless, the main aerodynamic forces and torques generated when the UAV is flying in the proximity to surfaces have been taken into account and are briefly analyzed in the section 2 of this chapter.

The last part of this chapter has been dedicated to control design. A non-linear control method to accomplish manipulation tasks while guaranteeing the system stability is presented in it. The proposed solution has been applied to the different aerial manipulator systems and validated with simulations and real experiments. The nonlinear control proposed is based on the Backstepping technique adding an integral term in some cases and considering the arm dynamics and the aerodynamic forces. We also introduce several manipulator control solutions.

The chapter is organized as follows: first, the methods to calculate the dynamic equations through both Lagrange and Newton-Euler will be presented. The application of the Kane's method to derive the dynamic equations is also introduced. Next, The aerodynamic moments and forces applied to these systems are also presented. Finally, the control scheme proposed will be developed for a generic aerial manipulator case.

2.1 Dynamics of aerial manipulators

This section presents the derivation of the dynamic equations of an aerial manipulator. There are several methods for obtaining the dynamics of a mechanical system. The sets of equations generated by these methods are equivalent, but some of them may be better suited for analysis and others for computation. In the aerial manipulation bibliography, the methods commonly used are Euler-Lagrange and Newton-Euler, but also Kane's method has been used in some cases.

The Lagrange-Euler equations of motion can be obtained in a structured form allowing a detailed analysis of the properties of the system but with a high computational cost. In fact, the main disadvantage of this method is the need for the differentiation of the energy functions such as the kinetic and potential energies, that may cause efficiency problem for large multibody systems. The Newton-Euler method provides

a very efficient set of recursive equations, but with a more difficult use for deriving advanced control laws. On the other hand, the Kane's method uses the generalised forces to eliminate the need for analysing interaction and constraint forces between bodies and does not employ energy functions (Kane et al., 1983) (Kane and Levinson, 1985). In other words, it could be said that it has the advantages of Newton-Euler and Lagrange-Euler without their disadvantages, although the generalised variables can be lees intuitive. Moreover, it is less used in general, probably due to it is less known, and its complex notation and learning. Both methods have been explored in this thesis.

An aerial vehicle equipped with multiple arms can be considered as a kinematic tree in which the base body(aerial platform) is a floating-base (Featherstone, 2014). It means a body in free motion relative to the fixed frame and not subjected to constraints.Thus, to model a floating-base, we need to introduce a new 6-DoF joint (three for position and three for orientation) connected between the fixed frame, S, and the multirotor frame located in it center of gravity,B. Each arm of the aerial manipulator will be the i-th branch of the kinematic tree with $i = 1, ..., k$ (see Figure 2.1)

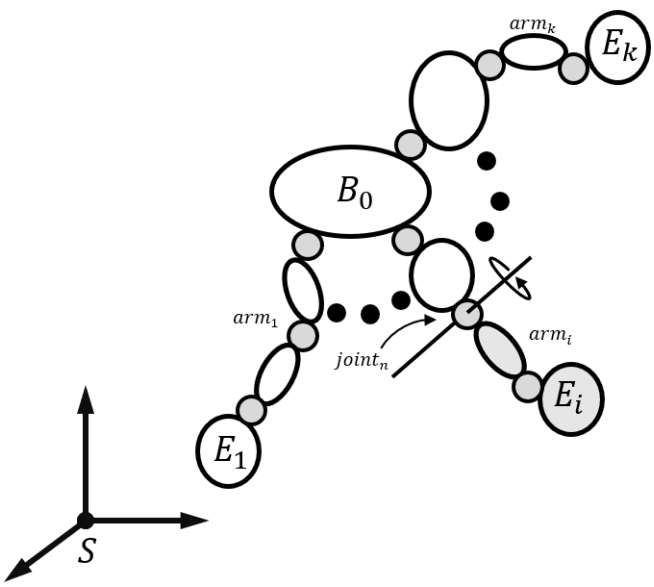

Figure 2.1: kinematic tree representing an aerial manipulator with multiple arms

The whole system will have k branches with r_k links. Moreover, we will define N_B and $N = 6 + \sum_{i=1}^{k} r_i$ as the number of bodies and degrees of freedom in the whole system and an end-effector frame E_i $(i = 1, ..., k)$ for each arm. Let us also consider that there are no loops and each joint of each arm can be prismatic or revolute. In the following, we introduce briefly the main steps of each method above mentioned to derive the dynamic model of an aerial manipulator with the above configuration.

2.1.1 Euler-Lagrange Formalism

First of all, to obtain the system equations of motion through Euler-Lagrange, we need to define a set of generalised coordinates, $\varphi = [\varphi_1 \, ... \, \varphi_N]^\top \in \mathbb{R}^N$. φ must fully describe the configuration of our aerial manipulation system. Thus, we have that φ is composed by three translation joints, $p = [x \; y \; z]^\top \in \mathbb{R}^3$, and three revolute joints, $\eta = [\phi \, \theta \, \psi]^\top \in \mathbb{R}^3$, which represent the six DOF of the aerial vehicle plus the joints of each manipulator arm, $\gamma^i = [\gamma_1^i \, ... \, \gamma_{r_i}^i]^\top \in \mathbb{R}^{r_i} (i = 1, ..., k)$. Thus, the system's generalised coordinates are given by

$$\varphi = [p \, \eta \, \gamma^1 \, ... \, \gamma^k] \in \mathbb{R}^N \; with \; N = 6 + \sum_{i=1}^{k} r_i \tag{2.1}$$

Moreover, to simplify the notation, we will use φ_n $(n = 1, ..., N)$ to refer to a specific coordinate of φ where the first six correspond to $[p\eta]^\top \in \mathbb{R}^6$ and the rest to the joints of the arms. The second step is to calculate the Lagrangian, $L(\varphi, \dot{\varphi})$, which is obtained as the difference between the kinetic and potential energies of the system. Thus,

$$L(\varphi, \dot{\varphi}) = K(\varphi, \dot{\varphi}) - P(\varphi) \tag{2.2}$$

where $K(\varphi, \dot{\varphi})$ and $P(\varphi)$ are the kinetic and potential energy both defined as a function of the generalised coordinates. Then, the system equations of motion are calculated by the Lagrange equations expressed by

$$\frac{d}{dt}\frac{\partial L(\varphi,\dot{\varphi})}{\partial \dot{\varphi}_i} - \frac{\partial L(\varphi,\dot{\varphi})}{\partial \dot{\varphi}_i} = \Gamma_i \qquad i = 1, ..., N \tag{2.3}$$

where Γ_i is the external force acting on the ith generalised coordinate. In a kinematic tree, the kinetic energy is calculated as the sum of the kinetic energies of its bodies and is given by

$$K = \frac{1}{2}\sum_{i=1}^{N_B}(v_i^b)^T \mathcal{M}_i (v_i^b) \tag{2.4}$$

where $\mathcal{M}_i$ is the generalised inertia matrix of the ith link defined as,

$$\mathcal{M}_i = \begin{bmatrix} m_i I_{3\times3} & 0 \\ 0 & \mathcal{I}_i \end{bmatrix} \tag{2.5}$$

where m_i and $\mathcal{I}_i \in \mathbb{R}^{3\times3}$ are the mass and the inertia tensor of the ith body and $I_{3\times3} \in \mathbb{R}^{3\times3}$ is an identity matrix. v_i^b is the velocity of the body i and is calculated as

$$v_i^b = \sum_{i\in\kappa(i)} J_i^b \dot{\varphi}_i \tag{2.6}$$

where $J^b \in \mathbb{R}^{6\times N}$ is the body Jacobian and $\kappa(i)$ is the set of points on the path between the body i and the base, that is the fixed frame S. Then the total kinetic energy can be obtained by the sum of the kinetic energy of each link,

$$K = \frac{1}{2}\dot{\varphi}^T(M(\varphi)))\dot{\varphi} \tag{2.7}$$

where $M(\varphi) \in \mathbb{R}^{N\times N}$ is the system inertia matrix and it is defined as,

$$M(\varphi) = \sum_{i=1}^{N}(J_i^b)^T M_i J_i^b \tag{2.8}$$

On the other hand, the total potential energy must be calculated to complete the derivation of the Lagrangian. For each link i, the potential energy can be obtained as,

$$P(\varphi) = m_i g h_i(\varphi) \tag{2.9}$$

Where $h_i(\varphi)$ is the height of the center of gravity of the ith link. Then, the total potential energy can be obtained as the sum of the potential energies of each link as,

$$P(\varphi) = \sum_{i=1}^{N} (m_i g h_i(\varphi)) \tag{2.10}$$

Using the kinetic and potential energies to complete the Lagrangian and substituting into Lagrange's equations 2.2, the dynamic model of the system can be expressed in matrix form as follows

$$M(\varphi)\ddot{\varphi} + C(\varphi, \dot{\varphi})\dot{\varphi} + G(\varphi) = \Gamma \tag{2.11}$$

where M is are the generalised inertia matrix, G represents the centrifugal and Coriolis terms, G is the gravity component. The terms of the Coriolis matrix can be derived through the system inertia matrix $M(\varphi)$ as follows

$$C_{ij}(\varphi, \dot{\varphi}) = \frac{1}{2} \sum_{k=1}^{N} (\frac{\partial M_{ij}}{\partial \varphi_k} + \frac{\partial M_{ik}}{\partial \varphi_j} - \frac{\partial M_{kj}}{\partial \varphi_i}) \dot{\varphi}_k \tag{2.12}$$

And the gravity vector $G(\varphi)$ is obtained directly from the potential energy as

$$G_i(\varphi) = -\frac{\partial P}{\partial \varphi_i} \qquad i = 1, ..., N \tag{2.13}$$

The forces and moments acting on the system are given by

$$\Gamma = \begin{bmatrix} F_a \\ \tau_a \\ \tau_{m_1} \\ \dots \\ \tau_{m_k} \end{bmatrix} + \tau_{ext} \tag{2.14}$$

Herein F_a and τ_a are the forces and torques generated by the rotors of the aerial vehicle respectively and they are related to the number of rotors and the configuration of the multirotor. The external forces and torque are represented by τ_{ext}.

2.1.2 Newton-Euler Formalism

In the Lagrangian Formalism, the system dynamics are derived using the Lagrangian function of the whole system, that means calculating the difference between the kinetic and potential energy. In contrast, the Newton-Euler Formalism is based on the balance of forces and moments acting on a body of the system. This allows obtaining the system dynamics following two recursive steps. First, the velocities and accelerations of each body are calculated through an outward recursion from the fixed frame to each system link. Then, the forces required to produce this acceleration are computed using the Newton-Euler equations. In each link of a kinematic tree, the velocity and acceleration are given by

$$\begin{aligned} v_i &= v_{i-1} + \Phi_i \dot{\varphi}_i \qquad (v_0 = 0) \\ a_i &= a_{i-1} + \Phi_i \ddot{\varphi}_i + \dot{\Phi}_i \dot{\varphi}_i \qquad (a_0 = -a_g) \end{aligned} \tag{2.15}$$

Initializing a_0 to $-a_g$, the gravity effect can be added. Then, we calculate the forces required to generate these accelerations as

$$f_i^a = \mathcal{I}_i a_i + v_i \times \mathcal{I}_i v_i - f_i^{ext} \tag{2.16}$$

The next step is the inward recursion, in which the force balance equation of each body is used to compute the spatial force across the joints from the forces/torques acting on the bodies. Then, iterating from N_B to 1 we have

$$\begin{aligned} f_i &= f_i^a - f_{ext} + \sum_{j \in c(i)} f_j \\ \tau_i &= \Phi_i^\top f_i \end{aligned} \tag{2.17}$$

More details of the equations and the recursive algorithm can be found on (Spong, 1989), (Siciliano and Khatib, 2016) and (Featherstone, 2014). Finally, the equations obtained can be rewritten in a closed form as in 2.11.

2.1.3 Kane's Method

The main idea in the Kane's method is to project the forces and torques on the directions of the generalized coordinates, transforming then into generalized forces and then obtaining the equilibrium equations of the generalized forces (Stoneking, 2013). For this reason it is also named generalized D'Alembert's principle. A general procedure of the Kane's method starts defining the locations of the center of mass of each system body and the locations of the applied forces. Then, we select the generalized coordinates φ and the generalized speeds v and the angular velocity ω (aerial vehicle) and $\dot{\gamma}$ in the arms' case. Next, we construct the partial velocities, v_r^i, and present the Kane's equation given by

$$F_r + F_r^* \qquad r = i, ..., N \tag{2.18}$$

Therefore, for a system with a set of N_B rigid bodies and N degrees of freedom, the generalized active forces are given by

$$F_r = \sum_{i \in \kappa(i)} [w_r^i \tau_i + v_r^i F_i] \tag{2.19}$$

and the generalized inertia forces are given by

$$F_r^* = \sum_{i \in \kappa(i)} [w_r^i(\mathcal{I}_i \dot{\omega}_i - \omega_i \times H) + v_r^i(-m_i a_i)] \tag{2.20}$$

The equation 2.18 is in vector form but it can be rewritten in a closed form as the equation 2.11. This method is used in the second application of chapter 3 to derive the dynamics of a helicopter equipped with a robotic arm.

2.2 Modelling of a Multirotor with a dual robotic arm

In the above section, we introduce the typical methods used to derive the dynamic model of a mechanical system. As an example, let us obtain the dynamic equations of a dual-arm aerial manipulator through the Lagrange-Euler formalism. The followed methodology was published in (Suarez et al., 2018b), one the publications that contribute to this thesis.

The motivation to mount a dual arm system in an aerial platform is to extend the grasping an manipulation capabilities with respect to a single arm case. This configuration allows the simultaneous grasping and transportation of two objects, or large objects that cannot be handled with a single arm, or to accomplish manual operations in which a camera can be positioned in one arm end-effector, assisting with visual feedback in the operation.

In other to simplify the resulting symbolic equations of the system, we have followed an approach based on barycentric vectors. This approach was first time proposed for space manipulator in (Papadopoulos, 1990) and applied to multiple manipulators in (Papadopoulos and Moosavian, 1994). Its main difference with other approaches is the calculus of system kinematics using a minimum set of body-fixed barycentric vectors and allowing to derive the dynamics w.r.t the center of mass of the full system.

Kinematic model

In the derivation of the kinematic and dynamic equations of a multirotor equipped with multiple robotic arms, it results convenient to express the position of the masses in terms of a set of body-fixed barycentric vectors. With this, the equations of motion can be written in terms of the translation of the system center of mass with respect to an inertial reference frame.

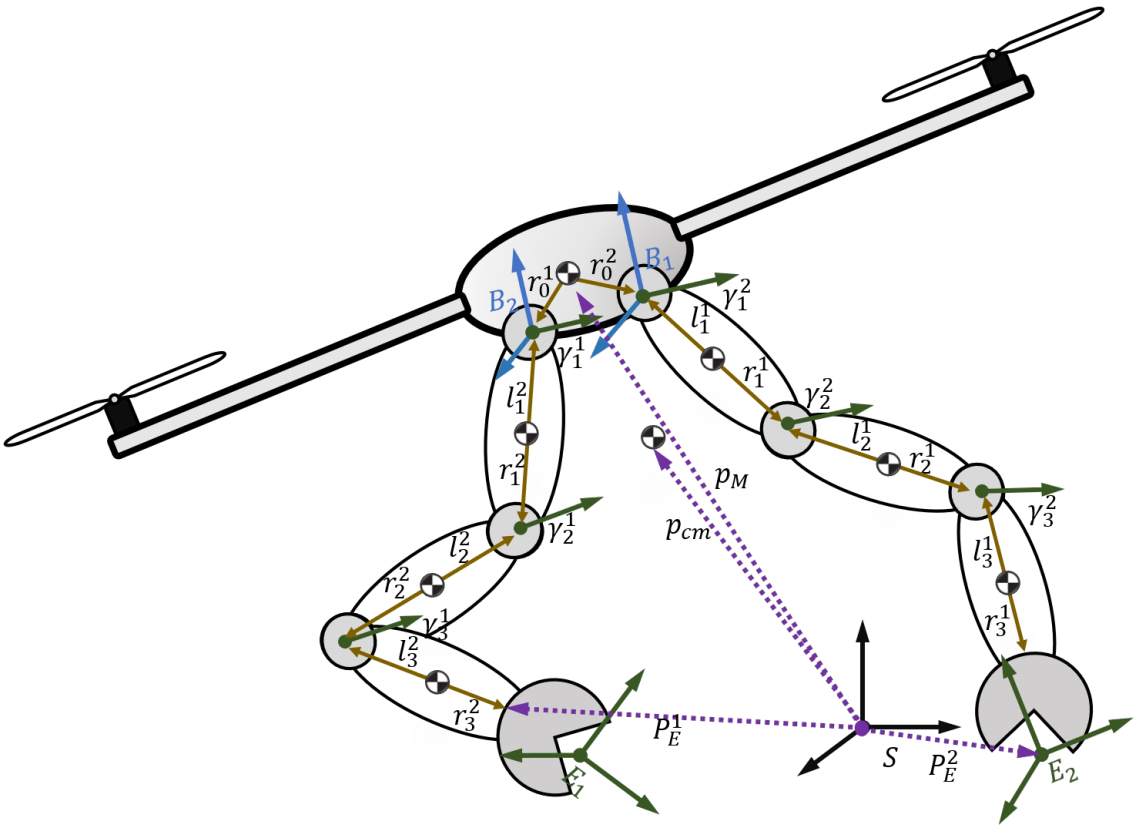

Figure 2.2: Scheme of multi-rotor equipped with two 3-DOF arms.

Let consider the schematic representation of the multi-rotor platform equipped with two manipulators depicted in Figure 2.2. The position of the center of mass and the attitude of the multi-rotor with respect to the inertial reference frame, S, are denoted by r_M and by the roll, pitch and yaw angles (ϕ, θ and ψ, respectively), while p_{cm} is the position of the center of mass of the whole system. Each of the M = 2 arms

consists of N = 3 links for end effector positioning, being γ_k^i the k-th joint position of the i-th arm, and l_k^i and r_k^i the length and position of the center of mass of the respective link. The two additional DOF's provided by each arm for wrist orientation are not considered for simplicity and because they do not have a significant influence over multirotor dynamics. Taking into account the 6 DOF's for the position and attitude of the aerial platform, the total number of degrees of freedom of the system is D = 12 .

Now it is necessary to relate the position of the center of mass of every single link with the position of the global center of mass. Let call $P_{k,a}^i \in \mathbb{R}^3$ to the position of an arbitrary point a on the link k of the manipulator i given by:

$$P_{k,a}^i = p_{cm} + \rho_k^i + r_{k,a}^i \tag{2.21}$$

where $r_{k,a}^i \in \mathbb{R}^3$ is the position vector from the k-th link center of mass of manipulator i to point a, and $\rho_k^i \in \mathbb{R}^3$ is computed in the following way:

$$\rho_k^i = T_\eta \sum_{p=1}^{M} \sum_{j=1}^{N} R_{0,j}^p v_{j\delta_{ip}}^p \tag{2.22}$$

Here δ_{ip} is the Kronecker delta, $T_\eta \in \mathbb{R}^{3\times3}$ is the rotation matrix of the multirotor with respect to the inertial frame, and $R_{0,j}^p \in \mathbb{R}^{3\times3}$ is the rotation matrix between the j-th link frame of manipulator p and the frame of the aerial platform. Taken into account 2.21, 2.22 can be rewritten as:

$$\begin{aligned} P_{k,a}^i &= p_{cm} + \rho_k^i + r_{k,a}^i = p_{cm} + T_\eta \sum_{p=1}^{M} \sum_{j=0}^{N} R_{0,j}^p v_{jk,a}^p \\ v_{jk,a}^i &= v_{jk}^i + \delta_{ja}^i \cdot r_{k,a}^i \end{aligned} \tag{2.23}$$

where $v_{jk}^i \in \mathbb{R}^3$ is the barycentric vector defined as the position vector of the k-th link center of mass of manipulator i-th with respect to the system center of mass:

$$v^i_{jk} = \begin{cases} r^{i*}_j = -l^i_j \mu^i_j + r^i_j \mu^i_{j+1} & j < k \\ c^{i*}_j = -l^i_j \mu^i_j - r^i_j (1 - \mu^i_{j+1}) & j = k \\ l^{i*}_j = l^i_j (1 - \mu^i_j) - r^i_j (1 - \mu^i_{j+1}) & j > k \end{cases} \tag{2.24}$$

where $l^i_j \in \mathbb{R}^3$ and $r^i_j \in \mathbb{R}^3$ are defined in Figure 2.2 and the mass distribution, μ^i_j, is given by:

$$\mu^i_j = \begin{cases} 0 & j = k \\ \frac{m_0}{m_T} + \sum_{p=1}^{M} \sum_{k=1}^{N(i,j,p)} \frac{m^p_k}{m_T} & j = 1, ..., N \\ 1 & j = N + 1 \end{cases} \tag{2.25}$$
$$N(i, j, p) = N - \delta_{ip}(N - j + 1)$$

Note from equation 2.25 that the position of the center of mass of each link respect to the inertial frame depends on the position of all links. The system center of mass is then computed as follows:

$$\begin{aligned} p_{cm} &= \frac{1}{m_T}(p_M m_0 + \sum_{p=1}^{M} \sum_{j=1}^{N} d^i_j m^i_j) \\ d^i_j &= p_M + T_\eta \sum_{p=1}^{j} (R^i_{0,p-1} \cdot r^i_{p-1} - T^i_{0,p} l^i_p) \end{aligned} \tag{2.26}$$

The position of the end effector for each manipulator is obtained from equation 2.23:

$$P^i_E = p_{cm} + T_\eta \sum_{p=1}^{M} \sum_{j=1}^{N} R^p_{0,j} v^p_{jN,E} \tag{2.27}$$

where r_M represents the multirotor center of mass position with respect to the inertial frame and $R^i_{0,0}$ is the identity matrix. Using the equations 2.24 and 2.25 it results that:

$$P_E^i = \begin{bmatrix} r_{Mx}^i \\ r_{My}^i \\ r_{Mz}^i \end{bmatrix} + T_\eta \begin{bmatrix} r_{0x}^i + rl_1^i c_{\gamma_1^i}(rl_2^i s_{\gamma_2^i} + rl_3^i s_{\gamma_{2,3}^i}) \\ r_{0y}^i + rl_1^i s_{\gamma_1^i}(rl_2^i s_{\gamma_2^i} + rl_3^i s_{\gamma_{2,3}^i}) \\ r_{0z}^i + rl_1^i - rl_2^i c_{\gamma_2^i} + -l_3^i c_{\gamma_{2,3}^i} \end{bmatrix} \tag{2.28}$$

with $rl_j^i = (r_j^i - l_j^i)$, $c_{\gamma_j^i} = cos(\gamma_j^i)$, $s_{\gamma_j^i} = sin(\gamma_j^i)$, $c_{\gamma_{j,k}^i} = cos(\gamma_j^i + \gamma_k^i)$ and $s_{\gamma_{j,k}^i} = sin(\gamma_j^i + \gamma_k^i)$. The equations 2.22 and 2.23 can be differentiated with respect to the time to obtain the position velocity of an arbitrary point a in the body k of the i-th manipulator:

$$\begin{aligned} \dot{P}_{k,a}^i &= \dot{p}_{cm} + \dot{\rho}_k^i + \dot{r}_{k,a}^i \in \mathbb{R}^3 \\ \dot{\rho}_k^i &= \sum_{p=1}^{M} \sum_{j=0}^{N} \omega_j^p \times v_{j(k\delta_{ip})}^p \in \mathbb{R}^3 \\ \omega_k^i &= \omega_0 + T_\eta T_k^i \dot{q}^i \in \mathbb{R}^3 \\ T_k^i &= [R_{0,1}^i u_1^i, R_{0,2}^i u_2^i, ..., R_{0,k}^i u_k^i, 0, ..., 0] \in \mathbb{R}^{3\times 3} \end{aligned} \tag{2.29}$$

with $\omega_0^p = \omega_0 (p = 1, ..., M)$ denoting the multirotor angular velocity with respect to the inertial frame and vector $\dot{\gamma}^i = [\dot{\gamma}_1^i \, \dot{\gamma}_2^i \, \dot{\gamma}_3^i]^\top \in \mathbb{R}^N$ represents the joint rates of the i-th manipulator. The terms $u_j^i \in \mathbb{R}^3 \, (i = 1, ..., M \; j = 1, ..., k)$ are unit column vectors and represent the rotation axis of j-th joint of the i-th manipulator.

While the procedure introduced here to obtain the kinematic model has benefits when the dynamics equations are presented, the kinematics can be also derived through other methods as the use of the Product of Exponential or Denavit-Hartenberg. An introduction to these methods can be found in Appendix A.1.

Dynamic model

The dynamic model of the dual arm aerial manipulator system is derived from the Lagrange-Euler method described above. In this case, The vector of generalized coordinates is defined as:

$$\varphi = [p_{cm} \, \eta \, \gamma_1 \, \gamma_2]^\top \in \mathbb{R}^{12} \tag{2.30}$$

This vector includes the position of the center of mass of the multirotor, p_{cm}, and its attitude, along with the joint positions of both manipulators. The system can be considered as a kinematic tree where the multirotor is connected to a fixed base via a 6-DOF joint and each robot manipulator is a subtree connected to the multirotor, being the kinetic energy of the tree equal to the sum of the kinetic energies of its bodies. The benefit of using the barycentric vectors (equation 2.24) is that the manipulators can be replaced by virtual manipulators whose base is the system center of mass. Therefore, the kinetic energy of the system is given by:

$$K(\varphi) = \frac{1}{2} m_T \dot{p}_{cm}^\top \dot{p}_{cm} + \frac{1}{2} \sum_{i=1}^{2} \sum_{k=1}^{3} (\omega_k^{i\top} \mathcal{I}_k^i \omega_k^i + m_k^i \dot{\rho}_k^{i\top} \dot{\rho}_k^i) \tag{2.31}$$

In this equation, the first term corresponds to the kinetic energy associated to the translational speed of the system, while the two terms within the nested summation are the kinetic energy due to the translation and rotation of the link masses, being ω_k^i the rotational speed of the k-th joint in the i-th manipulator. The potential energy due to gravity can be calculated with respect to the system center of mass as:

$$V(\varphi) = g m_T z_{cm} \tag{2.32}$$

where g is the acceleration due to gravity and z_{cm} is the altitude of the center of mass (see equation 2.26). The equation of motion of the system can be expressed in the following general form:

$$M(r)\ddot{\varphi} + C(r, \dot{r})\dot{\varphi} + G(\varphi) = \Gamma \tag{2.33}$$

where the vector $r = [\eta\, \gamma^1\, \gamma^2]^\top$ represents the multirotor rotation and the manipulators' joint angles. The resulting inertia matrix for the developed dual arm aerial manipulation system has the following form:

$$M(r) = \begin{bmatrix} I_{3\times3}m_t & 0_{1\times3} & 0_{1\times3} & 0_{1\times3} \\ 0_{3\times1} & M_\eta(r) & M_{\eta\gamma^1}(r) & M_{\eta\gamma^2}(r) \\ 0_{3\times1} & M^\top_{\eta\gamma^1}(r) & M_{\gamma^1}(r) & M_{\gamma^1\gamma^2}(r) \\ 0_{3\times1} & M^\top_{\eta\gamma^2}(r) & M^\top_{\gamma^1\gamma^2}(r) & M_{\gamma^2}(r) \end{bmatrix} \tag{2.34}$$

It is interesting to note in the form of this matrix the decoupling between the translation and rotation of the aerial manipulation system.

Analysis of interactions between the manipulators and the aerial platform

The terms $M_{\eta\gamma^1}$ and $M_{\eta\gamma^2}$ in equation 2.34 are the submatrices of inertia, which represent the dynamic coupling between the multirotor and the arms. The structure of the inertia matrix is derived from the application of the method of barycentric vectors in the calculation of the kinematic and dynamic equations, referenced to the center of mass of the whole aerial manipulator. This fact is evidenced by the null term in the cross-submatrices where the acceleration of the center of mass (linear and twist) are related. The main benefit of this method is that the equations obtained result in a more compact and simple form for its implementation in a simulation framework, and for the design of a model-based controller. The drawback is that the observation of the dynamic effects associated with the interactions between the arms and the aerial platform requires the transformation to the kinematic domain.

A MATLAB/Simulink simulator was developed for identifying the reaction torques introduced in the base of the aerial platform due to the motion of the arms, obtaining the dynamic/kinematic equations using the MUPAD toolbox of MATLAB. Figure 2.3 shows the inertia, Coriolis and gravity components of the torque in the three axes when the left arm rotates from 0 to 90° in one second time. This estimation is obtained from the application of the dynamic model over the data provided by the servo actuators in the physical manipulator.

This example demonstrates that the gravity term is dominant in the pitch angle, whereas the inertia and Coriolis terms in the roll and yaw angles are associated to the unbalanced motion of the masses, as there is no compensation with the right arm. What is more, the offset component in the gravity term represents the displacement

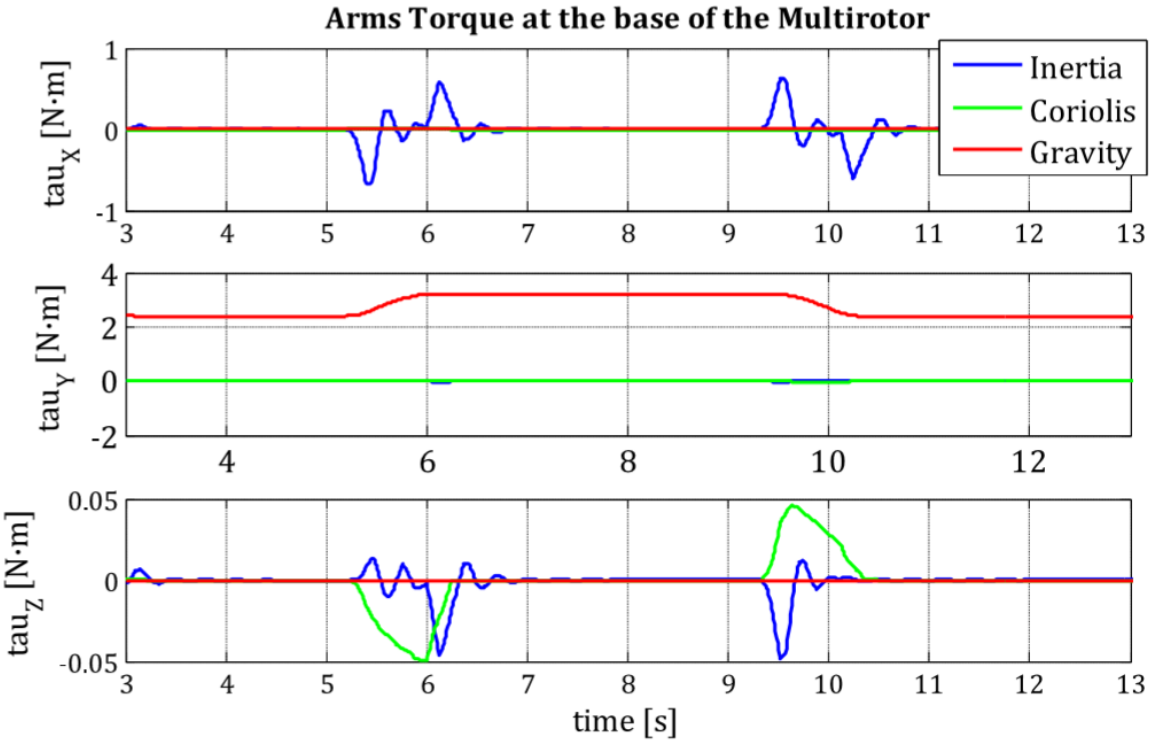

Figure 2.3: Inertia (blue), Coriolis and centrifugal (green) and gravity (red) terms in the XY axes for the 90° step in the shoulder pitch joint of the left arm. The components in the X and Z axes are caused by the asymmetry in the motion of the arms.

of the center of mass when the arms are attached to the aerial platform, and it should be compensated by the integral term in the autopilot during the flight operation.

The dynamic model above described shows a strong coupling between the manipulator and the multirotor, in such a way that the acceleration of any link in one arm will affect, not only to the aerial platform, but also to the joint torque in the other arm. Nevertheless, the torque induced in the joints by the acceleration of the aerial platform will be in practice dissipated by the relatively high friction of the gearbox of the servos, and by the embedded position controller. In other words, the motion of the arms will affect the stability of the aerial platform, but the opposite effect is not significant.

2.3 Aerodynamic Forces and Moments

In this work, all aerial vehicles considered have been Vertical Take-off and Landing (VTOL) platforms, such as multirotors, i.e., quadrotors, hexarotors or octorotors and helicopters. In vehicles having rotors as propulsion system, the aerodynamic forces and moments are calculated using momentum and blade element theory. The main aerodynamic forces and torques that we have taken into account in this thesis are the following:

2.3.1 Thrust Force

The thrust force is the sum of all the vertical forces acting on all the blade elements. The thrust force of each rotor can be calculated as

$$T_i = C_T \Omega_i^2 \tag{2.35}$$

where Ω_i is the angular speed of the i-th rotor and C_T is a constant which value depends on the geometry of the propeller (diameter, pitch, airfoil distribution) and the ambient conditions such as the air density or the relative humidity.

2.3.2 Drag Torque

The drag moment determines the power required to spin the rotor. This moment is caused by the aerodynamic forces acting on the blade elements. The horizontal forces acting on the rotor multiplied by the moment and integrated over the rotor.

$$Q_i = C_Q \Omega_i^2 \tag{2.36}$$

where C_Q is the drag coefficient which value depends on the geometry of the propeller (diameter, pitch, airfoil distribution) and the ambient conditions such as the air density or the relative humidity.

2.3.3 Ground effect

The ground effect in multirotors happens when the rotors are close to the ground and consists of a thrust increment due to the interaction of the rotor airflow with the ground surface. In (Sanchez-Cuevas et al., 2017a), this effect was studied and characterized in multirotors' case and the expression of the thrust increment due to the ground effect was calculated as:

$$\frac{T_{IGE}}{T_{OGE}} = \frac{1}{1 - (\frac{R}{4z})^2 - R^2(\frac{z}{\sqrt{(d^2+4z^2)^3}}) - (\frac{R^2}{2})(\frac{z}{\sqrt{(2d^2+4z^2)^3}}) - 2R^2(\frac{z}{\sqrt{(b^2+4z^2)^3}})K_b} \tag{2.37}$$

where T_{OGE} is the thrust generated by the rotor flying out of the ground effect and T_{IGE} is the thrust when the rotor is under the ground effect, R is the radius of the rotor, z is the vertical distance of the rotor to the ground, b is the distance between two opposite rotor axes and K_b is the empirical body lift coefficient. The ground effect can be included in the thrust model equation 2.35 resulting:

$$T_i = C_T \Omega_i^2 f_{GE}(z_{r_i}) \tag{2.38}$$

Herein $f_{GE}(z_{r_i})$ is the ground effect factor that accounts for the increment in thrust due to the ground effect and depends on the relative distance of each rotor to the ground, z_{r_i}.

Figure 2.4 compares the experimental and theoretical results of the increment in the thrust of a quadrotor as a function of the distance to the ground plane. We can see the results compared with a single rotor and with the PFI (Potential Flow with the method of images, (Cheeseman and Bennett, 1957)) approximations. The PFI is an analytical model that is used to model the ground effect in helicopters using potential flow with a single source to model the rotor airflow and the method of images to model the ground.

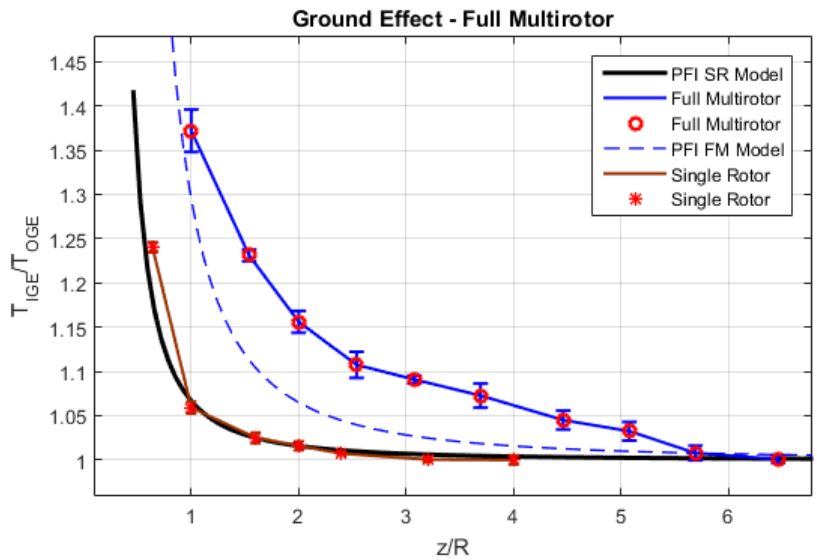

Figure 2.4: Experimental and theoretical results of the thrust behaviour due to ground effect for full multirotor demonstrated in (Sanchez-Cuevas et al., 2017b)

.

2.3.4 Ceiling effect

The ceiling effect appears when the aerial platform is flying close enough to a horizontal surface from below. The main difference between the ceiling and the ground effects is that while in the ground effect the increment in the rotor thrust takes the aerial vehicle away from the surface, in the ceiling effect this increment in the rotor thrust moves the UAV against the surface and thus can be dangerous and cause a crash with the ceiling. In (Jimenez-Cano et al., 2019), the ceiling effect was modelled through an aerodynamic analysis using CFD and was compared with experimental tests.

Figure 2.5 shows the results of $K_c(z_{c_i})$ that appear when the rotors approach the ceiling assuming that the power is constant. Using these results, the ceiling effect can be mathematically modelled and included in the thrust model equation. Then, it can be rewritten as:

$$T_i = K_c(z_{c_i}) C_T \Omega_i^2 \tag{2.39}$$

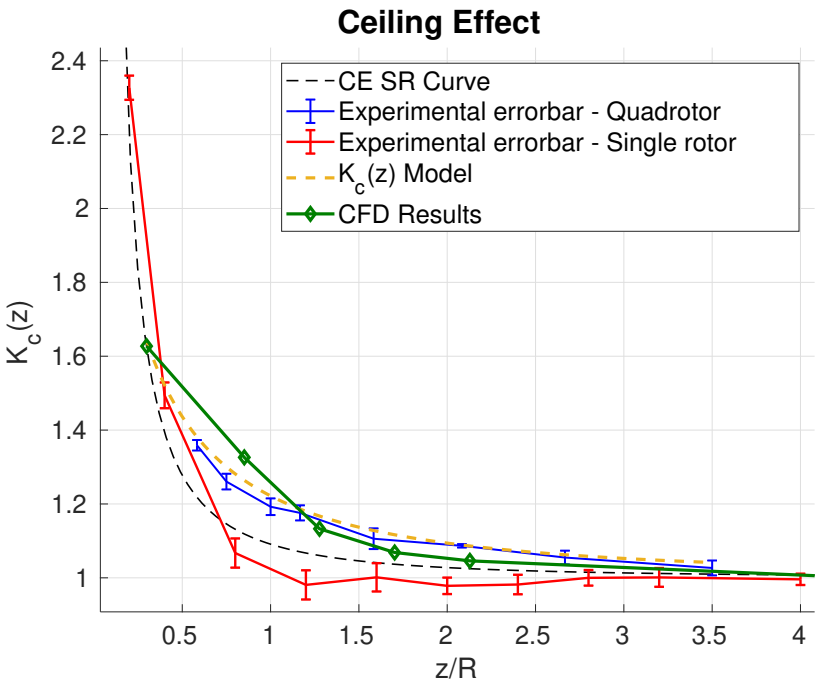

Figure 2.5: CFD Experimental Results Comparison. Blue error bar and red error bar are experimental results for quadrotor and multirotor respectively. Black braked line is the model proposed in (Sanchez-Cuevas et al., 2017b) for the single rotor in ceiling effect.

with

$$K_c(z_{c_i}) = \frac{1}{1 - \frac{1}{a_1}(\frac{R}{a_2 + z_{c_i}})^2} \tag{2.40}$$

where Both, $a_1 = 0.081$ and $a_2 = 1.026$ are values obtained through least squares minimizing the error with the CFD results.

2.4 Control Scheme

As above mentioned, in the control problem of an aerial manipulator there are two approaches: decentralized and centralized. In this thesis, we follow a centralized approach. Even though we design a controller for the multirotor and other for the manipulator, they share the full state of the system and are designed from the dynamic model of the full system (see Figure 2.6). The multirotor controller is responsible for

stabilizing attitude and global position of the aerial vehicle, taking into account and compensating the movements of the arm and the contact forces with the environment. The manipulator controller takes care of controlling arm joints angles and velocities, and the generalized forces τ that are generated by the aerial manipulator in the operational space, considering the movement and dynamics of the multirotor.

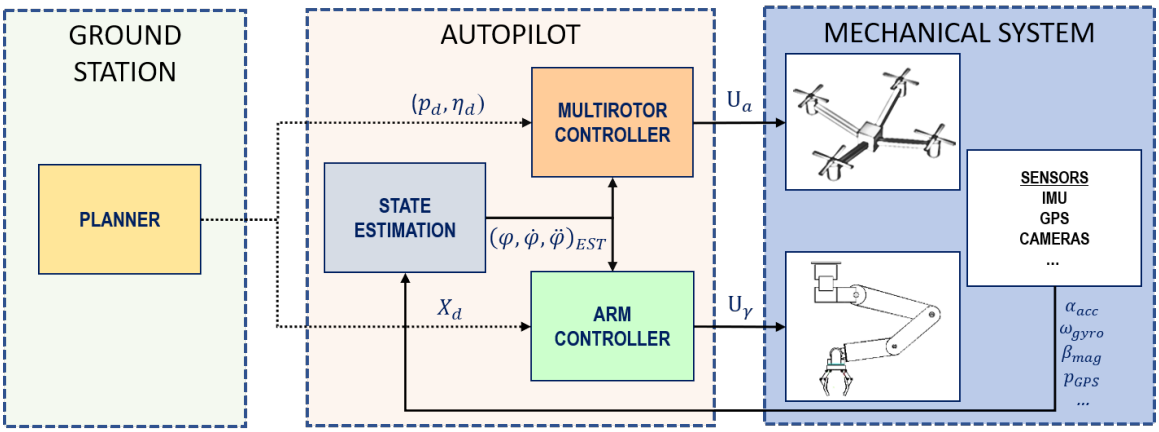

Figure 2.6: Control Scheme for an aerial manipulator

2.4.1 Multirotor Controller

A problem that arises in the aerial manipulators is that the dynamic behavior of the vehicle changes due to the modification of the aerial mass distribution and dynamics by grasping and manipulating objects. The main effects that appear and make the dynamic behavior of the multirotor with a manipulator different from the standard multirotor configuration that is usually considered are the following:

1. Displacement of the center mass from the vertical axis at the geometrical center.

2. Variation of mass distribution: the moments of inertia change significantly when the arm moves.

3. The dynamic reaction forces and torques generated by the movement of the arm.

These three effects are not usually taken into account explicitly, and are left to the integral term in the feedback controller for correction. The effects of the displacement of the mass center have been analyzed by some researchers. For example, (Pounds et al., 2012) presents stability limits within which the changing mass parameters of the system will not destabilize quadrotors and helicopters with standard PID controllers. On the other hand, (Mellinger et al., 2011) studies the effect of grasping objects at a point displaced from its center of mass and develops a controller that takes it into account explicitly. In (Kemper and Fatikow, 2006), the center of mass is also considered, but the variations of the moments of inertia are discarded. The influence of the center of mass being above or below the equatorial multirotor plane is analyzed in (Bristeau et al., 2009). Adaptive controllers that compensate for the unknown displacement of the center of mass have also been presented (Palunko and Fierro, 2011) and (Antonelli et al., 2013). Taking into account the above mentioned three effects a nonlinear based-model controller is proposed. This control approach is generalized solution adapted from the Variable Parameter Integral Backstepping (VPIB) controller that was presented in (Jimenez-Cano et al., 2013). Variable Parameter Integral Backstepping (VPIB) has shown as an effective control technique for aerial manipulation vehicles (Heredia et al., 2014) and it is based on a nonlinear Backstepping controller whose parameters vary accordingly with the dynamics of the manipulator and provides a good dynamic response when the manipulator moves. Deriving the dynamic model of the system from one the methods above mentioned, we can write these model equations in a compact form as follows:

$$M(\varphi)\ddot{\varphi} + C(\varphi, \dot{\varphi})\dot{\varphi} + G(\varphi) = \tau + \tau_{ext} \tag{2.41}$$

where $\varphi = (p, \eta, \gamma)^T \in \mathbb{R}^N$ is the vector of generalized coordinates. Then, analyzing the equation 2.41 and without loss of generality (Park and Khatib, 2005), it can be rewritten as

$$\begin{bmatrix} M_a & M_{am} \\ M_{am}^T & M_m \end{bmatrix} \begin{bmatrix} \ddot{p} \\ \ddot{\eta} \\ \ddot{\gamma} \end{bmatrix} + \begin{bmatrix} C_a \\ C_m \end{bmatrix} + \begin{bmatrix} G_a \\ G_m \end{bmatrix} = \begin{bmatrix} F_a \\ \tau_a \\ \tau_\gamma \end{bmatrix} + \tau_{ext} \tag{2.42}$$

where $M_a \in \mathbb{R}^{6\times 6}$, $M_m \in \mathbb{R}^{(N-6)\times(N-6)}$ and $M_{am} \in \mathbb{R}^{(6)\times(N-6)}$ are aircraft, manipulator and coupling inertia matrices. $C_a = [C_p, C_\eta]^T \in \mathbb{R}^6$ and $C_m \in \mathbb{R}^{N-6}$ are the aerial vehicle and manipulator Coriolis and centrifugal forces, and $G_a = [G_p, G_\eta]^T \in \mathbb{R}^6$ and $G_m \in \mathbb{R}^{N-6}$ are the aerial vehicle and manipulator gravity forces vector. Therefore, the multirotor equations of motion can be decoupled from the upper part of the equation 2.42 as follows

$$\begin{bmatrix} M_p & 0 \\ 0 & M_\eta \end{bmatrix} \begin{bmatrix} \ddot{p} \\ \ddot{\eta} \end{bmatrix} + C_a + G_a = \begin{bmatrix} F_a \\ \tau_a \end{bmatrix} + \tau_{ext}^a - M_{am}\ddot{\gamma} - \begin{bmatrix} 0 & M_{p\eta} \\ M_{p\eta}^T & 0 \end{bmatrix} \begin{bmatrix} \ddot{p} \\ \ddot{\eta} \end{bmatrix} \tag{2.43}$$

Most prototypes developed in this thesis had been made with multirotors in the most popular configurations, i.e. quadrotors, hexarotors, octorotors, etc. These are underactuated systems which have four control inputs, $U = [U_z, U_\phi, U_\theta, U_\psi]$, for six degrees of freedom. The four control inputs correspond to the total thrust, T, generated by the rotors and the three torques generated by these rotors in the three multirotor attitude angles, $(\tau_\phi, \tau_\theta, \tau_\psi)$. These control inputs are directly related to the generalized forces and torques of the equation 2.42 as follow

$$\begin{bmatrix} F_a \\ \tau_a \end{bmatrix} = \begin{bmatrix} U_p \\ U_\eta \end{bmatrix} = \begin{bmatrix} R_\eta \begin{bmatrix} 0 \\ 0 \\ T \end{bmatrix} \\ \tau_\phi \\ \tau_\theta \\ \tau_\psi \end{bmatrix} = \begin{bmatrix} U_x \\ U_y \\ U_z \\ U_\phi \\ U_\theta \\ U_\psi \end{bmatrix} \tag{2.44}$$

where U_x and U_y are virtual control inputs that are used to command desired angles (ϕ_d and θ_d) when the multirotor tracks a horizontal path. The control proposed for the multirotor follows the classic cascade control where desired roll and pitch angles are calculated by the desired horizontal position. Thus, we have a position controller in an upper loop which outputs are the desired thrust, U_z, and the desired attitude,

and the attitude controller into an inner loop which outputs are the attitude torques, U_η (see Figure 2.7).

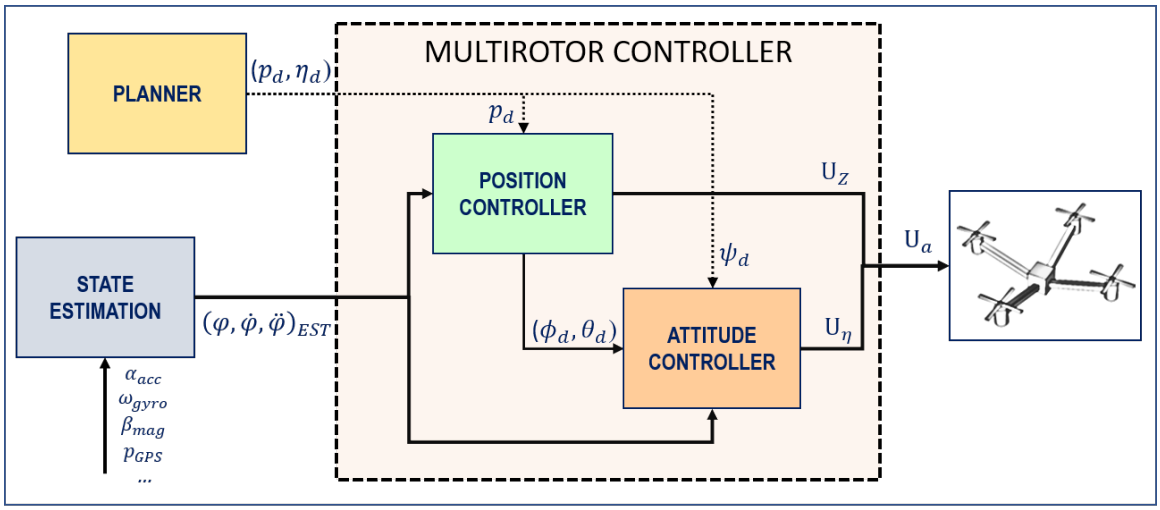

Figure 2.7: Control Scheme for multirotor controller

Attitude Controller

Consider the tracking error $e_\eta = \eta_d - \eta$, where η_d is the desired attitude and its dynamics:

$$\frac{de_\eta}{dt} = \dot{\eta}_d - \omega \tag{2.45}$$

Then a virtual control over the angular speed ω can be formulated, which is not a control input. Therefore, the desired angular speed can be defined as follows:

$$\omega_d = k_\eta e_\eta + \dot{\eta}_d + \lambda_\eta \chi_\eta \tag{2.46}$$

with k_η and λ_η are positive diagonal gain matrix and χ_η are the integral of each tracking attitude angle error. Next, the angular velocity tracking error $e_{\dot{\eta}}$ and its dynamics can be defined by:

$$e_{\dot{\eta}} = \omega_d - \omega \tag{2.47}$$

$$\frac{de_{\dot{\eta}}}{dt} = k_\eta(\dot{\eta}_d - \omega) + \ddot{\eta}_d + \lambda_\eta e_\eta - \ddot{\eta} \tag{2.48}$$

Using 2.46, 2.46 and 2.48 the attitude tracking error dynamics equation 2.45 can be rewritten as:

$$\frac{de_\eta}{dt} = -k_\eta e_\eta - \lambda_\eta e_\eta + e_{\dot{\eta}} \tag{2.49}$$

Now, $\ddot{\eta}$ in 2.47 and 2.48 can be replaced by its expression in the dynamic model 2.43, and the control input U_η appears explicitly. Then, combining the tracking errors of position e_η and the angular speed $e_{\dot{\eta}}$, and the integral position tracking error χ_η using the above equations the control input U_η can be calculated as:

$$U_\eta = D^{\triangle}(M_\eta)[(1-k_\eta^2+\lambda_\eta)e_\eta+(k_\eta+k_{\dot{\eta}})e_{\dot{\eta}}-k_\eta\lambda_\eta\chi_\eta]-F(M_\eta)-C_\eta-G_\eta-M_{am}\ddot{\gamma}+\tau_{ext}^{\eta,\gamma} \tag{2.50}$$

where $k_{\dot{\eta}}$ is a diagonal positive gain matrix which determines the convergence speed of the angular speed loop. The term $D^{\triangle}(M_\eta)$ represents the diagonal of M_η and depends on both the attitude angles and the arm joint angle positions. $F(M_\eta)$ represents the sum of the coupled terms such as $M_{p\eta}^T\ddot{p} \in \mathbb{R}^3$ or the coupled non-diagonal terms derived from the inertia matrix M_η. C_η and G_η are the nonlinear terms described above. In practice, the attitude controller terms can be rearranged in the following way:

$$U_\eta = D^{\triangle}(M_\eta)[K_P e_\eta + K_I\chi_\eta + K_D e_{\dot{\eta}}] - F(M_\eta) - C_\eta - G_\eta - M_{am}\ddot{\gamma} + \tau_{ext}^{\eta,\gamma} \tag{2.51}$$

where K_P, K_I and K_D are the parameters of a standard PID controller. The first part of the controller can be seen as a gain-scheduled PID with the different positions of the arm, while the nonlinear terms compensate the full coupled dynamic effects. In this way, it is easier to tune the controller parameters starting from the standard PIDs that are used by many multirotors as base controllers. The proof of stability for this control approach can be seen in the appendix section.

Position Controller

The expression of the position controller can be derived in a similar way to the steps followed above,

$$U_p = M_p(D^{\triangle}(R_\eta e_3))^{-1}[K_P e_p + K_I \chi_p + K_D e_{\dot{p}}] - C_p - G_p + F_{ext}^{p,\gamma} \tag{2.52}$$

Herein M_p is a diagonal matrix which terms are the total weight of the system and $D^{\triangle}(R_\eta e_3)$ is a diagonal matrix formed with the vector $R_\eta e_3 \in \mathbb{R}^3$ where $R_\eta \in SO(3)$ is the rotation matrix of the aerial platform and $e_3 = (0, 0, 1)^T$. $F_{ext}^{p,\gamma}$ represents the external forces applied over the end-effector and transformed to the translation axis of the center of mass of the multirotor. In practice, C_p should be a zero vector and $G_p = (0, 0, g)^T$. Therefore, equation 2.52 is given by,

$$U_p = M_T(D^{\triangle}(R_\eta e_3))^{-1}[K_P e_p + K_I \chi_p + K_D e_{\dot{p}}] - G_p + F_{ext}^{p,\gamma} \tag{2.53}$$

where M_T represents the total weight of the system. As mentioned above, the horizontal position controller, (U_x, U_y), outputs the attitude references ϕ_d and θ_d in response to a deviation from the y_d or x_d references respectively, which are tracked by the attitude controller. Then, this control law is adapted to generate the attitude references ϕ_d and θ_d using the elementary rotation around z,

$$R_z = \begin{bmatrix} \cos\psi & \sin\psi \\ -\sin\psi & \cos\psi \end{bmatrix} \tag{2.54}$$

where ψ is the angle with respect to the north in clockwise direction. Thus, the control law can be rewritten as:

$$\begin{bmatrix} \theta_d \\ \phi_d \end{bmatrix} = R_z \begin{bmatrix} U_x \\ U_y \end{bmatrix} \tag{2.55}$$

2.4.2 Manipulator Controller

In the design of a controller for an aerial manipulator, the mechanics of the arm joints is one of the main system features to take into account. Typically, we found robot

arms with rotational rigid joints (Jimenez-Cano et al., 2013). However, there are some examples of aerial manipulators with prismatic joints (Mersha et al., 2014) and, nowadays compliant joints are being also employed by researchers due to their benefits when the arm performs environment contact tasks, (Suarez et al., 2015), (Yüksel et al., 2015) (Bartelds et al., 2016) (Suarez et al., 2018a) (Suarez et al., 2018c). Other consideration to keep in mind must be if the actuators are controlled in torque or directly in position, velocity or acceleration. Most robot arm controllers found in the literature were designed for actuators which are controller in torque (Villani et al., 2000). To design the manipulator controller we start from the dynamic model of the full system. From 2.42 the matrix equations of motion for the manipulator can be expressed as:

$$M_m\ddot{\gamma} + C_m + G_m = \tau_\gamma + \tau_{ext}^{\gamma} - M_{am}^T \begin{bmatrix} \ddot{p} \\ \ddot{\eta} \end{bmatrix} \tag{2.56}$$

Now, let us focus on the end-effector of the manipulator as reference. Then using the operational space formulation (Khatib, 1987), the end-effector equations of motion in operational space can be written as:

$$\Lambda(\varphi)\ddot{X}_E + \mu(\varphi,\dot{\varphi})\dot{X}_E + \varrho(\varphi) = \Gamma \tag{2.57}$$

where $\Lambda(\varphi)$, $\mu(\varphi,\dot{\varphi})$ and $\varrho(\varphi)$ represent the inertia matrix, the end-effector centrifugal and Coriolis forces and the vector of gravity forces. And their relationships with the equations of motions of the system can be expressed are given by,

$$\begin{aligned} \Lambda(\varphi) &= J_{se}^{-T} M_m J_{se}^{-1} \\ \mu(\varphi,\dot{\varphi}) &= J_{se}^{-T} C_m - \Lambda(q) h(\varphi,\dot{\varphi}) \\ \varrho(\varphi) &= J_{se}^{-T} G_m \\ h(\varphi,\dot{\varphi}) &= \dot{J}_{se}\dot{\varphi} \end{aligned} \tag{2.58}$$

Herein, J_{se} is the so-called Jacobian of the system and it is used to relate the position and orientation of the end-effector, $X_E = [x, y, z, \phi, \theta, \psi]_E^T \in \mathbb{R}^6$ and the generalized coordinates of the system, φ. This relationship is given by

$$\dot{X}_E = J_{se}(\varphi)\dot{\varphi} \tag{2.59}$$

Finally, using 2.57 and 2.58, it is possible to obtain the relationship between the generalized forces as,

$$\tau_M = J_{se}^T(\varphi)\Gamma \tag{2.60}$$

which represents the relationship between the operational forces in the Cartesian space and the joint forces in accord with the multirotor and manipulator system equation and the end-effector equations. Using this model and if we can estimate the external forces, we could implement a cartesian impedance control, (Lippiello and Ruggiero, 2012). Considering the cartesian coordinates vector for the end-effector, X_E. Thus, we can derive the equation 2.59, obtaining the following result:

$$\ddot{X}_E = J_{se}(\varphi)\ddot{\varphi} + \dot{J}_{se}(\varphi)\dot{\varphi} \tag{2.61}$$

Then, defining an actual position error as $e_X = X_d - X_E$, where X_d is the desired position that the end-effector must reach, the control law can be defined

$$U_\gamma = g(\varphi) + J_{se}^\top(\Lambda(\varphi)\ddot{X}_d - \mu(\varphi, \dot{\varphi})\dot{X}_d + K_d\dot{e_X} + K_p e_X) \tag{2.62}$$

where K_p and K_d are symmetric and positive definite matrices of stiffness and damping. In the most aerial manipulator systems developed during this thesis, the robot arm mounted has smart servos such as Herkulex or Dynamixel. These smart servos are controlled in position with some velocity and acceleration configurations.Then, to apply the above control technique to these robot arms would require a system torque estimation as the complaint mechanism proposed in chapter 4. On the other hand, with the other aerial manipulator, we do not have the possibility of implementing a controller based in torque. Thus, to track the desired cartesian position of the desired

path, we have to solve the inverse kinematics. To accomplish this task, we have two options: through numerical methods or using equation 2.59. With the equation 2.59, we can design a first order CLIK (Closed-Loop Inverse Kinematics, (Chiacchio et al., 1991)) manipulator algorithm,

$$\dot{\varphi} = J_{se}^{\dagger} K_p e_X + (I - J_{se}\dot{J}_{se})\dot{\varphi}_0 \tag{2.63}$$

herein $J^{\dagger} = J^{\top}(JJ^{\top})^{-1}$ is the Jacobian pseudo-inverse. The equation 2.63 is used to implement a joint velocity control where $(I - J_{se}\dot{J}_{se})$ is the null-space and can be used to design constraints like to limit the arm workspace to avoid collisions or minimize the system centre of gravity movements to improve the platform stability.

Chapter 3

Applications (I). Aerial manipulators for grasping tasks

Chapters 3 and 4 describe the different applications in aerial manipulation developed during this thesis. We have divided the applications into two categories: aerial manipulators for grasping tasks, which are described in this chapter, and aerial manipulators for structure inspections, which will be presented in the next chapter. Furthermore, this coincides with the Framework of the European projects, ARCAS and AEROBI, in which this thesis has been developed. The ARCAS-Project objectives were the development of cooperative free-flying robot system for assembly and structure construction. The ARCAS systems used aerial vehicles (helicopters and quadrotors) with multi-link manipulators for assembly tasks. Compared to the previously published work, the use of multi-link manipulators has several advantages over the grasping mechanisms used in most developed systems. The arm allows for greater flexibility in the kind of tasks that can be done, not only grasping objects but also manipulating them, as mounting pieces, fastener installation, inspection by contact, etc. Furthermore, the extra degrees of freedom of the arm can be used to compensate the oscillations and perturbations that are always present in aerial vehicles, to stabilize the position of the tool and to accommodate the effect of contact forces and torques in the assembly tasks. The objectives of the AEROBI Project were the use of aerial manipulators for structure inspection and we will go deeper into this project in the next chapter.

In this chapter, we will focus on the aerial manipulators with multi-link arms for grasping tasks. First, we will study the AMUSE system. This prototype consisted of a multirotor equipped with a commercial multi-link arm and was developed during the ARCAS FP7 European Project. In this project, the AMUSE prototype was used to done grasping tasks in outdoor experiments. We will present its development, starting with the first prototypes, and its implementation and proposed controller. We will also show the outdoors experiments done. Furthermore, we will also analyze the techniques implemented in AMUSE but for a helicopter's case and presenting the simulation results.

3.1 Application 1 ARCAS - Multirotor with rigid joints arm

This section presents the AMUSE aerial manipulation system, its design, control scheme and experiments done. The AMUSE born as an evolution of the QARM1 prototype (see Figure 3.1). The QARM1 aerial robot was a quadrotor with a 3-link light manipulator arm developed by GRVC at University of Seville and CATEC. It was one of the first prototypes developed at the beginning of ARCAS and was used to carry out studies about the dynamic behavior of the system when the arm does any movement. This prototype was a quadrotor that had a standard configuration with four electric motors with fixed-pitch propellers at the ends of two crossbars. The quadrotor gross weight was 980 g. including batteries, controller and sensors. It had a three-link manipulator arm attached at the center of its belly between the two skids. The manipulator weight was 400 g. and it had 200 g of payload.

The QARM1 had a controller board based on the Arducopter design with a 16 MHz ATMega2560 microcontroller, and a sensor board with three-axis MEMS accelerometers and gyros, and a single frequency GPS receiver. The manipulator arm has been specially designed and built for this purpose, given the payload limitations of the quadrotor. The main design criteria that have been considered are to minimize the displacement of the center of gravity and the total arm weight, and maximize the

Figure 3.1: (Left)QARM1 quadrotor with three links manipulator arm developed by the University of Seville and CATEC (Seville). (Right) AMUSE octoquad aerial manipulator developed at University of Seville (AMUSE).

load to weight ratio. The different parts of the arm have been built from polymer powder by Rapid Manufacturing.

Figure 3.2: QARM1 manipulator design.

The arm has four main parts (see Figure 3.2). The base is attached to the quadrotor belly, and it includes the control electronics and the two servos that drive the first two joints, to minimize the displacement of the center of mass. The two first links are made of lattice structure to minimize weight. The first link is designed so that it can accommodate the second bar when folded, and in this rest position the center of mass of the QARM1 is centered at the quadrotor geometric Z axis. At the end of the second link is the servo that drives the end effector, which has a neoprene sheet added at the contact area to facilitate gripping of the pieces.

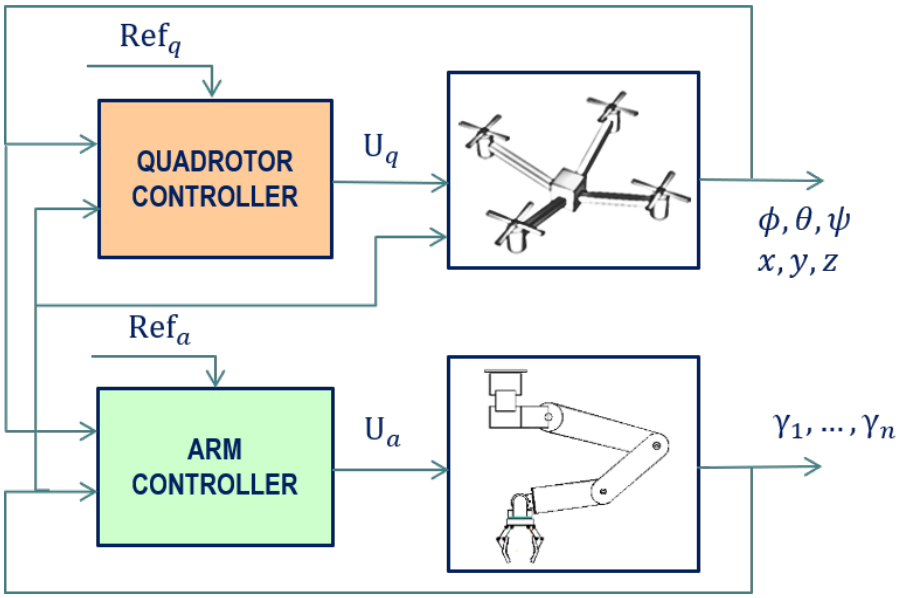

Figure 3.3: Control Scheme of the QARM1

The control scheme considered for the QARM1 is shown in Figure 3.3. The quadrotor controller block is responsible for attitude and position control of the quadrotor. The arm joints variables are used in this controller to compensate for the motion of the arm. For control design purposes, the quadrotor model is considered as a standard quadrotor plus an articulated body, which causes the center of mass to be displaced from the geometric Z axis of the quadrotor and modifies the inertia, and both of them are dependent on the arm joint angles. On the other hand, the arm controller block takes as inputs the state coordinates of the quadrotor, and it commands the motors of the arm to try to compensate for the motion of its base (quadrotor), so that the Tool Center Point (TCP) or end effector of the manipulator maintains the desired position (to grab and release objects),or follows a predefined trajectory. Extensive simulation tests and also outdoors experiments were done to validate the control scheme proposed. The results of these tests have been published in (Jimenez-Cano et al., 2013) (see Figure 3.4).

Thanks to the experience with QARM1, the next step was the design of an aerial manipulator for outdoors with more payload and with a manipulator arm with better handling capabilities, which is the AMUSE (Aerial Manipulator of University of

Figure 3.4: QARM1 prototype during flight experiments.

SEville). The next subsections present a system description of AMUSE, the control scheme and the outdoor validation experiments.

3.1.1 System Description

The AMUSE aerial platform is a multirotor with eight rotors located at the ends of a four-arm planar structure, with two rotors positioned coaxially at the end of each arm, which is usually known as "octoquad" configuration. The reason to use eight rotors is to get enough lift and payload for the application. Each pair of coaxial rotors rotates in opposite directions to compensate the torque at each arm. The octoquad has been preferred over the standard octocopter configuration (eight rotors distributed in the same plane) because it is more compact, and it is better suited to fly close to objects or other obstacles. The AMUSE octoquad aerial platform has been designed to get additional payload so that the sensors and control computer needed to operate outdoors and a multilink manipulator arm with enough payload can be mounted. The AMUSE mounts eight $750W$ motors, model Kopterworx KW10, with 16" rotors. The maximum thrust of each rotor is 3300 g. and it has 187 g. of weight. The rotors are located at $41cm$ of the center on each of the four bars. The AMUSE total payload is about 8 kg, which is available for sensors, processing hardware, the manipulator arm and the arm payload.

Manipulator arms for aerial robots have strong weight limitations given the limited payload of these aerial vehicles. Usually the main design criteria are to minimize the

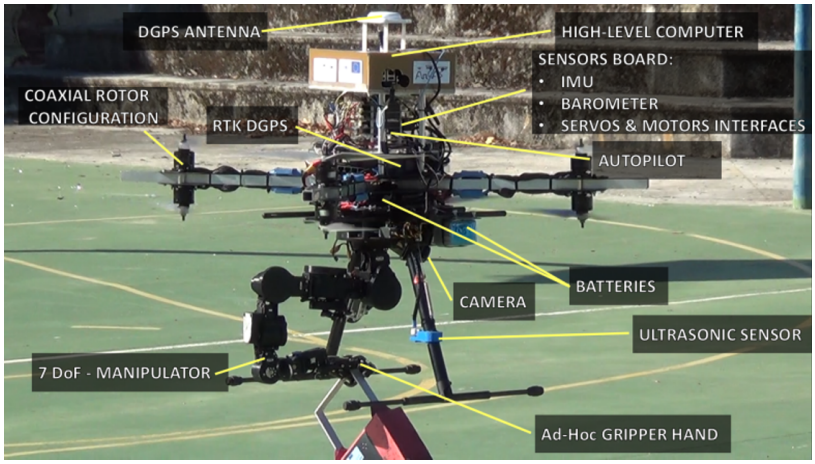

Figure 3.5: AMUSE control computers and sensors for outdoor operation.

total arm weight, maximize the load to weight ratio and minimize the displacement of the center of gravity when the arm joints move, to facilitate control of the robot. Figure 3.5 presents the AMUSE with a 7-DoF arm developed by Robai (model Cyton Gamma 1500) and the sensors and systems mounted. In this case, the use of a commercial arm was due to the excellent specification in the relationship reach/payload of the Robai model and that with 7-DoF it has better manipulability than the other configurations. Moreover, the maximum payload is 1.3 kg, which is well suited for a large set of applications. In the Cyton Gamma 1500 robot arm, each joint is actuated by a smart servo (Dynamixel) that can provide position, speed, load, voltage and temperature feedback information. The 7-DoF make the Cyton arm kinematically redundant. The extra degree of freedom gives more manoeuvrability and the ability to reach around obstacles. The general specifications of the arm are presented in Table 3.1.

To achieve better manipulation capability, the Robai gripper was substituted by a custom design developed at the University of Seville. The new gripper consists of three fingers actuated by tethers and springs which simulate the tendons of a finger. This design allows more versatility to grasp objects with different shapes. Moreover, it has a large size grip zone which improves the grasping capability when the position accuracy is low. The gripper developed is shown in Figure 3.6

Table 3.1: Cyton Gamma 1500 arm general specifications.

Parameter	Value
Total weight	2 kg
Payload (full-range)	1.3 kg
Payload (mid-range)	2 kg
Maximum reach	0.68 m
Footprint	0.15m×0.15m
Repeatability	±0.005 m

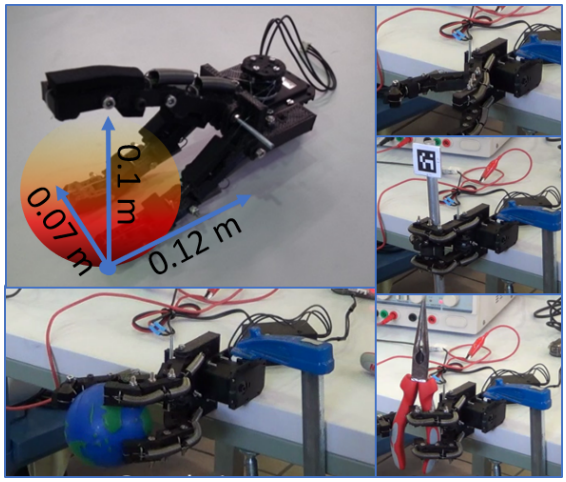

Figure 3.6: AMUSE hand designed and developed at University os Seville. This design was published in (Suarez et al., 2016).

The AMUSE mounts an Autopilot designed and developed by CATEC. This autopilot consists og a BeagleBone White computing board connected through a vertical bus with a sensor shield. The sensor shield mounts a Cortex M3 which is responsible for managing sensors measurements, devices inputs (UARTs and I2Cs) and PWM outputs. The sensor shield incorporates an IMU ADIS16407, a GPS Ublox 6 and two inputs with Futaba SBUS compatibility. This shield is also used as an interface with the Beaglebone White and to communicate it with the Robai robot arm. The Beaglebone White is an embedded PC developed by Texas Instrument which uses an ARM Cortex-A8 and incorporates a 256MB DDR2 RAM memory, two USB

ports, Ethernet 10/100, etc. The CATEC autopilot uses QNX Operative System and it allows to design and develop custom control techniques using MATLAB/Simulink. Moreover, using Simulink external mode the data logs can be seen and analyzed in real time, and even parameters like the control gains can be modified in real time during the experiments.

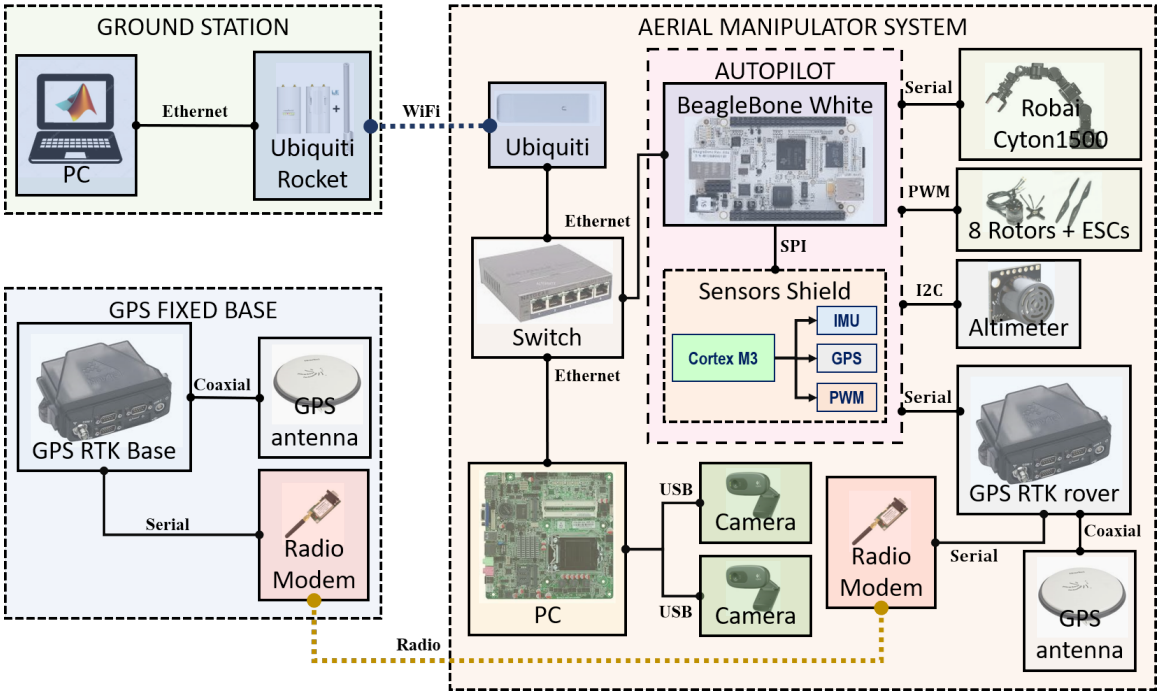

Figure 3.7: Hardware Scheme implemented in AMUSE.

The Autopilot is connected through an Ethernet link to the High Level Computer (HLC), which is an Intel i7-based PC. Furthermore, several cameras can be also connected to the HLC (see Figure 3.7). One of the cameras is mounted on the end effector and it is used for visual servoing and relative positioning of the objects that are being manipulated. The second camera shown in Figure 3.8 is attached to the octoquad frame pointing down, and it is used for relative positioning and hover flight stabilization, aiding the RTK-DGPS and complementing it when it is not available in high accuracy mode. A third camera for positioning can be also mounted on the frame pointing down on the other side of the frame (not shown in Figure 3.8).The HLC runs 64 bits Ubuntu server with ROS (Robot Operating System (Quigley et al.,

2009)). It also has installed the ARUCO library (Munoz-Salinas, 2012), which can detect different markers in real time. Markers can be placed in objects that are being manipulated, or on ground near interest areas for aiding in positioning.

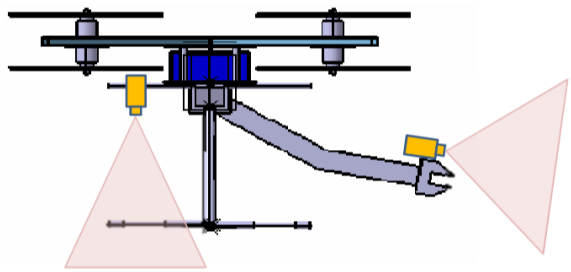

Figure 3.8: AMUSE octoquad with two cameras: one on the end effector for object recognition and another one mounted on the frame for positioning.

To help in the positioning system, a Novatel GPS-RTK has been also incorporated to the system. In this system a GPS-RTK device (Rover) is located onboard and it is communicated with a GPS-RTK device that is located outboard as a fixed base. This GPS system allows an accuracy of about 2 cm. The communication between the rover and the base are done thanks to two radio modems at a baudrate of 115200. The Rover is also connected to the autopilot through a serial port. An ultrasonic altimeter is also connected by I2C to the autopilot. The ground station and AMUSE aerial manipulator are communicated by WiFi using an Ubiquiti M5 at 5 GHz. A scheme of the full hardware system is shown in Figure 3.7

3.1.2 Modelling and Control

As was introduced in chapter 2, the dynamic model can be derived either using the Lagrange-Euler Formalism or the Newton-Euler recursive formulation. Defining the vector of generalized coordinates as $\varphi = (p, \eta, \gamma)^T \in \mathbb{R}^{13}$, where the joint coordinates vector of the Robai arm is given by $\gamma = (\gamma_1, ..., \gamma_7)^T \in \mathbb{R}^7$. Thus, following one of these methods, the dynamic equations in compact matrix form are given by:

$$M(\varphi)\ddot{\varphi} + C(\varphi, \dot{\varphi})\dot{\varphi} + G(\varphi) = \tau + \tau_{ext} \tag{3.1}$$

where the vector τ encompasses actuator forces and torques exerted by the octoquad rotors and the servo actuators of the arm joints, and τ_{ext} includes external forces. Since the inertia matrix is invertible, the following holds:

$$\ddot{\varphi} = M(\varphi)^{-1}[\tau + \tau_{ext} - C(\varphi, \dot{\varphi})\dot{\varphi} - G(\varphi)] \tag{3.2}$$

Multirotor Controller

The AMUSE octoquad controller is adapted from the Variable Parameter Integral Backstepping (VPIB) controller that was presented in chapter 2. It is a nonlinear controller obtained through backstepping with an added integral term, with guaranteed stability. The multirotor controller terms depend on the manipulator arm joint positions and velocities, and thus the parameters and gains of the controller vary when the arm moves. Next, the derivation of the pitch attitude controller will be presented. The controllers for the other angles are built in a similar way. Consider the tracking error $e_\eta = \eta_d - \eta$, where η_d is the desired attitude and its dynamics:

$$\frac{de_\eta}{dt} = \dot{\eta}_d - \omega \tag{3.3}$$

Then a virtual control over the angular speed ω can be formulated, which is not a control input. Therefore, the desired angular speed can be defined as follows:

$$\omega_d = k_\eta e_\eta + \dot{\eta}_d + \lambda_\eta \chi_\eta \tag{3.4}$$

with k_η and λ_η are positive diagonal gain matrix and χ_η are the integral of each tracking attitude angle error. Next, the angular velocity tracking error $e_{\dot{\eta}}$ and its dynamics can be defined by:

$$e_{\dot{\eta}} = \omega_d - \omega \tag{3.5}$$

$$\frac{de_{\dot{\eta}}}{dt} = k_\eta(\dot{\eta}_d - \omega) + \ddot{\eta}_d + \lambda_\eta e_\eta - \ddot{\eta} \tag{3.6}$$

Using 3.4, 3.5 and 3.6 the attitude tracking error dynamics equation 3.3 can be rewritten as:

$$\frac{de_\eta}{dt} = -k_\eta(e_\eta - \lambda_\eta e_\eta + e_{\dot{\eta}} \tag{3.7}$$

Now, $\ddot{\eta}$ in 3.5 and 3.6 can be replaced by its expression in the dynamic model 3.2, and the control input U_η appears explicitly. Then, combining the tracking errors of position e_η and the angular speed $e_{\dot{\eta}}$, and the integral position tracking error χ_η using the above equations the control input U_η can be calculated as:

$$U_\eta = M_\eta^*(\gamma)[(1 - k_\eta^2\lambda_\eta)e_\eta + (k_\eta + k_{\dot{\eta}})e_{\dot{\eta}} - k_\eta\lambda_\eta\chi_\eta] - D_\eta(\varphi, \ddot{\varphi}) - C_\eta(\varphi, \dot{\varphi}) - G_\eta(\varphi) + \tau_{\eta,\gamma} \tag{3.8}$$

where $k_{\dot{\eta}}$ is a diagonal positive gain matrix which determines the convergence speed of the angular speed loop. In practice, the attitude controller terms can be rearranged in the following way:

$$U_\eta = M_\eta^*(\gamma)[K_P e_\eta + K_I\chi_\eta + K_D e_{\dot{\eta}}] - D_\eta(\varphi, \ddot{\varphi}) - C_\eta(\varphi, \dot{\varphi}) - G_\eta(\varphi) + \tau_{\eta,\gamma} \tag{3.9}$$

where K_P, K_I and K_D are the parameters of a standard PID controller, $M_\eta^*(\gamma)$ is a variable gain that depends on the arm joint angle positions, and D_η, C_η and G_η are the nonlinear terms described above. The first part of the controller can be seen as a gain-scheduled PID with the different positions of the arm, while the nonlinear terms compensate the full coupled dynamic effects. In this way, it is easier to tune the controller parameters starting from the standard PIDs that are used by many multicopters as base controllers. The expression of the position controller can be derived in a similar way.

$$U_p = M_p^*(D(R_\eta e_3))^{-1}[K_P e_p + K_I\chi_p + K_D e_{\dot{p}}] - G_\eta(\varphi) \tag{3.10}$$

Manipulator Controller

The controller for the manipulator arm joints could be derived in the same manner that the multirotor controller from the dynamic equations of motion, thus obtaining the required torques τ to drive the motors of the arm joints. This approach has been

followed in (Lippiello and Ruggiero, 2012) and Huber et al. (2013), which use a torque based impedance controller for interaction with objects in the environment. However, there are practical limitations in the manipulator arm design that prevent its use. As stated above, arms used for aerial manipulation have strong weight restrictions,due to the payload limitations of the aerial platforms. The prototype arms that have been designed for the AMUSE use standard servos or Robotis Dynamixel servos to drive the joints. This is also the case with many other arms designed for aerial manipulation (Cano et al., 2013). Although some of the larger Dynamixel servos have the possibility of joint torque control, torque sensing has poor accuracy, making very difficult if not impossible to implement torque control. The AMUSE manipulator arm implements an admittance controller, which is a position-based Cartesian impedance controller. The admittance controller will command a desired Cartesian position $\sum_d$ for the end effector Tool Center Point (TCP):

$$\sum_d = \sum_{TCP} + \sum_{int} \tag{3.11}$$

where $\sum_{TCP}$ is the TCP position defined by the manipulation task and trajectory interpolation, and $\sum_{int}$ is the additional displacement that would get the desired interaction forces and torques between the end effector and the objects or the environment, calculated by the admittance controller. Then, $\sum_d$ is transformed through the manipulator inverse kinematics K^{-1} and the desired joint position setpoints are transmitted to the local joint embedded controllers. For the inverse kinematics a Jacobian-based first-order algorithm has been used. This algorithm minimizes the operational space error between the desired and the actual end-effector position and orientation, overcoming drift problems induced by other differential kinematics schemes. Additionally, internal motions have also been generated through the Jacobian null space to force a prescribed configuration of the manipulator for a given end-effector position and orientation. Thus, a strategy to minimize the distance from mechanical joint limits has been considered. Finally, to provide a robust behavior crossing through or close to singular configurations a modified pseudoinverse with a variable damping

factor based on Gaussian-weighted functions of the manipulability measure has been used.

3.1.3 Experiments

A first set of experiments have been done with AMUSE to obtain estimations of the dynamic reaction torques and variation in moments of inertia generated by the movement of the manipulator. These tests have been useful to gain insight into the stability of the aerial platform and how it can be affected by these variable terms. Then, they have been very used to adjust the controller.

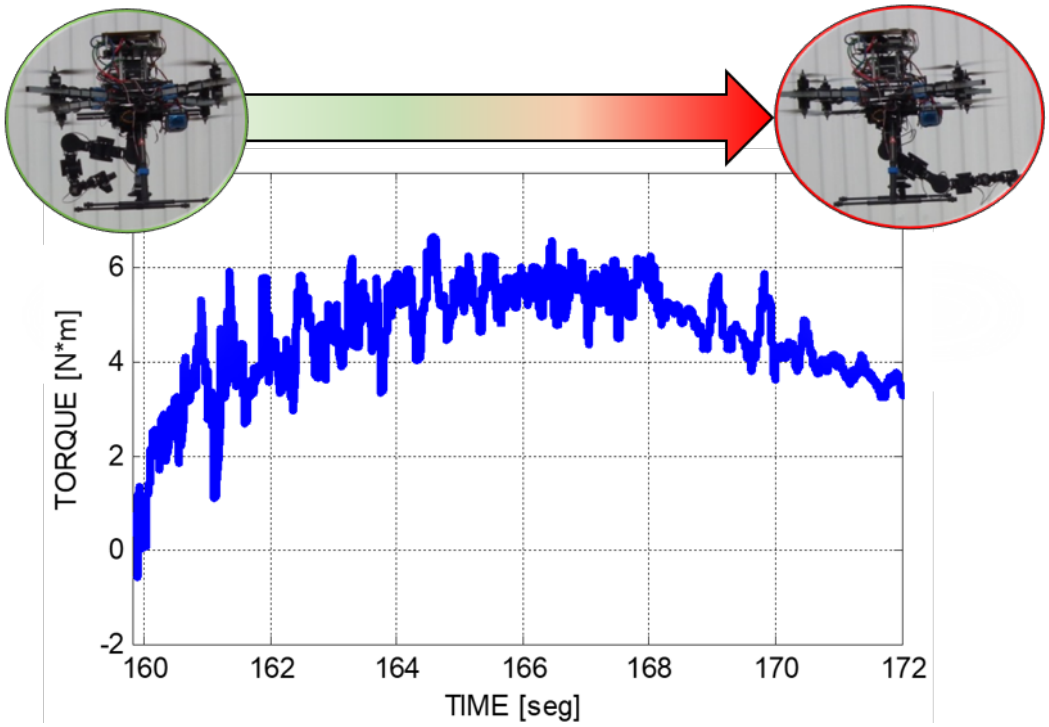

Figure 3.9: Dynamic reaction torque in base generated by movement of the arm.

The results of these experiments can be seen in Figures 3.9, 3.10 and 3.11. In detail, the dynamic reaction torque in the base of the arm is shown for a sample movement in Figure 3.9. The measurement noise that can be seen in the figure is due to the dynamic torque involves accelerations which are obtained using accelerometers. This

measurement must be filtered in case of use for control directly. Figure 3.10 presents the variation of the torque generated by the displacement of the center of mass in one of the tests, as a function of one of the joints (joint 2 which is representative of the movement of the arm). The arm moves from the initial take-off/landing position to an extended position, which are shown in the two pictures of Figure 3.10.

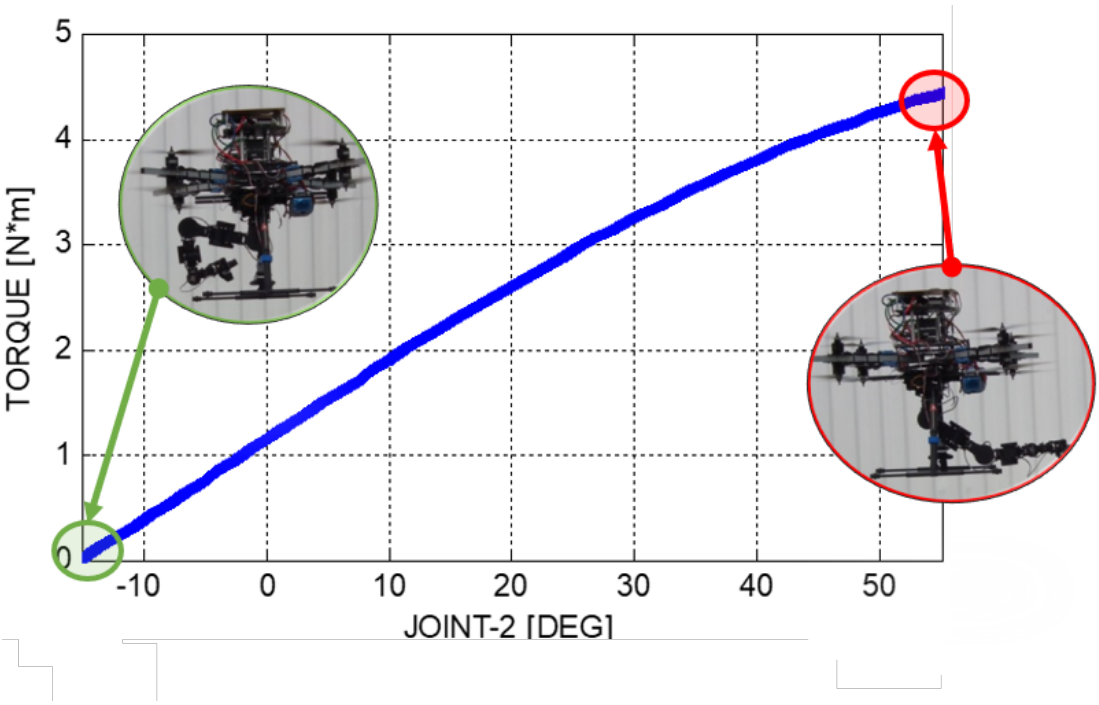

Figure 3.10: Torque generated by displacement of center of mass.

Another interesting data obtained by the experiments is the variation of the moments of inertia, which are presented in Figure 3.11 for the same movement of the arm of Figure 3.10. Figure 3.11 shows the variation of the main inertia moment I_{xx} and the cross-inertia moment I_{xz}, which are the most affected by the movement of the arm in this experiment. The maximum variation at terms of the principal diagonal of the inertia matrix is 5.36% and the maximum torque generated is $4.5Nm$.

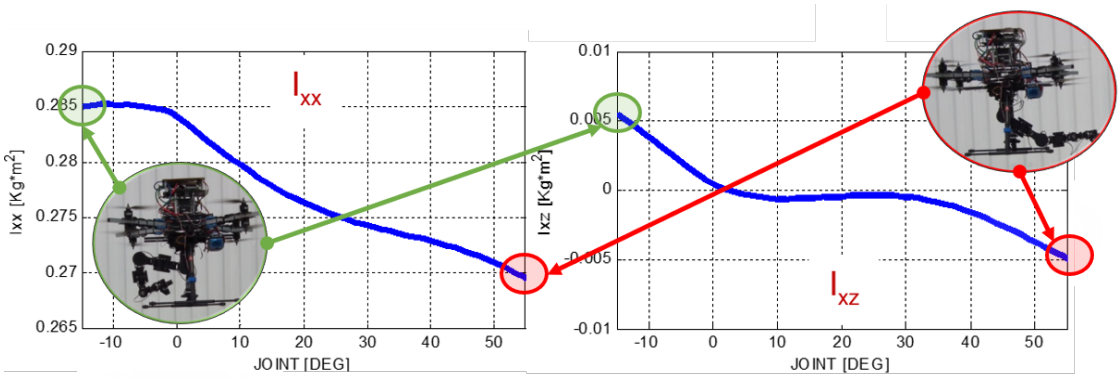

Figure 3.11: Variation of moments of inertia.

Outdoor Experiments with visual Feedback

Another set of experiments has been done to test the control approach using visual feedback in an outdoor scenario. Two cameras were mounted on the AMUSE platform: one for manipulation tasks and another one for multirotor positioning purposes. The manipulation camera was placed nearby the robot base pointing to the end-effector workspace. It was found the best location to minimize interference of the arm gripper with the localization targets. Other setups were tested such as assembling this camera to the end-effector gripper or mounting it on the last manipulator link. However, these configurations incurred on loss of accuracy due to several reasons: firstly the increase and amplification of camera movements and vibrations caused by the higher distance from de system's CoG (Centre of Gravity) and the full mechanical chain that, in fact, it is not a completely rigid body; secondly the error propagation because of the joint angle measurements. Mechanical vibrations are the source of several image issues such as blurring and distortions that may reduce visual recognition capabilities. On the other hand, the employment of joint angles needed to adjust the measurements of a camera placed on a manipulator increases positioning uncertainty.

The platform positioning camera was placed on the landing gear pointing towards the ground, far away enough from possible manipulator obstructions. The ArUco vision algorithm was implemented on the high-level computer. This algorithm computes

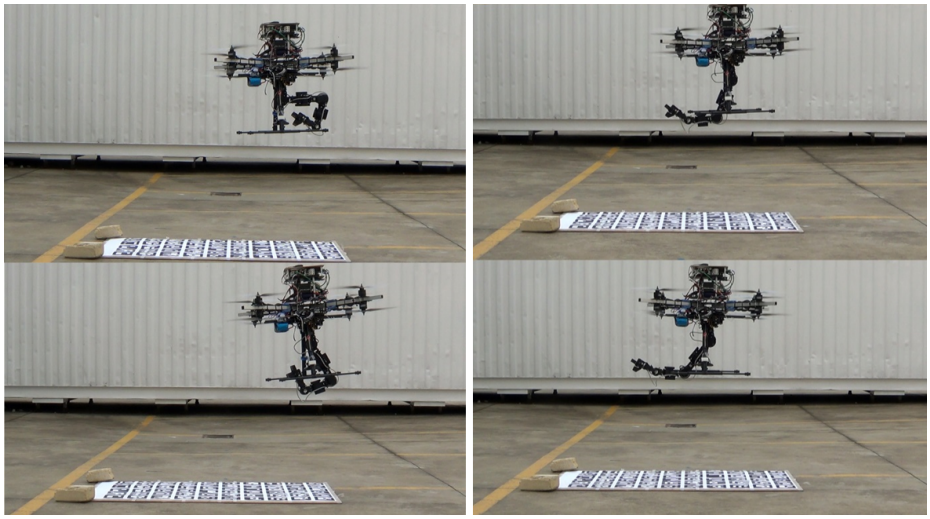

Figure 3.12: Controller comparison tests using board positioning.

camera position and orientation relative to a reference frame attached to a tag or a set of tags (board). In view of this, the target object (object to grasp) was provided with a single tag and a 2x2m board was placed on the ground (see Figure 3.12). In Figure 3.12, we can see a sequence of pictures of an initial experiment in which using visual feedback for positioning, the controller is tested, evaluating the system behavior when the arm is moving. Experiments have been performed with the backstepping controller and with a standard PID controller that does not take into account the movement of the arm. Figure 3.13 shows the evolution of the AMUSE multirotor pitch attitude angle during the experiments.

The X-axis is placed on the plane of the arm and the pitch angle is defined as the rotation of the multirotor in this plane around the Y-axis, which is perpendicular to the plane. Thus, the pitch angle is the most influenced by the movement of the arm in these experiments. The shadowed areas in Figure 3.13 represent the movement of one of the arm joints (joint 3, which is moving up to 75 deg/s). Several arm joints were moving at the same time during the experiments. Just for the sake of clarity, the shadowed area has been included as an indication of the arm movements. In the right plot of Figure 3.13, it is shown the evolution of the pitch angle with the PID controller. When the arm is not moving and centered, the pitch angle presents oscillations of

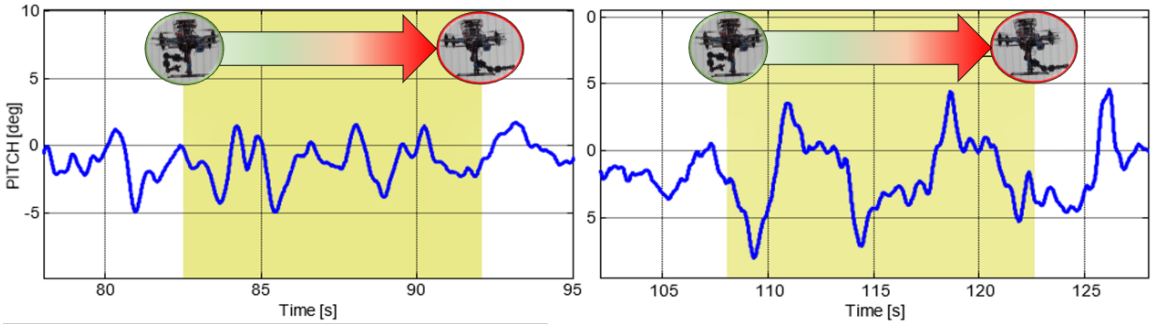

Figure 3.13: Evolution of the AMUSE pitch attitude angle during the experiments. Right plot: with a standard PID controller which does not consider the arm movement and dynamics. Left plot: with the full dynamics backstepping controller.

about 5-5.5 degrees of amplitude, which are due to the atmospheric perturbations and the action of the controller (this is common to both controllers). But when the arm begins to move, the oscillations with the PID controller grow rapidly to around 12 degrees. The left plot of Figure 3.13 shows the time evolution of the AMUSE multirotor with the proposed controller in the same experiment. It can be seen that, when the arm moves, oscillations increase only slightly to 6-6.5 degrees. Thus, the proposed controller is able to effectively counteract the movement of the arm even during large extents.

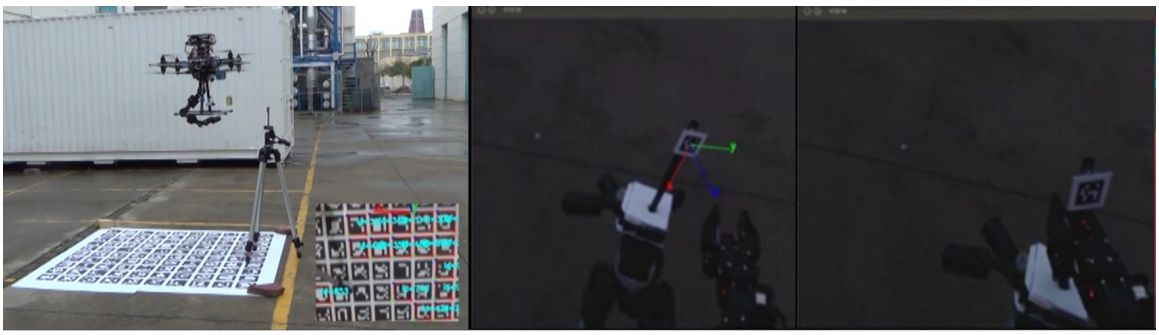

Figure 3.14: Left: structure bar with a marker at its base (indicated in the photo with a yellow arrow). Right: relative pose recognition performed by ARUCO, including relative position and orientation.

In a second round of experiments, the target was placed on a tripod next to the board where multirotor was going to hover. The manipulator was commanded to

grasp the bar while the whole platform was hovering counteracting the manipulator effects. Figure 3.14 shows a sequence of pictures of this test.

Outdoor Experiments with DGPS

Also, a set of experiments has been performed in an outdoor scenario with the DGPS sensor for positioning. These experiments have been divided into three subsets which were the steps that have been followed to test the control law implemented at our platform. The subsets have been called: Hover, Tracking, and Aerial Manipulation in Hover.

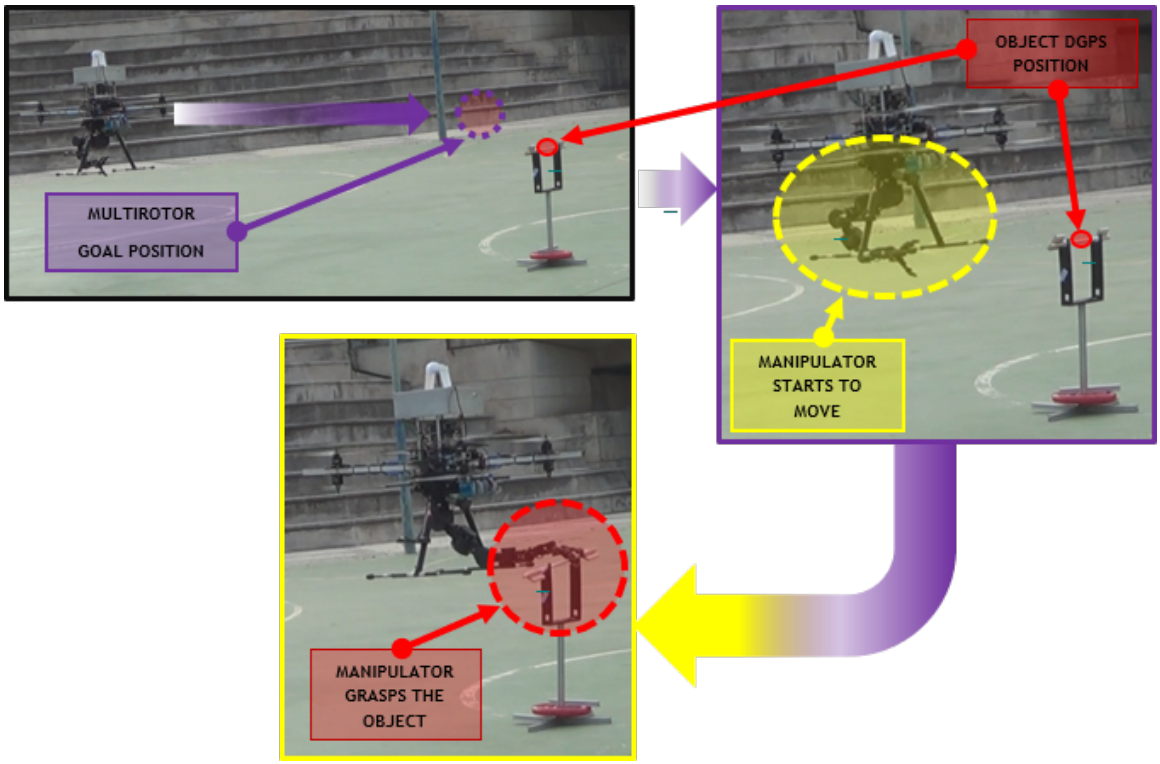

Figure 3.15: Outdoor experiments of AMUSE.

Figure 3.15 shows a sequence of pictures of the complete task, where, first, the multirotor arrives at the desired position close to the target and second, it grasps an object while is in hovering. To carry out these tasks, we have completed the above-mentioned steps, whose results are described in the following.

A. Hover experiments

The first step was to test if the AMUSE platform was able to hover at the desired position with the least possible errors, and test if the controller can reject the typical outdoor perturbations due to wind gusts or the degradation of position accuracy due to loss of satellites by the DGPS receiver. During these tests the manipulator was held at a fixed position. An example from these experiments can be seen in Figure 3.16.

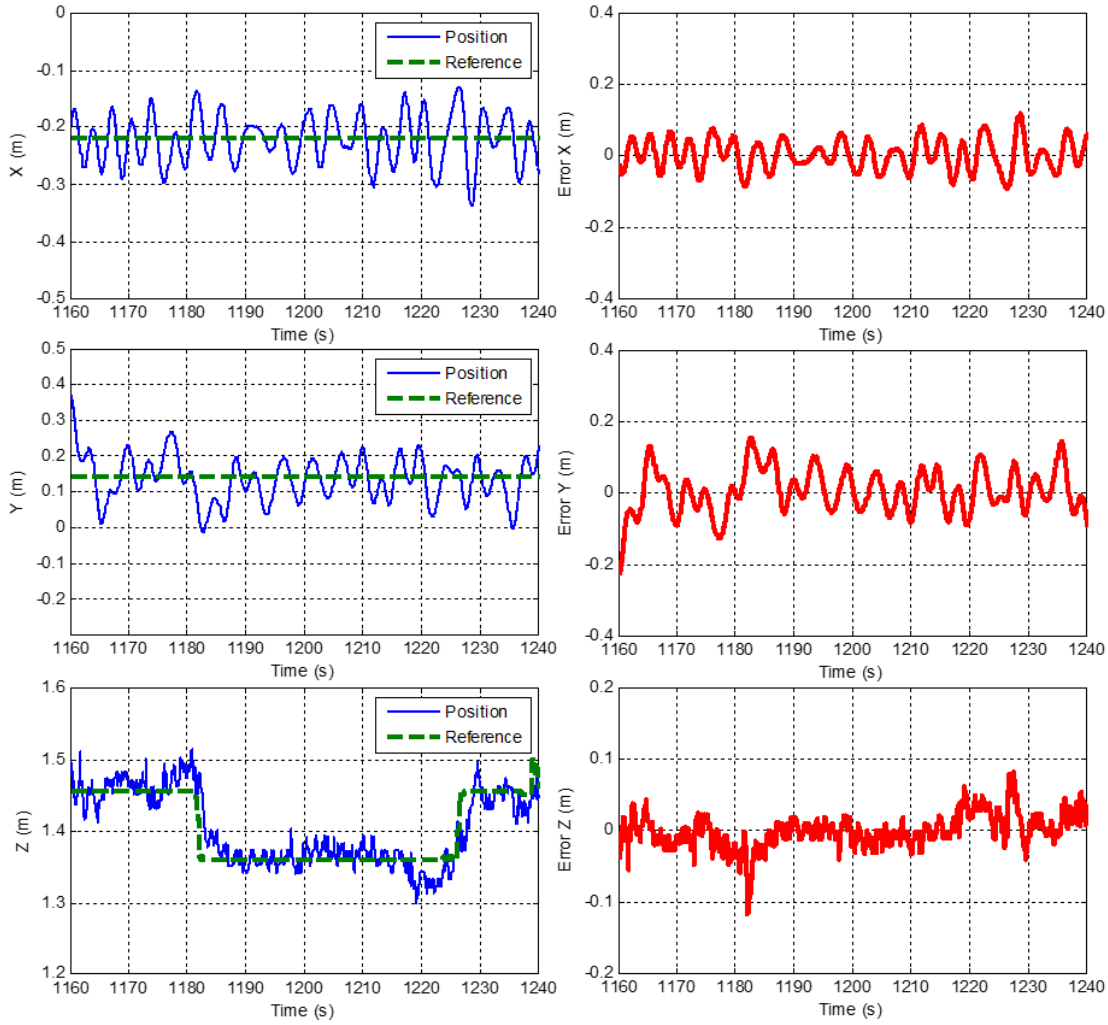

Figure 3.16: AMUSE position and errors in hover.

An object should be at the workspace of the robotic arm to be grasped. In aerial manipulation, this means that the multirotor should be oscillating on the desired

position in the range of the manipulator and the oscillations should be slow enough to be compensated by the manipulator. Figure 3.16 shows the results of an outdoor experiment with variable wind gusts of up to $12km/h$. The multirotor was commanded to stay at hover, and change altitude at some time instants while maintaining the horizontal position. The maximum errors obtained in this test have been about $\pm 8cm$ approximately in X and Y axes when maintaining altitude, and a bit larger when changing altitude. The Z errors were smaller, of about $\pm 4 - 5cm$ most of the time, except when changing altitude.

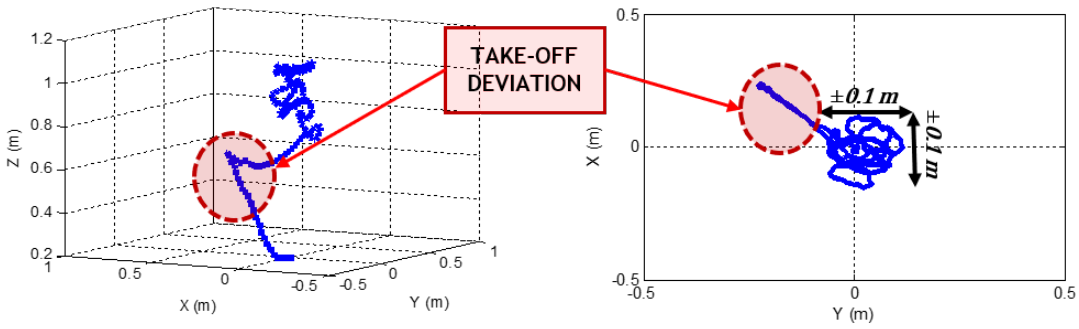

Figure 3.17: Take-off and hover experiments.

Figure 3.17 shows the 2-D and 3-D trajectories of another experiment in which the AMUSE was commanded to take off and maintain hover at a fixed point.

B. Trajectory tracking experiments

Another set of experiments has been done to test the capability of the AMUSE to track a desired straight trajectory with the controller. The result of one of the experiments is shown in Figure 3.18, where the reference trajectory is shown in dashed green and the AMUSE trajectory in blue. Figure 3.18(right,bottom) shows another experiment in which the AMUSE is commanded to track a trajectory and then maintain hover at the end point of the trajectory. These results show, the position accuracy flying with a DGPS. In the next, we evaluate if flying with this accuracy, our system can achieve to grasp an object.

C. Aerial Manipulation in Hover

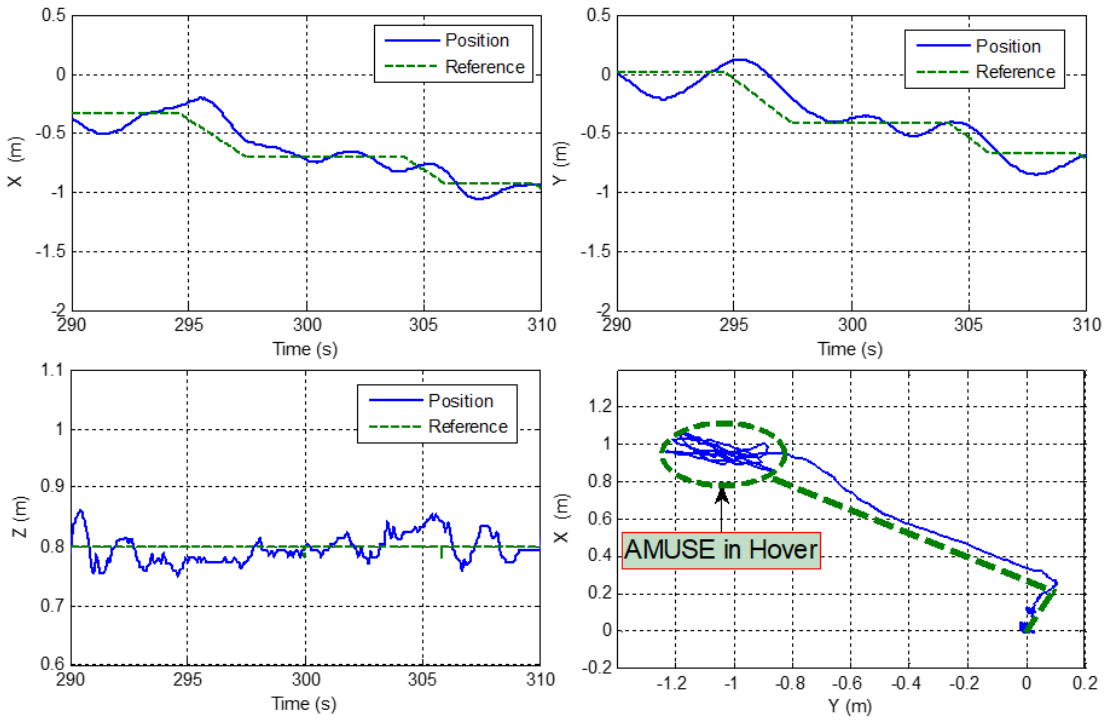

Figure 3.18: Traking a trajectory.

The last experiments subset shows tests where the multirotor is flying in hover and compensating the effects of the movements of the manipulator. The platform stability is maintained and position errors are sufficiently small so that the object can be maintained in the manipulator range and the arm controller can compensate for the position errors. In these experiments, the positioning system used by the AMUSE is a DGPS-RTK. The position of the tube is communicated to the autopilot in GPS coordinates. The autopilot calculates the relative position of the tube with respect to the arm base located in the aerial platform and aligned with its center of mass and it is transmitted to the arm controller. Figure 3.19(a) shows a sequence of pictures of these experiments. It is possible to see when the aerial manipulator is grasping a tube. Figure 3.19(b) presents the plots of the X and Y position coordinates, as well as the pitch and roll angles of the AMUSE multirotor in one of these experiments. The periods where the manipulator arm is moving approaching the object to grasp it are marked in the plots.

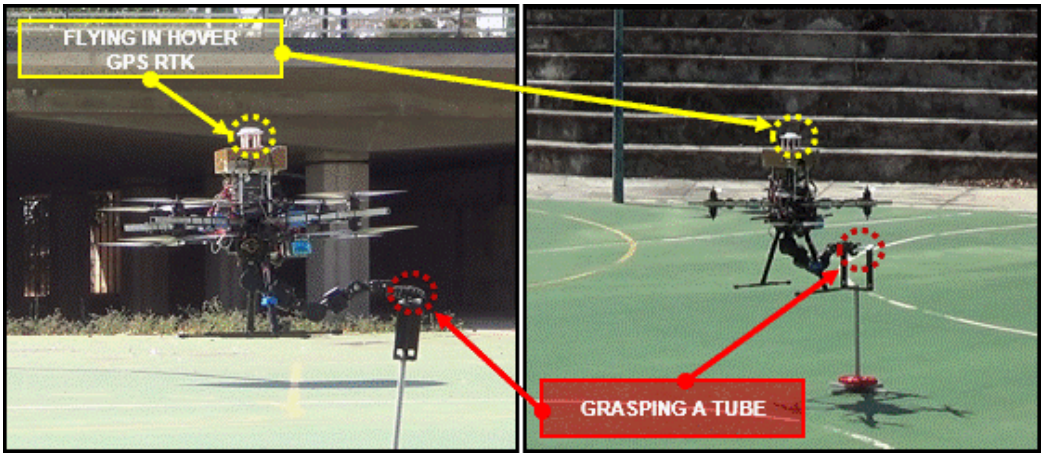

(a) Sequence of pictures of the experiments

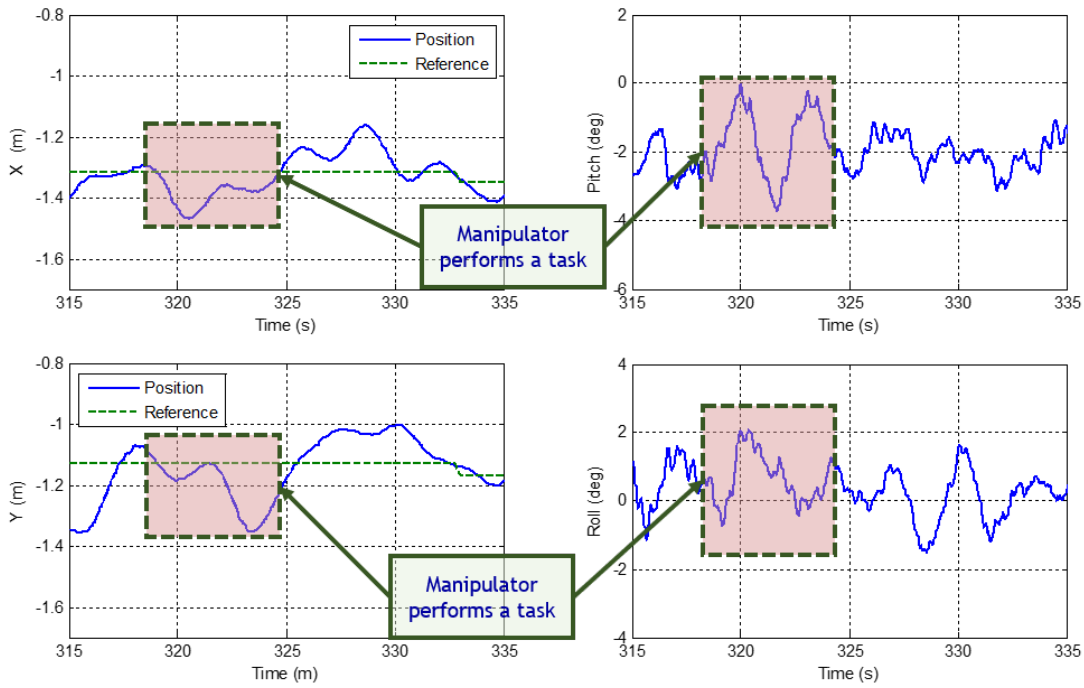

(b) Trajectory tracked by the AMUSE

Figure 3.19: Hovering and grasping experiments.

Integrated Experiments

A set of experiments where accomplished where the AMUSE performed a complete mission in a simulated radioactive scenario, as shown in Figure 3.20. A Geiger meter

was placed on this area where the AMUSE platform was aimed to recover that measurement instrument among all the wreckage material.

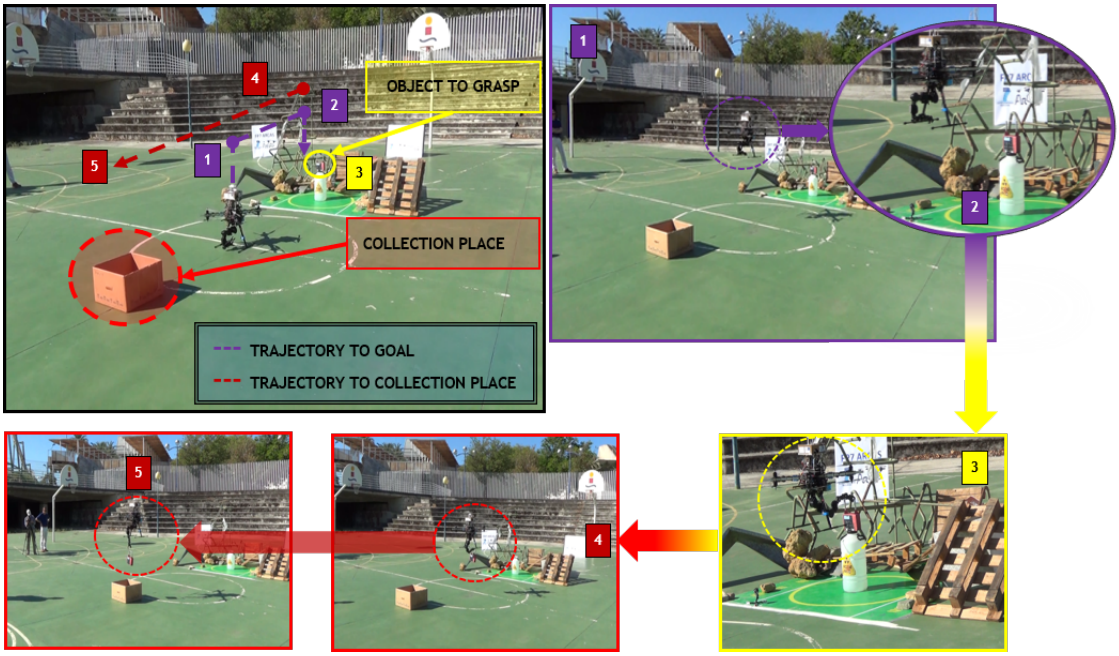

Figure 3.20: AMUSE experiments at a simulated radioactive scenario.

To this end, the AMUSE takes-off and starts a cruise flight to the grasping area (1). During this step, the manipulator remains in folded configuration. Once in the desired area, the multirotor starts to hover and the manipulator unfolds. After that, the flying platform slowly approaches the target (the Geiger meter) until the target is in the manipulator's workspace (2). Then, the manipulator EE approaches, grasps the instruments and moves away with it (3). After that, the manipulator folds to a safe configuration carrying the payload (4). Finally, the AMUSE starts a cruise flight to a collecting area where the payload is released by the manipulator (5). The results of these experiments were presented in the final report of the ARCAS project as the outdoor final experiments.

3.2 Application 2 ARCAS - Helicopter with multi-link arm

Owing to the good results obtained applying the control proposed in a multirotor with a robot manipulator, we decided to study this control technique for an aerial manipulator in which the aerial platform was a helicopter. This study was published in (Jimenez-Cano et al., 2016) and presented an elaborated model of the entire system as well as the implementation of the proposed controlled. Simulation experiments confirmed the validity of the proposed approach, and the results were also validated with a high-fidelity Modelica simulation model. Most works presented in the aerial manipulation use a multirotor as aerial platform. For example, several works use quadrotors with different gripping mechanisms for structure construction (Lindsey et al., 2011), whereas others like (Mellinger et al., 2011) and (Jiang and Kumar, 2013) consider cooperative quadrotors grasping and transporting loads. In (Mellinger et al., 2013) several lightweight, low-complexity grippers that allow quadrotors to grasp and perch on branches or beams and pick up and transport payloads are presented. The inertial parameters of the grasped object are estimated and used to adapt the controller and to improve performance during the flight. Furthermore, algorithms for quadrotor stabilization and force control are studied in (Orsag et al., 2013) and (Fumagalli et al., 2012) In (Kim et al., 2013) a quadrotor with an arm with two degrees of freedom was presented, and an adaptive sliding mode controller was designed. The control of an aerial multirotor with a manipulator has been also considered in (Korpela et al., 2012). Novel multirotor configurations have also been proposed: (Papachristos et al., 2014) developed a tri-tiltrotor UAV that is able to exert forces with a simple arm using thrust vectoring, (Nikou et al., 2015) presents a system that obtains the rotor configuration for a given manipulation task through optimization and (Rajappa et al., 2015) have presented a fully actuated hexarotor design with tilted propellers that is able to exert forces in all directions. Works using helicopters have been also presented like in (Pounds et al., 2011), where a small RC helicopter with a gripper is capable of grasping objects on the ground, or in (Kondak et al., 2013) and (Chmaj et al., 2013), where prototypes of helicopters with attached manipulators are also

presented. Experimental results of a helicopter equipped with fully actuated redundant manipulator arm were presented by (Huber et al., 2013). In this section, we present an adaptation of the control strategy introduced in chapter 2 for a helicopter with a multi-link manipulator. This adaptation is not straightforward since helicopters have stronger coupling between rotational and translational degrees of freedom than multirotors.

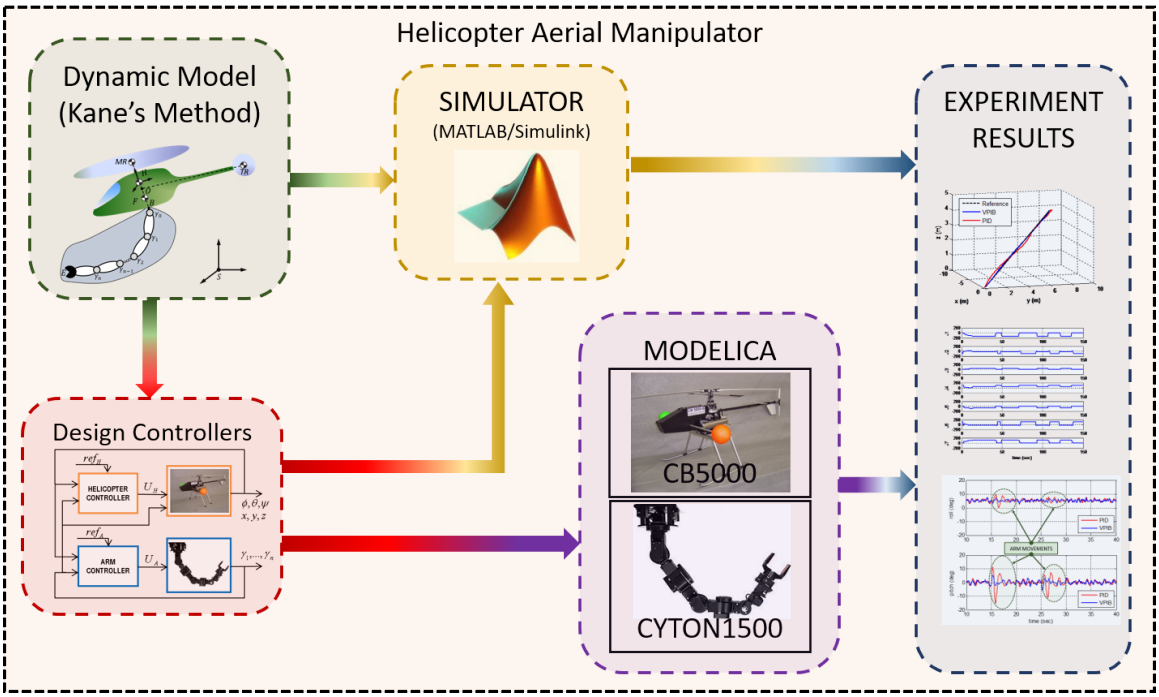

Figure 3.21: Scheme of the work developed for this case.

In the following, we develop the dynamic model for a helicopter with a 7-DoF robot arm through the Kane's method introduced in chapter 2. Then, we design a control law based in the controller proposed in chapter 2 and through a high-fidelity simulator developed in Modelica, we test the control approach. A scheme of the work followed to carry out this case can be seen in Figure 3.21.

3.2.1 Modelling and control

Helicopters are highly nonlinear systems with significant dynamic coupling. This dynamic coupling is attributed to the force and torque generation process. Following the dynamic model for helicopters described in (Sandino et al., 2011), a helicopter can be modeled as two rigid bodies. The main rotor is modelled as a solid thin disk rotating with constant angular speed Ω_{MR} and mass distribution equivalent to the rotating blades. and the inertia of both main rotor and fuselage is defined using inertia dyadics. Then, we will consider that a helicopter equipped with a manipulator is a mechanical system composed of $2+n$ interconnected rigid bodies: helicopter fuselage with mass m_F, main rotor with mass m_{MR} and n manipulator links (see Figure 3.22), where each link has a mass, m_i with $i = 1, ..., n$. We will define the inertial frame S, a frame H fixed to the helicopter's fuselage, a point O located at the intersection between the rotation axis of the main rotor and that joins the tail rotor to the fuselage and the frame B in the base of the manipulator.

Assumption 1 *The helicopter is symmetric in the lateral direction and therefore, the CoG of the fuselage is located on the rotation axis of the main rotor.*

The assumption 1 is consistent with a usual practice in small helicopters, in which the position of the center of mass is usually adjusted to be as close as possible to the rotor rotation axis placing appropriately the equipment (batteries, sensors, computers, etc.). This makes easier manual take-off and landing by a human pilot, which is done in many cases for safety reasons.

Following the definition for the generalized coordinates of an aerial manipulator introduced in chapter 3, we will define the position of the helicopter as $p = (x, y, z)^T$ and the velocities as $V = (u, v, w)^T$. The generalized coordinates corresponding to the helicopter rotation will be expressed by $\eta = (\phi, \theta, \psi)^T$ and represent to the Euler angles (roll, pitch, yaw). Finally the projections of the angular velocity of the system into frame H will correspond to $\omega = (p, q, r)^T$ and the arm's joint are represented by $\gamma = (\gamma_1, ..., \gamma_n)^T$. Then, the dynamic model is obtained using Kane's method introduced in chapter 2 and it is given by

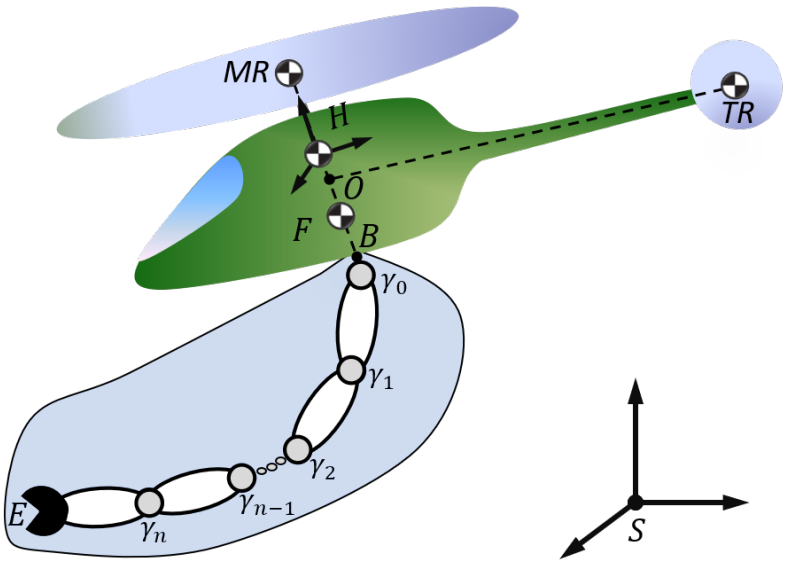

Figure 3.22: Helicopter with a manipulator arm: reference frames, centre of mass and dimensions of interest for modelling purposes.

$$
\begin{aligned}
M_T\dot{u} &= f_{MR}s_\theta - f_{TR}c_\theta s_\psi \\
M_T\dot{v} &= -f_{MR}s_\phi c_\theta + f_{TR}(c_\phi c_\psi - s_\phi s_\theta s_\psi) \\
M_T\dot{w} &= -gM_T + f_{MR}c_\phi c_\theta + f_{TR}(s_\phi c_\psi - c_\phi s_\theta s_\psi) \\
I_{T_x}\dot{p} &= t_{MR_x} + d_H f_{TR} + \eta_{B_x} + ((I_{T_y} - I_{T_z})r + \varpi_{MR}) \\
I_{T_y}\dot{q} &= t_{MR_y} + t_{TR} + \eta_{B_y} + ((I_{T_z} - I_{T_x})r + \varpi_{MR})p \\
I_{T_z}\dot{r} &= t_{MR_z} + d_{TR}f_{TR} + \eta_{B_z} + (I_{T_x} - I_{T_y})pq \\
\dot{\phi} &= -(qs_\psi - pc_\psi)/c_\theta \\
\dot{\theta} &= ps_\psi + qc_\psi \\
\dot{\phi} &= r + s_\theta(qs_\psi - pc_\psi)/c_\theta
\end{aligned}
\tag{3.12}
$$

where $M_T = m_{MR} + m_F + \sum_{i=1}^{n} m_i$ is the total mass of the system, $\varpi_{MR} = 2I_{MR_x}\Omega_{MR}$ where I_{MR} is the main rotor's inertia matrix. Concerning the force, f, and torque, t, generation process, the aerodynamic contribution of the main rotor (MR) is given by f_{MR} and t_{MR} while the tail rotor (TR) produces f_{TR} and t_{TR}. The terms $I_{T_i}(i = x, y, z)$

are the values of the main diagonal of the inertia system matrix, $I_T \in \mathbb{R}^{3\times3}$ and depends on the angular positions of the arm joints γ_i. Thus, I_T can be calculated with respect to the center of mass of the global system as follows:

$$I_T = I_H + \sum_{i=1}^{n}(R_{\gamma_i}^T(I_{\gamma_i} + m_i(d_{Bi}^2\delta_{ij} - d_{Bi}d_{Bi}^T))R_{\gamma_i}) \tag{3.13}$$

where $d_{Bi} = \sum_{i=1}^{k}(\prod_{j=1}^{i} R_{\gamma_j})p_{Bi} \in \mathbb{R}^3 (i = 1...k)$ is the distance between the CoG of joint i and the manipulator base that is attached to the helicopter belly, $R_{\gamma_j} \in \mathbb{R}^{3\times3}$ is the rotation matrix of the joint γ_j, p_{Bi} is the position of the CoG of the joint i w.r.t. the axis of rotation joint and δ_{ij} is the Kronecker delta function. The moments of inertia of the helicopter and each arm's link are represented by I_H and I_{γ_i}, respectively.

Note that only the main moments of inertia are considered in the simplified model in equation 3.12, since the inertia cross moments, although they vary with the movement of the arm, are considered small. This assumption simplifies the equations greatly for controller derivation. The Modelica high-fidelity model includes the full dynamics and inertia characteristics of the helicopter and the arm, and the simulation experiments in the last subsection of this chapter will serve as validation of the assumption.

In equation 3.12, the term $\eta_B = t_B + \delta_B f_B \in \mathbb{R}^3$ collects all the torques due to the joints torques and the accelerations of the centre of gravity of the manipulator. Where δ_B is the position of the center of gravity (CoG) of a manipulator $\delta_B \in \mathbb{R}^3$ in frame B, it can be obtained from the CoG positions of the links using the kinematic model of the manipulator as follows,

$$\delta_B = \left\| \frac{\sum_{i=1}^{k} m_i d_{Bi}}{\sum_{i=1}^{k} m_i} \right\| \tag{3.14}$$

The justification for not including the dynamics of the manipulator arises from the fact that in practice, it is assumed that the control of the manipulator arm is only kinematically coupled. That is to say, the manipulator controller is decoupled from the helicopter controller and receives the position and velocities of the manipulator base.

3.2.2 Controller

The controller uses the feedback signals coming from the arm joint positions and velocities, which provide a good dynamic response when the manipulator moves. The dynamic model of the entire system, equation 3.12, can be rewritten in a matrix form as follows:

$$\begin{aligned} M_T\dot{V} &= F_{MR} + F_{TR} + F_{grav} \\ I_T\dot{\omega} + \omega \times (I_T\omega) &= \tau_{MR} + \tau_{TR} + \eta_B \end{aligned} \tag{3.15}$$

Then the four helicopter control inputs can be expressed as:

$$\begin{aligned} U_z &= f_{MR} \\ U_\omega &= \begin{bmatrix} t_{MR_x} \\ t_{MR_y} \\ f_{TR} \end{bmatrix} \end{aligned} \tag{3.16}$$

Following the control technique described in chapter 2, first of all, let consider the tracking error $e_\eta = \eta_d - \eta \in \mathbb{R}^3$ where η_d is the desired angular position. We need also to define the angular rate tracking error as e_ω

$$\begin{aligned} U_\omega &= I_T(P_\omega e_\eta + D_\omega e_\omega - \mu_\omega \lambda_\eta + \dot{\omega}_d) + \omega \times (I_T\omega) - \tau_\omega \\ U_p &= M_T(D^*(R_\eta e_3))^{-1}(P_p e_p + D_p e_v - \mu_p \lambda_p - \frac{(R_\eta^T e_3) f_{TR}}{M_T} - F_{grav}) \end{aligned} \tag{3.17}$$

3.2.3 Experiments

The possibility of testing control techniques for aerial vehicles with high-fidelity simulation models is very interesting, since it allows for controller testing and validation prior to experimentation. Modelica is an object-oriented language for modelling of large, complex and heterogeneous physical systems, which has the characteristics of multi-domain, non-causal and object-oriented (Elmqvist et al., 1999). Modelica now

has been widely used in many engineering fields (Pulecchi et al., 2010), (Bonvini and Leva, 2011) and also with aerial vehicles. (Chen et al., 2006),(Li et al., 2013) The modular structure of Modelica makes easy to model servomotor-driven multibody systems. In this section, first, we have developed a simulator in MATLAB/Simulink in which several tests have been done to validate the proposed control solution. Then, we use Modelica to model a helicopter-based aerial manipulator, which allows to capture the whole dynamic interactions between the arm and the aerial vehicle and provides a high-fidelity model to prove the control approach with several exhaustive tests.

Simulations with matlab

First, we present the results corresponding to the simulation test done in Matlab to validate the proposed control algorithm. For comparison purposes, the simulations performed with the proposed controller are presented jointly with simulations in the same conditions with a baseline PID controller. This PID helicopter controller has a cascaded structure with an inner angular rate control loop, a middle attitude angle control loop and an outer position control loop, which is commonly used in many UAVs.

Concerning the helicopter model, the geometric, mass and inertia parameters of the CB5000 autonomous helicopter have been used for the simulations (see Table 3.2.3). This is a small-size autonomous helicopter which is equipped with a RTK Differential GPS, an IMU, a magnetometer and a sonar altimeter. With this information, the simulation tool implements a very accurate model of the dynamics of the helicopter with the manipulator arm. Furthermore, noise characteristics of the sensors as well as uncertainties in their modelling parameters have also been accounted for. Angular sensors operate at a sampling frequency of 100 Hz and have a standard deviation of 1.2 degrees in attitude. Position estimation is supposed to be affected by a typical standard deviation of 0.04 m and its update frequency is fixed to 10 Hz. 1

The helicopter is also equipped with a 7-DoF robot manipulator Robai CYTON 1500. The parameters of this robotic arm that have been used for simulation are given in Table 3.1. Dimensions, moments of inertia and mass of each manipulator link were also estimated and included in the simulator. The first set of simulations has

Table 3.2: Helicopter CB5000 characteristics.

Parameter	Value
Helicopter mass	11 kg
Rotor diameter	1.9 m
Solidity factor	0.045
Ω_{MR}	1300 rpm
Rotor inertia	$I_x = I_y = 0.0846, I_z = 0.0846(kgm^2)$
Fuselage inertia	$I_x = 0.064, I_y = 0.244, I_z = 0.18(kgm^2)$

been carried out to verify the tracking properties of the proposed controllers when the arm is not moving. More precisely, the arm is extended downwards along the rotor vertical axis. In this scenario, the system should be able to track the desired reference trajectory at the same time that it is cancelling out the manipulator mass and inertia effects. The moments of inertia of the system are constant since the manipulator does not move in this first simulation experiment. The CoG of the entire system is located along the rotor vertical axis but further down that the CoG of the aerial vehicle due to the manipulator mass. For both the proposed controller and the cascade PID, the evolution of the position coordinates in the inertial frame is shown in Figure 3.23.

The reference trajectory appears as a dashed line. The 3D helicopter position is presented in Figure 3.24(left), whereas the magnitude of the position error is shown in Figure 3.24(right). While it is true that both controllers are able to track the reference trajectory, the proposed controller exhibits better performance and more advanced tracking capabilities than those of the cascade PID design. In the second set of simulations, the helicopter firstly follows a commanded trajectory to reach a desired position and then, from such stable hover condition, the system should be able to keep the desired position while the arm joints move at the same time.

Figure 3.25 shows the evolution of helicopter roll and pitch attitude angles during the second part of the simulation experiment, where the arm joints are allowed to move at certain instants ($t = 15$ s and $t = 25$ s) and the helicopter aims to achieve stable hovering. When the arm is centered and not moving, the roll and pitch angles present bounded oscillations of about $2 \sim 2.5$ degrees of amplitude. This effect is due to the sensor errors and the corresponding response given by the controller (this is common to both approaches, proposed controller and PID).

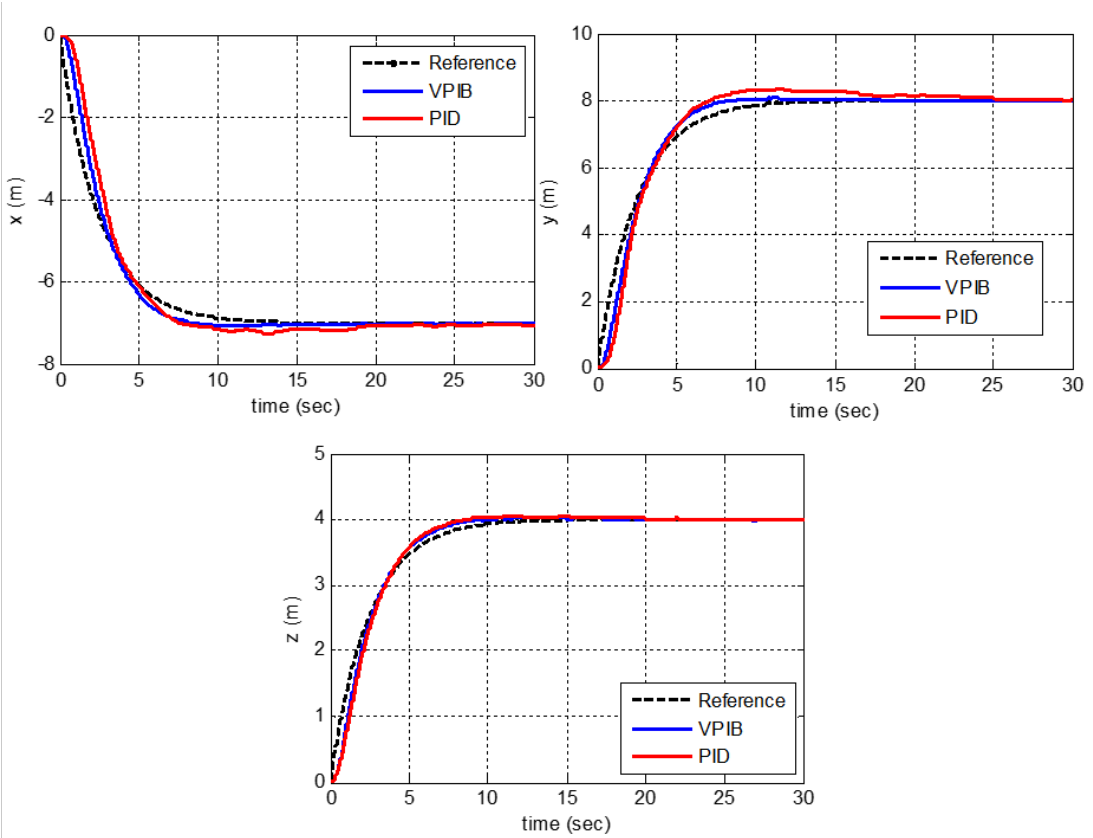

Figure 3.23: First simulation: reference trajectory (black dashed line), x, y, z position trajectories with proposed control (blue line) and PID (red line) controllers.

However, when the arm begins to move ($t = 15$ s and $t = 25$ s), the oscillations produced by the cascaded PID controller (red line) grow rapidly to $12 \sim 14$ degrees in pitch and $4 \sim 6$ degrees in roll angle. The pitch angle is the most influenced by the movement of the arm because the manipulator end effector is tracking a trajectory in the XZ plane in this experiment. In contrast to this undesired behaviour of the cascaded PID strategy, the figures show that apparently there is not any performance degradation with the proposed controller when the arm moves. Thus, the control approach is able to effectively counteract the movement of the arm to a large extent. Figure 3.26(a) illustrates the trajectory of the helicopter on the horizontal plane in world coordinates that correspond to the second set of simulations. The oscillations in roll and pitch attitude angles caused by the manipulator movement generate the

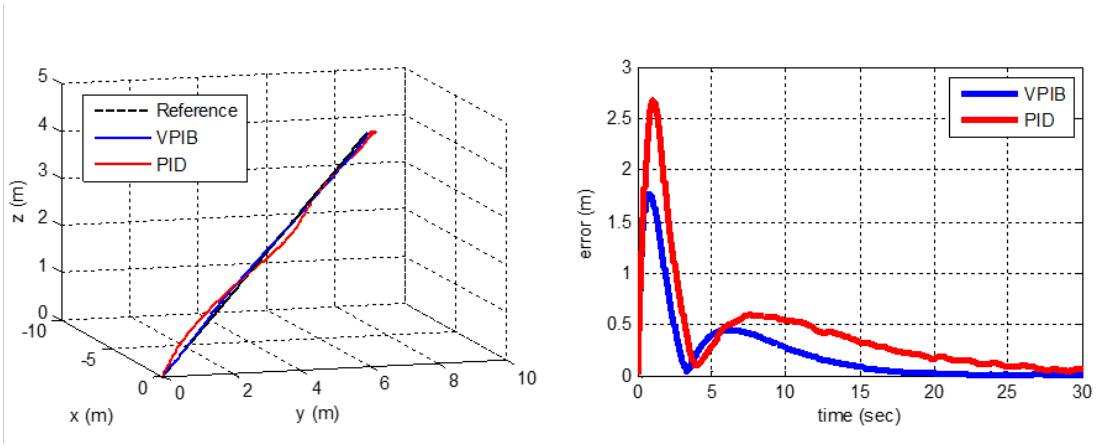

Figure 3.24: First simulation: reference trajectory (black dashed line), x, y, z position trajectories with proposed control (blue line) and PID (red line) controllers.

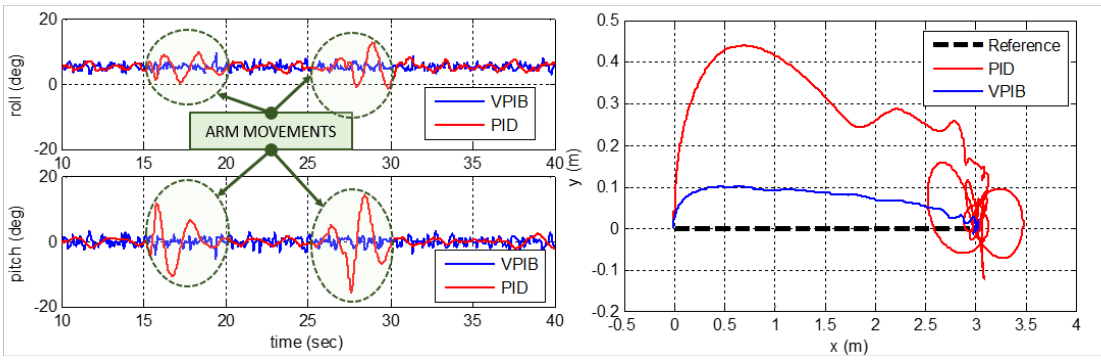

Figure 3.25: Second simulation: roll and pitch attitude angles of the control approach (blue line) and PID (red line).

position errors observed in Figure 3.26(a), which are significantly larger with the cascade PID controller.

In the third set of simulation experiments, the helicopter is tracking a desired trajectory while the manipulator moves at the same time. Figure 3.26(b) shows the tracking trajectory in the XY-plane for both approaches, cascade PID (red line) and the control approach (blue line). On the other hand, position errors for both controllers are represented in the upper plot of Figure 3.27. They can be seen in relation with the movements of the manipulator joints that are shown in the lower part of the same figure.

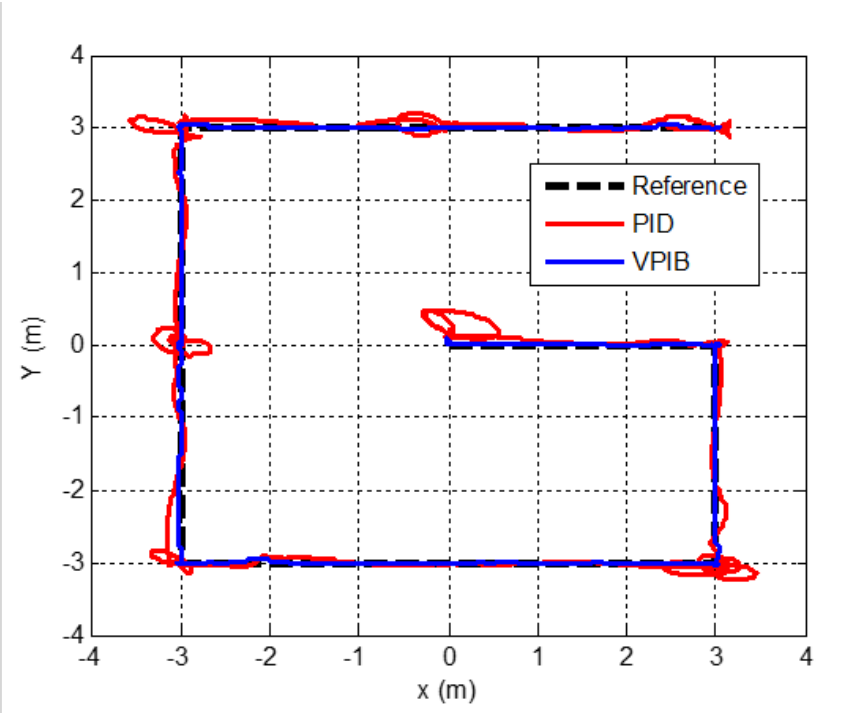

Figure 3.26: Second simulation and third simulations: reference trajectory (black dashed line), XY position trajectory with control approach (blue line) and PID (red line).

Validation with Modelica

This section presents the results of the proposed control approach tested with a high-fidelity model of the aerial manipulator. A detailed multibody model of the helicopter with the manipulator arm has been developed using Modelica, which captures all the couplings and interactions between the helicopter body, the main rotor and the arm links and other nonlinear effects as friction in the arm joints. This provides a high-fidelity model for validation experiments. Both the proposed controller and cascaded PID controllers have been tested with this model. As was the case in simulations of the previous section, the goal in these experiments is that the system be able to keep the desired position while the arm joints move at the same time, rejecting as much as possible the perturbations in roll and pitch. Several simulation experiments have been performed. Figure 3.28 shows roll and pitch attitude angles with both cascade

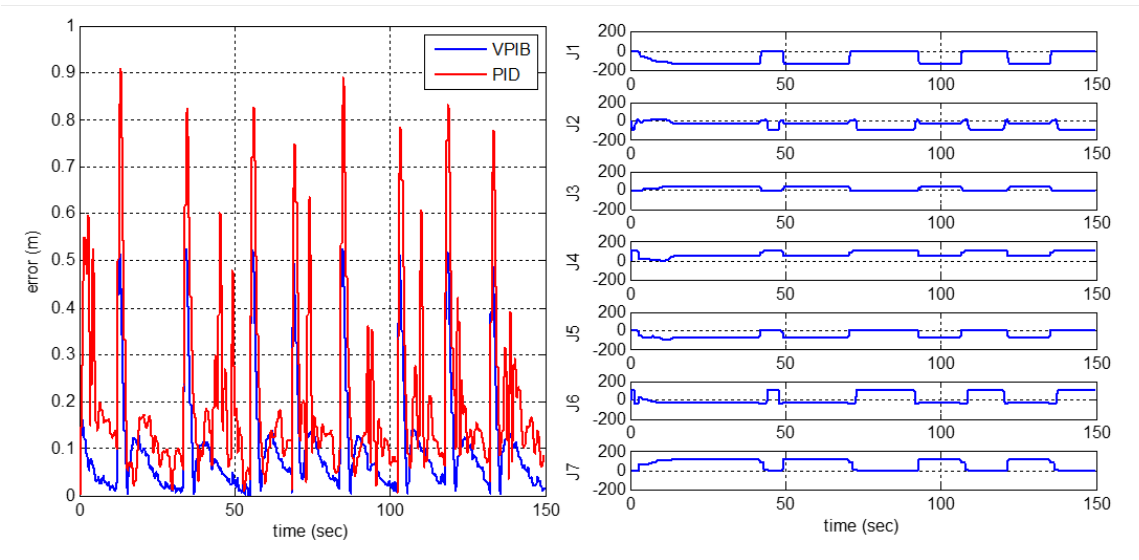

Figure 3.27: Third simulation: reference trajectory (black dashed line), XY position trajectory of proposed controller (blue line) and PID (red line).

PID and proposed controllers on one of the simulations. As with the simulations in the previous section, when the arm is moving (between $t = 15$ and $t = 20$, and $t = 25$ and $t = 30$), the pitch angle is the most influenced. Furthermore, when the arm is not moving both the cascaded PID and the proposed controllers have similar performance. Nevertheless, when the arm is moving the stabilization of the helicopter was faster with the proposed controller. In this case, the oscillations produced by the cascaded PID controller (red line) were of $10 \sim 14$ degrees in pitch during the first movement and $5 \sim 10$ degrees during the second movement. However, the oscillations produced with the proposed controller (blue line) were of 5 degrees in pitch during the first and second movements.

In general, the oscillations of the attitude angles when the arm is moving are larger in the experiments with this validation model than in the simulations of the previous section, what could be expected since the model is more detailed and includes couplings and nonlinear effects not present in the other model. They also show a stronger coupling of the roll and pitch angles. However, the presented controller

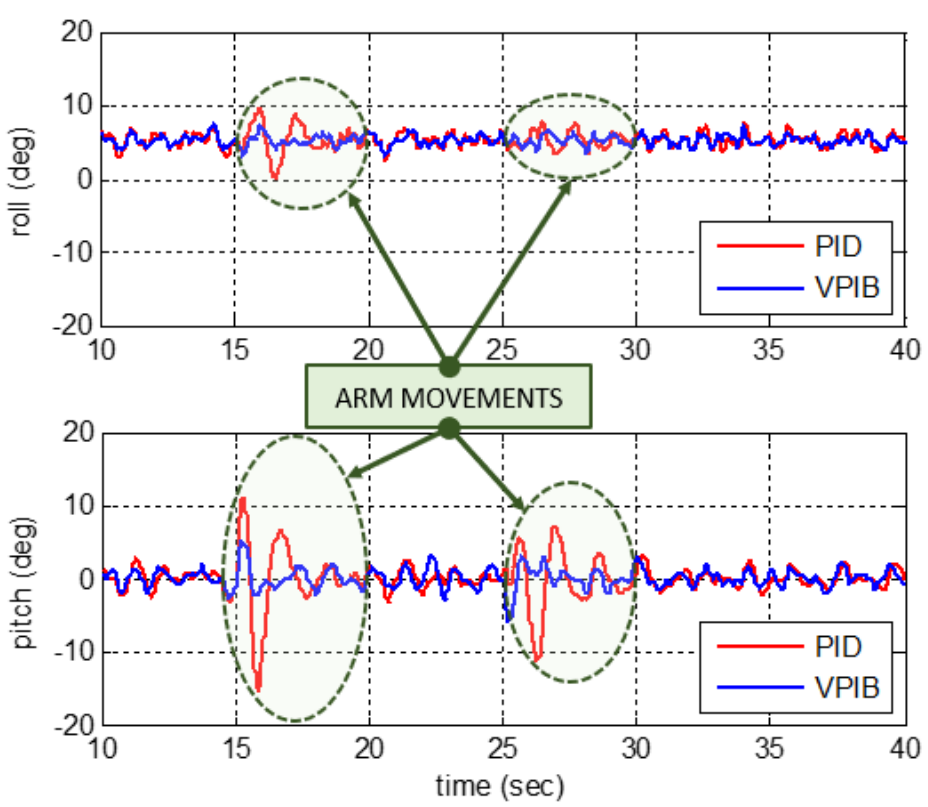

Figure 3.28: Simulation experiments with the Modelica validation model.

consistently performs better than the cascaded PID controller with much reduced oscillations, greatly easing aerial manipulation operations.

When comparing the proposed controller strategy with the classical cascaded PID approach, the analysis of the different simulations shown in this section allows to conclude that performance of the controller proposed as well as its associated responsiveness against disturbances caused by manipulator movements, are clearly better than those exhibited by the cascaded PID design Furthermore, although the proposed control is a model-based controller, this approach has demonstrated a significant robustness attributes against parametric and modelling uncertainties in the simulations.

Chapter 4

Applications (II). Aerial manipulators for structure inspection

Nowadays, the structural assessment of bridges involves the use of a lot of equipment, including heavy machinery like lifters, scaffolders and cranes among others. Typically, an inspection of a civil structure is divided into two parts. One first part of this assessment is a visual inspection to detect cracks, corrosion, leaching and other defects. A second part involves other tasks that require direct contact of a sensor with the structure, i.e. using ultrasound testing sensors to measure the crack depth or measuring beam deflection through a reflector prism and a topographic station.

New applications are continuously emerging with the continuing development of aerial platforms. Standard multirotors with cameras have been used for an initial visual inspection of difficult to access areas of civil infrastructures and helping to inspectors with the first part of the assessment. However, when cracks or other damages are detected in the images or to measure a beam deflection, the inspection has to follow with experienced human inspectors in need of hands-on-access and forcing operators to work in high altitude in dangerous conditions.

The use of aerial manipulators provide an excellent solution for conducting the inspection by contact of bridge elements without human intervention and carrying

Figure 4.1: Structures inspectors working at high altitude.

out tasks such as holding an ultrasonic sensor to evaluate a crack or positioning a topographic prism to measure a beam deflection. This chapter is focusing on this second part of the assessment of civil structures, i.e. the inspection by contact.

In this chapter, we present three aerial manipulator applications related to the structural inspection. The first application is a multirotor equipped with a 3-DoF arm whose goal is to use the arm to hold an ultrasound sensor in contact with the bridge while the multirotor is hovering. In the second application the manipulator is a lightweight compliant arm that could be used both to hold an ultrasonic sensor and to hold a topographic prism to measure girder deflection. The last application is focusing on the controller of an aerial platform specifically designed to optimize the task of taking deflection measurements of bridge girders by holding in contact a topographic prism. This application is the most advanced in AEROBI-project, carrying out even autonomous mission to measure girder deflections of a bridge.

The first application presented was developed in the ARCAS project. Nevertheless, it was one of the first aerial manipulator prototypes used for structure inspection by contact, and helped in the first months of the AEROBI project. The H2020 AEROBI project started in 2015, and was aimed at helping in the development and validation of innovative and intelligent aerial platform prototypes for the in-depth structural inspection of reinforced concrete bridges. The second and third applications were developed in the framework of the AEROBI project.

Figure 4.2: Examples of visual bridge inspections using UAVs.

4.1 Application 1 - Multirotor with multi-link arm for structure inspection

This application deals with the works published in (Jimenez-Cano et al., 2015) about the use of aerial manipulator as a solution for conducting the inspection by contact of bridge elements without human intervention. The objective was to implement an aerial manipulator system able to hold a sensor (i.e, ultrasonic sensor) in contact with a bridge while the aerial platform is hovering. Furthermore, since in many cases the bridge elements have to be inspected from below (i.e. the aerial robot should fly below the bridge, and the surfaces that it has to inspect are located above the robot), a new aerial manipulator configuration is proposed in which the arm is attached on top of the multirotor body above the rotors, and not on the belly below the rotors as is the case for all the published works.

Figure 4.3: AMIS aerial manipulator for structure and bridge inspection, developed by the GRVC at University of Seville.

Following we present a system description with the main details of the prototype. Next, the dynamic system is introduced and a control scheme proposed. Finally, we show the results of the tests simulation and flying experiments that were done to validate the proposed solution.

4.1.1 System Description

For this application the AMIS (Aerial Manipulator for bridge inspection of Structure) prototype was developed by the GRVC at University of Seville. The AMIS aerial platform is a multirotor with eight rotors located at the ends of a four-arm planar structure, with two rotors positioned coaxially at the end of each arm (octoquad configuration). The multirotor has an arm manipulator attached to the upper part. The arm has three degrees of freedom and the length of the links are 400mm, 350mm and 50mm, respectively. Dynamixel servos have been used for the arm's joints. The total weight of the manipulator is 1.3 kg, and the maximum reach is about 860 mm including the sensor head. The total weight of the multirotor with the arm is 8.6 kg. The autopilot used in the AMIS prototype is the same that in AMUSE (see chapter 3, section 1). AMIS incorporates a camera on-board for visual inspection, an altimeter

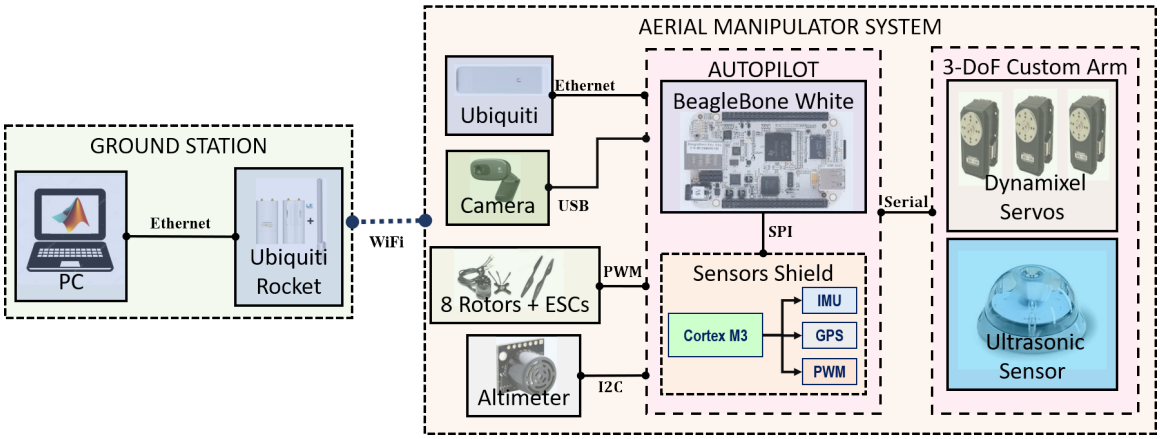

Figure 4.4: AMIS system description

and an ultrasonic sensor located at the arm end-effector. This sensor is used to the inspections by contact and, in the first experiments show in the following subsections, it will be replaced by a mock-up sensor.

4.1.2 Modelling

In this case, we use Lagrange-Euler method to derive the system dynamics. As we describe in the above subsection, the prototype developed was a multirotor in octoquad configuration and equipped with a 3-DoF custom robot manipulator. Therefore, we have a system composed of four bodies ($N_B = 4$) and 9-DoF ($N = 9$). Then, the generalized coordinates are defined as

$$\varphi = [p\, \eta\, \gamma]^\top \in \mathbb{R}^9 \tag{4.1}$$

Following the Lagrange-Euler method describes in chapter 3, we obtain the equations of motion for the system given by 2.41. In which the gravity force vector $G(\varphi)$ can be calculated as

$$G(\varphi) = [G_p\, G_\eta\, G_\gamma\,]^\top \tag{4.2}$$

where $G_k \in \mathbb{R}^3$ are the terms of the gravitational force vector for the position of the multirotor, p, its orientation, η and each joint of the manipulator, γ, and can be

calculated as

$$G_p = -g \begin{bmatrix} 0 \\ 0 \\ \sum_1^{N_B} m_i \end{bmatrix} \qquad G_\eta = -g \begin{bmatrix} \frac{\partial p_z}{\partial \phi} \sum_1^{N_B} m_i \\ \frac{\partial p_z}{\partial \theta} \sum_1^{N_B} m_i \\ \frac{\partial p_z}{\partial \psi} \sum_1^{N_B} m_i \end{bmatrix} \qquad G_\gamma = -g \begin{bmatrix} \frac{\partial p_{z_{\gamma_1}}}{\partial \gamma_1}(m_2 + m_3 + m_4) \\ \frac{\partial p_{z_{\gamma_2}}}{\partial \gamma_2}(m_3 + m_4) \\ \frac{\partial p_{z_{\gamma_3}}}{\partial \gamma_3} m_4 \end{bmatrix} \tag{4.3}$$

The equations of motion 2.41 can be rewritten without loss of generality as

$$\begin{bmatrix} M_p & M_{p\eta} & M_{p\gamma} \\ M_{p\eta}^\top & M_\eta & M_{\eta\gamma} \\ M_{p\gamma}^\top & M_{\eta\gamma}^\top & M_{p\gamma} \end{bmatrix} \begin{bmatrix} \ddot{p} \\ \ddot{\eta} \\ \ddot{\gamma} \end{bmatrix} + \begin{bmatrix} C_p \\ C_\eta \\ C_\gamma \end{bmatrix} + \begin{bmatrix} G_p \\ G_\eta \\ G_\gamma \end{bmatrix} = \begin{bmatrix} F_p \\ \tau_\eta \\ \tau_\gamma \end{bmatrix} + \begin{bmatrix} S_a^\top \\ J^\top \end{bmatrix} F_{ext} \tag{4.4}$$

where $S_a^\top$ is a transformation matrix that relates the external forces/torques acting on the robotic arm and the aerial vehicle.

4.1.3 Controller

The control scheme implemented for this application uses a controller for the multirotor and another one for the manipulator arm. Following the control scheme presented in chapter 2, both have access to the full aerial manipulator state. The multirotor controller is responsible for stabilizing attitude and global position of the aerial vehicle, taking into account and compensating the movements of the arm and the contact forces with the environment. The manipulator controller takes care of controlling arm joints angles and velocities, and the generalized forces Γ that are generated by the aerial manipulator in the operational space, considering the movement and dynamics of the multirotor.

Multirotor controller

The aerial platform is an octoquad, the eight rotors have been positioned in four coaxial pairs of rotors. It means that the multirotor behavior is like a quadrotor. Then, the control inputs are defined as

$$U = \begin{bmatrix} U_z \\ U_\phi \\ U_\theta \\ U_\psi \end{bmatrix} = \begin{bmatrix} c_T & c_T & c_T & c_T & c_T & c_T & c_T & c_T \\ -c_T & -c_T & 0 & 0 & c_T & c_T & 0 & 0 \\ 0 & 0 & c_T & c_T & 0 & 0 & -c_T & -c_T \\ c_D & -c_D & c_D & -c_D & c_D & -c_D & c_D & -c_D \end{bmatrix} \begin{bmatrix} \Omega_{1,1}^2 \\ \Omega_{1,2}^2 \\ \Omega_{2,1}^2 \\ \Omega_{2,2}^2 \\ \Omega_{3,1}^2 \\ \Omega_{3,2}^2 \\ \Omega_{4,1}^2 \\ \Omega_{4,2}^2 \end{bmatrix} \tag{4.5}$$

where $\Omega_{i,j}^2$ is the angular velocity of the j-th rotor positioned in the i-th arm. Following the proceeding defined in the chapter 2 controller section, for the dynamic model presented the control inputs are given by

$$\begin{aligned} U_z &= \frac{m_T}{c_\phi c_\theta}[P_z e_z + I_z \chi_z + D_z e_{\dot{z}} + \ddot{z}_d] - \widetilde{F}_{E_z} \\ U_\eta &= D^{\triangle}(M_\eta)[P_\eta e_\eta + I_\eta \chi_\eta + D_\eta e_{\dot{\eta}} + \ddot{\eta}_d] + \sum T_\eta \end{aligned} \tag{4.6}$$

where P_z, I_z and D_z are positive constant gains and $\widetilde{F}_{E_i}(i = x, y, z)$ are the components of the external force estimation vector which is used to describe the dynamics effects over the multirotor due to the interaction between the end-effector manipulator and the environment. The positive diagonal matrix P_η, I_η and D_η are also used as controller gains and the vector $\sum T_\eta$ is given by

$$\sum T_\eta = C_\eta + G_\eta + \widetilde{N}\ddot{\gamma} - \widetilde{\tau}_c \tag{4.7}$$

where $\widetilde{N}\ddot{\gamma}$ introduces the estimation of the dynamics coupling due to the manipulator movements and $\widetilde{\tau}_c$ the estimation of the torque induced by the contact forces, F_{ext}. The dynamics of the interaction between the end-effector and the environment had been modelled using a Hunt-Crossley model (Diolaiti et al., 2005) and a spring model

had been used for modelling the contact. The environment was assumed to have a constant stiffness. Then each contact n is given by

$$f_c^n = k_n \dot{x}_n \tag{4.8}$$

Herein f_c^n is the n-th contact force and $\dot{x}_n$ is the instantaneous velocity in the contact normal direction. In this case, these positions are defined in the end-effector frame, hence the external force vector, $\widetilde{F}_{ext}$ is defined as

$$\widetilde{F}_{ext} = S_a^\top f_c^n(x) \in \mathbb{R}^6 \tag{4.9}$$

The measurements of the contact forces can be carried out through a force sensor at the end-effector. The position controller must be capable to keep the desired (x, y, z) position while the manipulator performs the contact task with the underside of the bridge.

End-Effector controller

The manipulator arm is attached to the multirotor body, and hence the multirotor needs to move to a position in which the task operational space is within the arm workspace. The multirotor is commanded to hover at this point with the controller developed above, while the arm is performing the inspection (then $\dot{p} \sim 0$ and $(\phi, \theta) \sim 0$) and the arm controller considers that these terms are small. Another consideration is that $X_{Ed} \in \mathfrak{D}_{X_E}$ where X_{Ed} and $\mathfrak{D}_{X_E}$ represent the desired effector position and the domain of the operational space, respectively. $\mathfrak{D}_{X_E}$ can be calculated as:

$$\mathfrak{D}_{X_E} = G(\prod_{i=1}^{k}[\gamma_i^-], \gamma_i^+) \tag{4.10}$$

where γ_i^- and γ_i^+ are the minimal and maximal bounds of the i-th joint coordinate, respectively. An effective technique for dealing with these highly nonlinear and coupled systems is the nonlinear dynamic decoupling in operational space (Hara et al., 2012)

which can be derived using the relationship between the generalized forces 2.60 as:

$$\tau_M = J_E^T M_M^* \Gamma_E^* + \widetilde{C}_M + \widetilde{G}_M^* - J^T F_E^* + M_{QM}^T \begin{bmatrix} \ddot{p} \\ \ddot{\eta} \end{bmatrix} \tag{4.11}$$

with

$$\begin{aligned} \Gamma_E^* &= \mathbb{I}_{EE} \ddot{X}_{Ed} + k_p (X_{Ed} - X_E) + k_v (\dot{X}_{Ed} - \dot{X}_E) \\ F_E^* &= f_{Ed} + k_f (f_{Ed} - f_c) \end{aligned} \tag{4.12}$$

where $\widetilde{C}_M = C_M - J_E^T M_M^* h(p, \dot{p})$ is the estimated vector of the Coriolis and centrifugal forces into joint space of the end-effector and $\widetilde{G}_M$ is estimated gravity forces vector. The term $\mathbb{I}$ represents a unity matrix. k_p, k_v and k_f are gain matrices for position, velocity and force respectively. The contact force measurement done by the force sensor is denoted by f_c and the desired contact force is expressed by f_{Ed}. In the real system, oscillations in the multirotor axis generate disturbances in the contact force measured by the sensor which will be compensated by the control action, F_E^*, in 4.12 and the feedback force, $F_{ext}^{p,\gamma}$ in 2.53.

4.1.4 Simulations and Outdoor Experiments

This section presents the several tests that have been done using the full mathematical model of the aerial manipulator. In simulation tests the geometric, mass and inertia parameters used have been obtained from the prototype showed in Figure 4.3, using a 5-DoF manipulator. Furthermore, it is assumed that the multirotor is equipped with a positioning system, an Inertial Measurement Unit (IMU), a magnetometer and a sonar altimeter. Noise characteristics of the sensors as well as uncertainties in their modelling parameters have also been accounted for. The IMU operates at a sampling frequency of 100 Hz and it has a standard deviation of 1.2 degrees in attitude. Position estimation is supposed to be affected by a typical standard deviation of 0.04 m and its update frequency is fixed to 10 Hz.

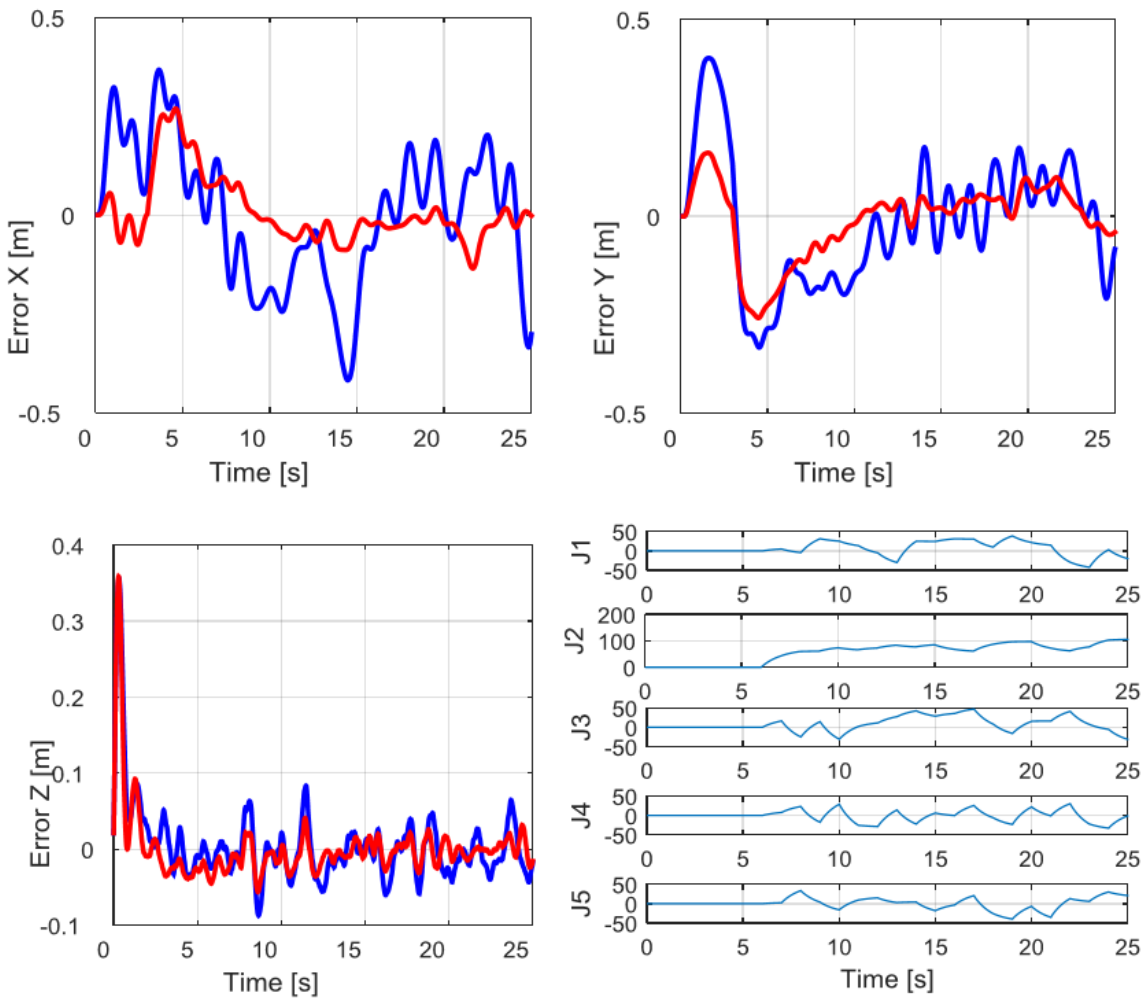

Figure 4.5: Simulation of the aerial manipulator flying forward and moving the arm. X, Y, Z position errors, PID (BLUE) and control proposed (RED). Arm joints movements (bottom right).

The first set of simulations that is presented in this subsection analyzes the behavior of the aerial manipulator when it is flying forward to a desired position with the center of gravity off-center, and then the arm moves constantly changing its configuration (and the position of the CoG), which is one of the more demanding cases. Figure 4.5 shows the X,Y,Z position errors in one of these simulations, when the aerial robot is flying toward the desired position (2,-2, 2), with the CoG off-center and there the manipulator carries out several movements, using the attitude and position controllers

above presented. For comparison purposes, simulations have been done also with a standard PID multirotor controller, which is not able to compensate for the arm movement, as the backstepping controller does to a large extent.

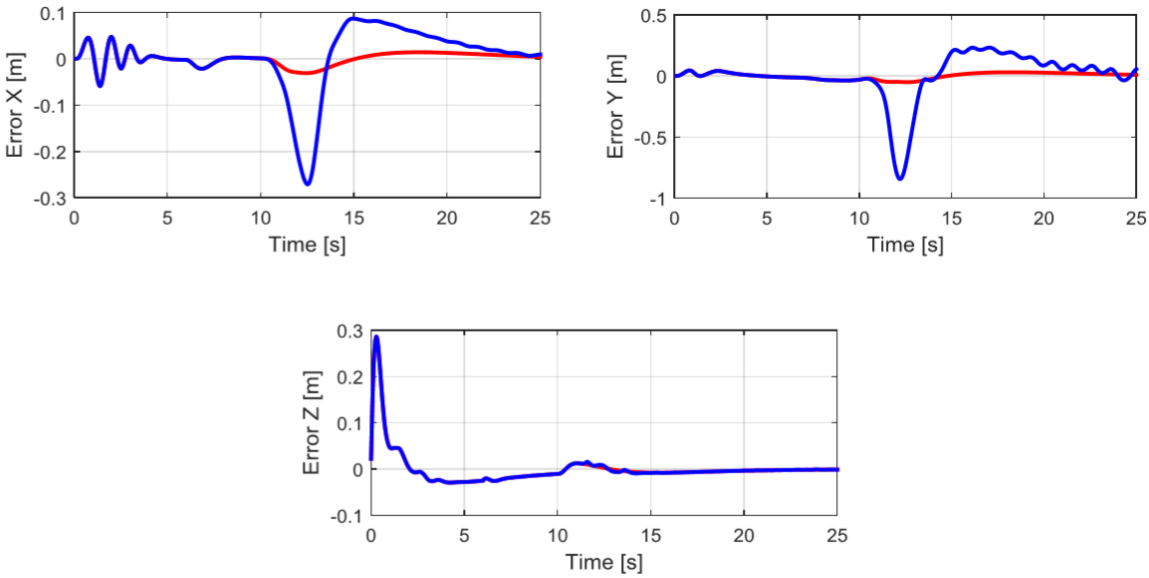

Figure 4.6: Simulation of the aerial manipulator hovering and touching the bridge with the arm. X,Y,Z position errors, VPIB with contact force estimator (RED) and control proposed without contact force estimator (BLUE).

A second set of experiments studies the behavior when the aerial robot is inspecting a structure such as a bridge, touching it with the ultrasound sensor head located at the end effector of the arm, and applying a contact force so that the sensor stays in touch enough time to take measurements. Figure 4.6 shows the position errors using the VPIB controller with contact force estimator and without using it, which is affected by the contact forces of the arm with the bridge (beginning at t = 10 s), as can be seen in the figure.

In the following,we present the experiments done to test the dynamic behavior of the AMIS prototype with the developed attitude controller when it is approaching the inspection point at the bridge, and then when the AMIS arm is touching the structure with the sensor head to take measurements. For these experiments a dummy sensor was used and no ultrasonic measurements were done (see Figure 4.7).

Figure 4.7: Sequence of bridge inspection experiment.

Another very interesting point that wanted to try in the experiments was whether the stability of the aerial vehicle was affected by the contact forces in case an extra force was deliberately applied by the arm at the sensor head, so that the contact with the bridge surface can be constantly maintained enough time to take the measurements with the sensor head. From the performed experiments, it can be concluded that this extra force did not affect the aerial manipulator stability. In fact, it was even the opposite, the extra force decreased the multirotor pitch and roll oscillations, as can be seen in Figure 4.8.

The figure shows the total thrust generated by the AMIS rotors and the multirotor pitch attitude angle. It can also be seen in the figure that the total thrust can be a good estimator of the contact forces, since the multirotor is in hover when performing these operations. Unmanned Aerial Vehicles are evolving to include not only systems with sensing capabilities but also with the possibility to act on the environment, and particularly with manipulation capabilities. This work presented a new configuration for an aerial manipulator in which the arm is attached to the top of the multirotor. This setup is well suited for infrastructure and bridge inspection flying below the elements that are being inspected, even by contacting the bridge surface with an ultrasonic sensor located at the end effector of the arm. The derivation of the aerial manipulator dynamic model and suitable controller, which has been tested in simulation and in flying experiments. These tests suggest that the additional forces applied by the arm

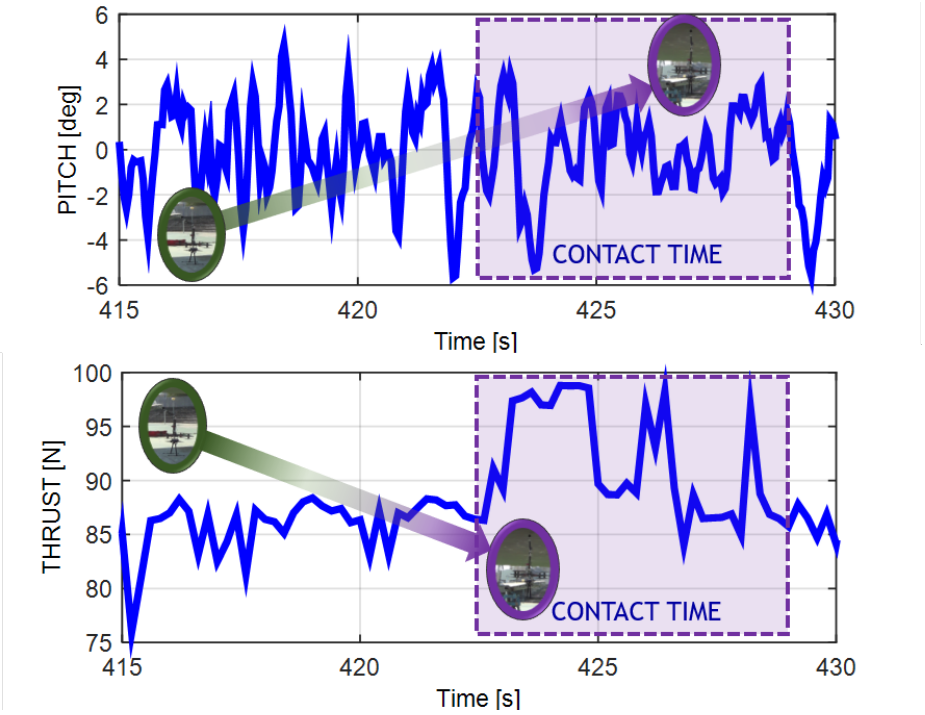

Figure 4.8: Bridge inspection experiment. Total thrust and pitch angle.

to the bridge surface to maintain contact are even beneficial for multirotor stability, decreasing pitch and roll oscillations.

4.2 Application 2 AEROBI - Multirotor with multi-link compliant arm for structure inspection

This application emerges from the experience obtained in the above case. For the use of some ultrasonic sensors or to perform measurements with a topographic prism, it is desirable to control the force exerted by the aerial manipulator over the contact surface. A solution could be the use of a force/torque sensor but these sensors are expensive and, in many cases, too heavies. For this reason, we decide to design a robotic arm with compliant joints. An actuator is compliant if it is able to adapt to the force generated when it interacts with the environment. This capability implies that the manipulator no only can be protected against damages due to impacts, but

it also can estimate these forces and torques measuring the deflection of the elastic element included therein (springs or elastomers). For this reason, in this application, we decide to develop a new lightweight compliant arm. To achieve it, an innovative compliant actuator has been designed. Its technical details are described in the next section.

The integration between an aerial manipulator and a topographic station is one of the aims of this application to carry out structures inspection tasks. To achieve it, the topographic station used in this work is a robotic Total Station (TS) developed by Leica (Leica, 2019). The Leica Total Station is a device that may be used, among others, for measuring distances with laser technology. It can measure the distance to any surface or to a reflector prism. This kind of devices are commonly used in topography and building construction and with the angles of itself can get the position of the objective points in local axis which are defined by the user. When the total station is working with a topographic prism, this reflects the laser in the same direction that is received to generate the measure of its position improving the accuracy. In addition, it is able to track the prism in case of it is moving. Another feature is the possibility of generating point clouds thanks to its laser technology. These point clouds can be used to create accurate 3D maps of a structures (Delgado et al., 2017).

Furthermore, in this section, we present a full aerial manipulator system including a topographic robotic total station to perform measurements of the position of a prism allocated as end-effector in the robot manipulator arm developed. A central feature in the system presented is that the measurements done by the Total station are employed to obtain the deflection of a bridge girder and, moreover, to estimate the position of the aerial manipulator.

Next, we provide more details about the hardware used in the implementation of the full aerial manipulator system. In addition, we derive the dynamic model and we propose a controller for the aerial manipulator. Finally, in order to validate the proposed controller, we present the experiments results done.

Figure 4.9: Prototype done a contact with the ceiling bridge.

4.2.1 System Description

In a structure inspection, the main tasks are done through direct contact between the bridge surface and suitable tools. For example, to measure the deflection of a girder over time, a topographic station measures the position of a prism while it is in contact with the surface of the girder. Another example is an ultrasonic sensor that is used in contact with a crack or void to measure its dimensions. Another task is monitoring the deterioration of the elastomeric bearings between the rafters and the pillars that usually have difficult access. Therefore a multi-link compliant robotic arm can be an useful tool for structural inspection. As we already mentioned, in this section we present the prototype developed by the GRVC at University of Seville consisting of a multirotor equipped with a custom compliant robotic arm. First, we present details in the multirotor configuration chosen for this application. Next, we focus on the custom compliant arm manipulator and the innovative compliant actuator developed. The picture of the aerial manipulator system designed can be seen in Figure 4.10.

Figure 4.10: (Right)3D Figure of the multirotor and robotic arm designed.(Left) Picture showing the custom compliant arm developed

Multirotor configuration proposed

A novel configuration of an aerial vehicle has been proposed for this work. This multirotor is an octorotor system with two layers, where the alternate rotors are kept at different planes with a vertical distance between each one, enabling propellers to overlap as shown in Figure 4.11. Thanks to this configuration, total size area of the octorotor can be minimized without loss of flight time and payload capability (Nandakumar et al., 2018), and it allows the system to access and navigates through smaller spaces like, for example, between beams or columns. Furthermore, in the bottom layer each rotor has been placed with an angle over the layer horizontal plane.

Thus, the aerial vehicle is fully actuated, since it is possible to generate horizontal forces without tilting the platform. This is beneficial for aerial manipulation tasks because it allows the manipulator to work like in a fixed platform, reducing the disturbances due to the attitude oscillations in the aerial platform.

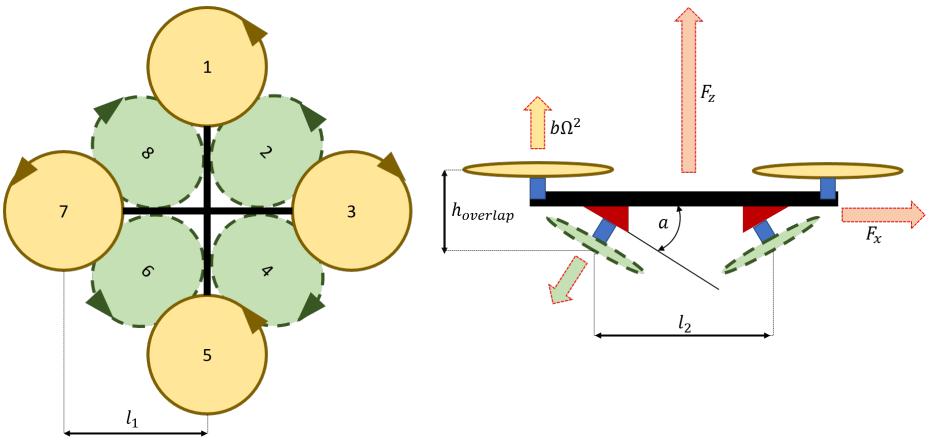

Figure 4.11: Scheme of multirotor layers.

Lightweight Compliant Arm design

Most commercial robots manipulators have been designed without taking into account the weight and the mass distribution in each of its links, therefore they have not made suitable to use in aerial platforms. The center of gravity of an aerial manipulation system is modifying its position continuously while the robotic arm is performing a task. This variation of the position of the center of mass depends on the mass distribution of the manipulator. Thanks to this effect, these systems present complex coupling dynamics. Therefore, the stabilization and the design of control strategies are hard problems for these systems. An aid to solve these problems could be the design of lightweight arms (Suarez et al., 2015). An optimization in the mass distribution of the robotic manipulator would reduce the influence over the aerial manipulator. Furthermore, the contact forces generated by the interaction between the robotic arm and the environment also affect the platform stability. Therefore, the design of a robotic manipulator with compliant joints can present a desirable solution against the problems caused by shocks or impacts. In ascending order, the first specification design should be a low weight and the second, a minimization of the influence of the inertia term of each link over the UAV. Construction materials such as aluminium, carbon fiber or 3D-printers philaments (PLA, ABS, etc) should be considered in the design due to their low mass density. The construction of aluminium or carbon fiber pieces for

the implementation of a robotic arm require the use of expensive precision equipment. Thus, we opt to make our robotic arm with 3-D printers materials. The popularity of 3D-printers has raised in few years due to it has demonstrated to be useful for rapid-prototyping in robotics. Furthermore, in case of damage, the reparations of our prototype becomes easier using 3D-printers pieces. The most used materials are PLA (Polylactic Acid) or ABS (Acrylonitrile Butadiene Styrene). For these reasons, it has been the material chosen to make our prototype.

Herkulex smart servos have been employed as actuators for the construction of our prototype. Thanks to these servos, the mechanical design can be simplified without a loss of accuracy in the position control and with high torque to weight ratio. A disadvantage is that they do not present an option of torque control. The robotic arm must have the capability to interact with the environment and consequently, it should support a strong exposure to impacts and overloads. For this reason, a Passive Compliance Mechanism (PCM) has been designed. The PCM aims to absorb the impact energy and protect the actuators. Furthermore, it has been designed like a torque sensor and allocating one on each actuator it allows to measure the forces acting on the arm and the contact forces applied by it. In Figure 4.12, a scheme of PCM is shown.

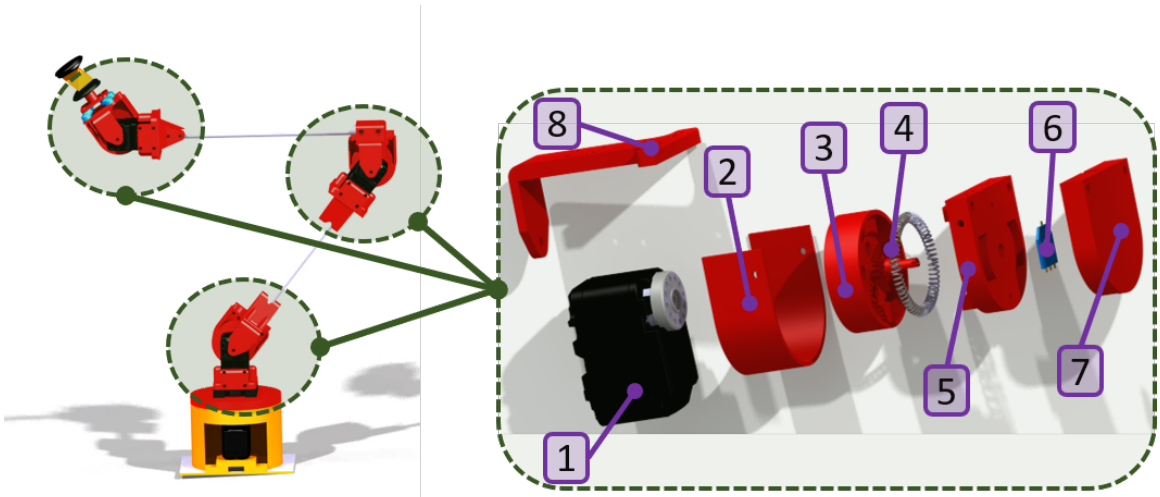

Figure 4.12: (Right)Scheme of the passive compliance mechanism (PCM).(Left)3D CATIA model of the 4-DoF robotic arm developed.

As Figure 4.12(Right) shows, four symmetric springs (part number 4) are placed on piece 3. These springs are used as elastic material and measurement the deflection it is possible to estimate the torque acting on the servo. This piece 3 is attached to the actuator (part number 1). When a force is applied to the joint, the piece 5 twists through the servo's rotation axis. The force is transmitted to the springs that will be compressed. This compression generates a difference between the angle of the joint and the servo's angle position. The difference is measured by the potentiometer (part number 6). To add strength to the mechanism works both pieces 2 as 7. The piece 8 is the linkage with the next joint. Thanks to the potentiometers' measurements, both torque and external force can be estimated and thus a force controller could be designed. Using the complaint mechanism previously described, a four degrees of freedom compliant arm has been developed. The Herkulex servos model selected have been the model DSR-0201. The manipulator is formed by a shoulder yaw and pitch joints at the base, followed by an elbow and a wrist pitch joints. The center of mass of each link is placed within its rotation axis, thus the kinematics are simplified. The total weight of the robotic arm is 0.4 kg. and its reach is 0.5 meters. The compliant arm has an excellent relation between the maximum reach and weight. All joints have a compliant mechanism with a max. deflection of 30 degrees. A 3D CATIA model of the 4-DoF compliant arm developed is shown in Figure 4.12(Left).

Hardware Scheme

For this prototype we use a hardware architecture based on the CATEC autopilot introduced in the above chapter, section 1. In this case, the BeagleBone White is communicated by ethernet with a Beaglebone Black. This device manages the signals of the sensors needed by the system (external magnetometer, altimeter SF11/C, PX4Flow, etc) and input/outputs of each servo actuator of the robotic arm as well as the signals of each potentiometer located in each joint. The hardware scheme can be seen in Figure 4.13.

In the same way that in the AMUSE system, the controllers are developed using MATLAB/Simulink and run in the BeagleBone White. The BeagleBone Black is used to expand the inputs/outputs in the above system. For the positioning system, we use

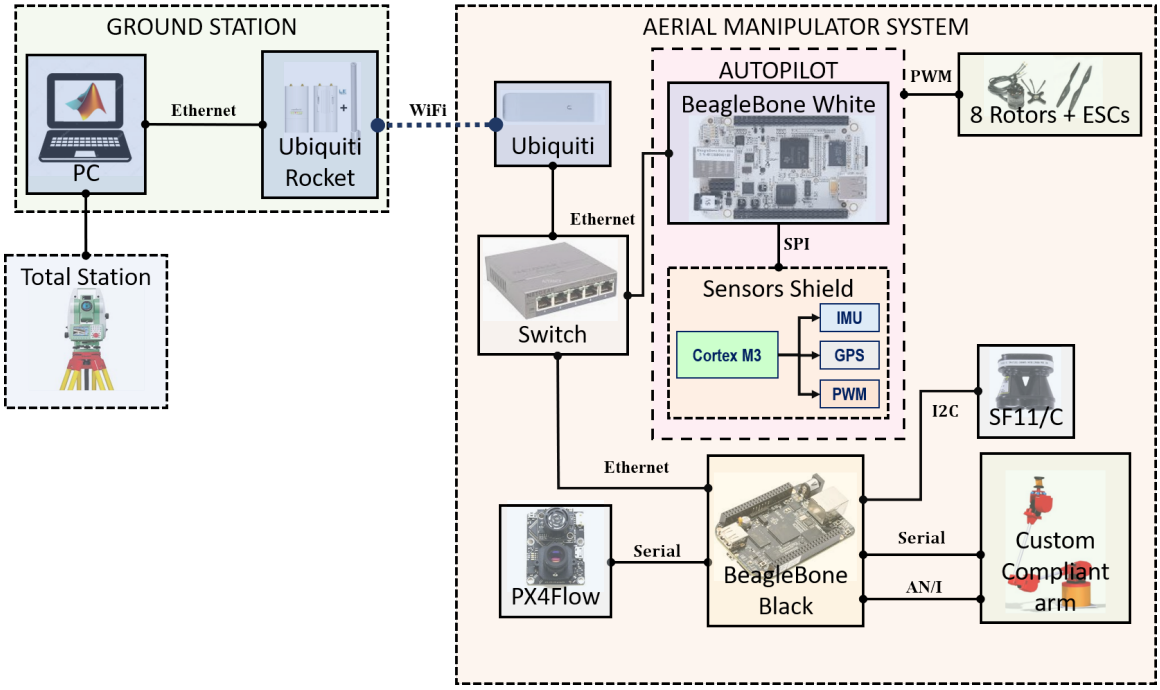

Figure 4.13: Hardware architecture of the system.

a laser altimeter model SF11/C, a PX4Flow and the prism position communicated by the Total Station. These inputs are used by an Extended Kalman Filter (EKF), calculating the position estimation of both aerial platform and arm end-effector.

Description of the bridge inspection system

To obtain the deflection of a beam, the inspection procedure will start with the creation of the 3D map through the total station. In this map, the field inspector will select which points of the girder are needed to calculate its deflection. The prism is placed at the end effector of the aerial manipulator. The autopilot is communicated by wifi with the total station, thus the platform controller will receive the position of the prism. This position is integrated on the extended Kalman filter to obtain the full state of the system and it can be used by the aerial manipulator position control. Thanks to the data sent by the Total Station, the aerial platform can navigate to the inspector selected points and to perform the measurements. The field inspector will receive these measurements and will calculate the girder profile. Then, this calculus should

be compared with old profiles to get the current deflection and, finally evaluate the state of the structure and check the safety. The scheme of this full system is shown in Figure 4.14

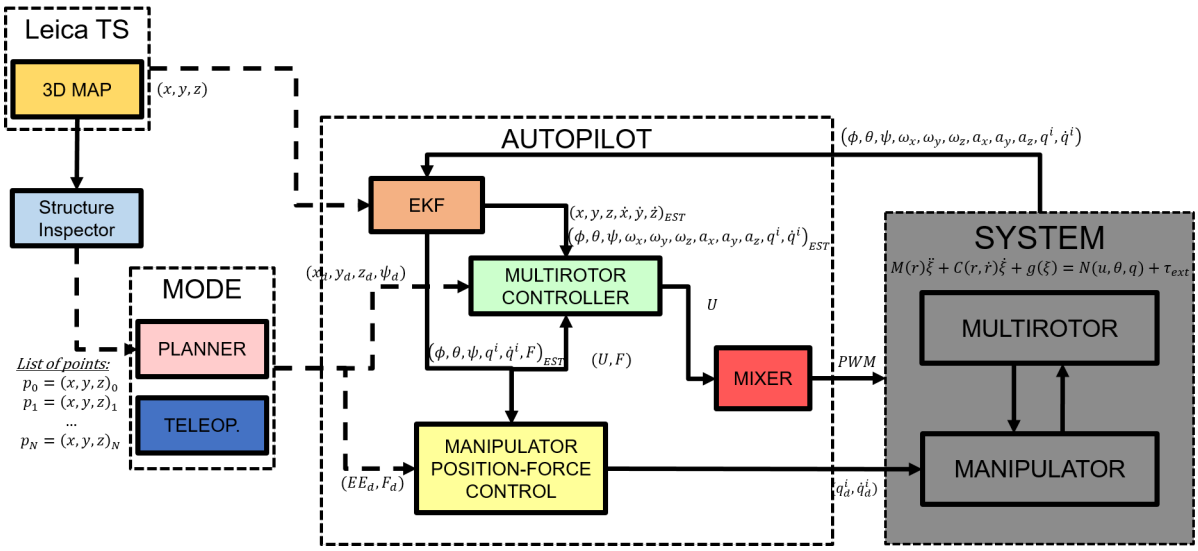

Figure 4.14: Scheme of multirotor layers.

4.2.2 Modelling

In chapter 2, we have presented three methods to derive the dynamics equations of a mechanical system. All these methods consider rigid joints. However, in this application, the prototype has been designed with compliant joints. To model these flexible elements, we have used the reduced flexible joint robot model (Spong, 1989). Then, through the Lagrange-Euler formulation, the dynamic model of the system is given by,

$$\begin{aligned} M(\varphi)\ddot{\varphi} + C(\varphi, \dot{\varphi})\dot{\varphi} + g(\varphi) &= N(u, q, \gamma) + \tau_{ext} \\ B\ddot{q} + N(u, q, \gamma) &= \tau_m \end{aligned} \tag{4.13}$$

where the inertia matrix $M(\varphi) \in \mathbb{R}^{N \times N}$ must be symmetric and positive definite. The term $C(\varphi, \dot{\varphi})\dot{\varphi}$ represents Coriolis and centrifugal forces and complies with the property

$\dot{M}(\varphi) = C(\varphi, \dot{\varphi})^\top$, which is skew-symmetric of $\dot{M}(\varphi) - 2C(\varphi, \dot{\varphi})$.The gravitational force is given by $g(\varphi) \in \mathbb{R}^N$ and the term τ_{ext} is the vector of external forces generated by the interaction with the environment. Matrix B is the inertia of servos' shaft and frame and τ_m is the torque generated by the motor. The vector $N(u, q, \gamma)$ is used to represent the forces and torques acting on the system, where $u \in \mathbb{R}^6$ is the forces and torques generated by the rotors over the aerial platform presented in the above subsection and which it is defined by the equation,

$$u = \begin{bmatrix} F_x \\ F_y \\ F_z \\ \tau_x \\ \tau_y \\ \tau_z \end{bmatrix} = \begin{bmatrix} 0 & -\frac{b\sqrt{2}sin(a)}{2} & 0 & \frac{b\sqrt{2}sin(a)}{2} & 0 & \frac{b\sqrt{2}sin(a)}{2} & 0 & -\frac{b\sqrt{2}sin(a)}{2} \\ 0 & -\frac{b\sqrt{2}sin(a)}{2} & 0 & -\frac{b\sqrt{2}sin(a)}{2} & 0 & \frac{b\sqrt{2}sin(a)}{2} & 0 & \frac{b\sqrt{2}sin(a)}{2} \\ b & bcos(a) & b & bcos(a) & b & bcos(a) & b & bcos(a) \\ 0 & l_2bcos(a) & l_1b & l_2bcos(a) & 0 & -l_2bcos(a) & -l_1b & l_2bcos(a) \\ -l_1b & -l_2bcos(a) & 0 & l_2bcos(a) & l_1b & l_2bcos(a) & 0 & -l_2bcos(a) \\ -d & -dcos(a) & d & dcos(a) & -d & -dcos(a) & d & dcos(a) \end{bmatrix} \begin{bmatrix} \Omega_1^2 \\ \Omega_2^2 \\ \Omega_3^2 \\ \Omega_4^2 \\ \Omega_5^2 \\ \Omega_6^2 \\ \Omega_7^2 \\ \Omega_8^2 \end{bmatrix} \tag{4.14}$$

where b and d are the thrust and drag coefficients, a is the tilt angle of the rotors in the bottom layer and $l_i (i = 1, 2)$ are the distance between the rotors and the geometric center in each layer. The torques given by the compliant joints are defined by $K(q - \gamma)$ and then $N(u, q, \gamma)$ can be expressed as

$$N(u, q, \gamma) = \begin{bmatrix} I_{6\times6} & 0 \\ 0 & K \end{bmatrix} \begin{bmatrix} u \\ q - \gamma \end{bmatrix} \tag{4.15}$$

Herein, $K \in \mathbb{R}^{N\times N}$ is a diagonal matrix and represents the elastic constant terms of each joint and $q = [q_1 ... q_k]^\top \in \mathbb{R}^N$ are the servos' angular positions.

4.2.3 Position-Force controller

In order to done the structure inspection tasks, it is needed to design a position-force controller for the aerial manipulator system designed. The first step is to estimate the torques and forces acting in each link. Thanks to the PCMs, it is possible to obtain an estimation of these torques and forces. Nevertheless, the use of potentiometers and

springs can induce errors owing to backlash or construction's failures. To compensate and detect these possible errors a method to estimate the deflection angle in each joint has been implemented. Then, for each joint, we should find the position of each joint respect to it, e. g. for the joint j we should calculate the position of $j+1, ..., k$, where k is the end-effector. E. g., for the joint j:

$$\begin{cases} p_{j+1} = \sum_{i=j}^{j+1} T_0(\eta) \left(\prod_{j=1}^{i} T_j(\gamma) \right) p_i \\ \dots \\ p_k = \sum_{i=j}^{k} T_0(\eta) \left(\prod_{j=1}^{i} T_j(\gamma) \right) p_i \end{cases} \tag{4.16}$$

where $T_0(\eta)$ is the aerial vehicle rotation matrix and can be defined as,

$$T_0(\eta) = \begin{bmatrix} c_\psi c_\theta & c_\psi s_\theta s_\phi - s_\psi c_\phi & c_\psi s_\theta c_\phi + s_\psi s_\phi \\ s_\psi c_\theta & s_\psi s_\theta s_\phi + c_\psi c_\phi & s_\psi s_\theta c_\phi - c_\psi s_\phi \\ -s_\theta & c_\theta s_\phi & c_\theta c_\phi \end{bmatrix} \tag{4.17}$$

with c_α and s_α defined as $cos(\alpha)$ and $sin(\alpha)$, respectively. Then, we could obtain the position of the center of gravity using the following equation:

$$CoG_j = \frac{\sum_{i=j}^{k} m_j p_j}{\sum_{i=j}^{k} m_j} \tag{4.18}$$

where m_j is the weight of the joint j. Now, we can obtain the distance between the center of gravity and the rotation axis of the joint j, δ_j. Furthermore, we need to calculate the angle, β_j, of the vector formed by the position of the center of gravity and position of the rotation axis for the joint j as (see Figure 4.15):

$$\begin{aligned} \beta_j &= atan2(CoG_j y, CoG_j x) \\ \delta_j &= \sqrt{CoG_{jx}^2 + CoG_{jy}^2} \end{aligned} \tag{4.19}$$

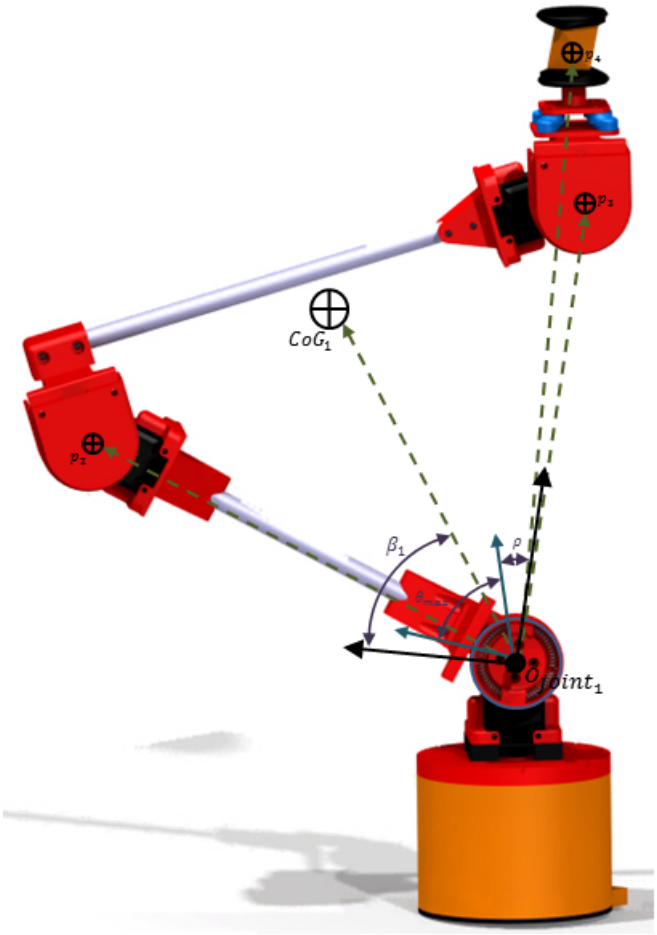

Figure 4.15: Scheme used in the method followed to obtain the angle deflection.

Then the torque in the joint j due to the gravity force can be obtained as:

$$\tau_j = \left(\sum_{i=j}^{k} m_j\right) \delta_j g cos \left(\beta_j + \sum_{i=1}^{j}(\gamma_i) + \rho\right) \tag{4.20}$$

where g is the gravity acceleration. Finally, the angle's deflection for each arm's joint j, $\nabla\hat{\gamma}_j$, can be calculated as:

$$\nabla\hat{q}_j = \frac{\tau_j \gamma_{max}}{dkL} \tag{4.21}$$

where L is the free length of the spring, k is the stiffness constant, d is the radius of the circle in which the springs are located and q_{max} is the arc angle formed by the spring.

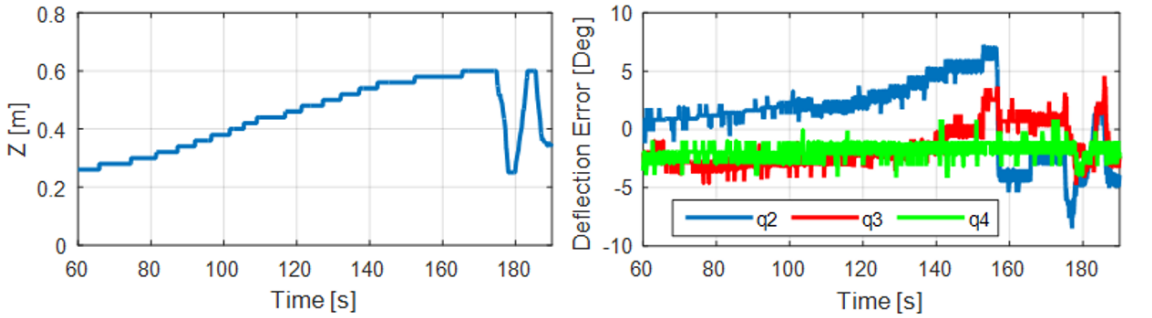

Figure 4.16: Errors between the deflection measured by the deflections estimates when the arm is moving in the z-axis.

Figure 4.16 shows the errors between the deflections measured by the potentiometers and the deflections estimations done through this method when the arm is moving on the z-axis. This experiment demonstrates the errors due to backlash and friction considering that when the arm moves slowly the errors increase and when the arm moves fast, these errors decrease. Nevertheless, an accumulative error remains in the measurement. Furthermore, this figure shows as the potentiometers have deg. of accuracy. Thanks to these estimations, the measurement errors induced by backlash can be detected and the estimation of a force applied over the end-effector can be improved. Then, using the method developed a position-force controller has been implemented. For the system described by 4.13, the following equations of equilibrium can be obtained by setting the accelerations and velocities coordinates to zero (Spong, 1989),

$$\begin{aligned} -K(\gamma - q) &= u \\ K(\gamma - q) + g(\gamma) &= \tau_{ext} \end{aligned} \tag{4.22}$$

where u is the torque motor in 4.13 that serves as a control input. Thanks to the equilibrium equation 4.22, if $\tau_{ext} = 0$ the control variable, $\bar{\gamma}$, can be defined as (Albu-Schaffer et al., 2005):

$$\bar{\gamma} = q - K^{-1} g(\gamma_d) \tag{4.23}$$

where γ_d is the desired joint position, then, a classical control solution for a robotic arm with elastic joints would be compliant controller with constant gravity compensation in which the control law would be:

$$u = J^T(\bar{\gamma}) K_x \tilde{x}(\bar{\gamma}) + g(\gamma_d) \tag{4.24}$$

where the control input u is obtained by a proportional term acting over the end effector pose error, a derivative term used as a motor damping and the gravity compensation calculated by the desired joint position, γ_d. K_x and K_d are the proportional and derivative diagonal positive gain matrices. In Spong (1989), the stiffness equation is defined as:

$$K_x \tilde{x} = K_x (x - x_d) = F \tag{4.25}$$

where K_x is a diagonal positive gain matrix, x_d is the desired end-effector position and F is the generalized external force. Thanks to the potentiometers placed in each joint, the arm controller can obtain the difference between the actuator angle position and the joint angle position generated by an applied force over the arm. The potentiometers measure the angle deflection in each joint, $\hat{pot}_i = (q_i - \gamma_i)$. Then, equation 4.25 can be rewritten as:

$$\hat{F} = J^{-T}(K\hat{pot} - g(\gamma)) \tag{4.26}$$

Thus the gravity compensation term can be obtained as:

$$g(\gamma_d) = K \nabla \hat{\theta}(\gamma_d) \tag{4.27}$$

where $\nabla\hat{q}(\gamma)$ is the deflection angle estimation. Now, it is possible to define the force error as:

$$e_F = F_d - J^{-T}K(\hat{pot} - \nabla\hat{q}(\gamma_d)) \tag{4.28}$$

And therefore, the torque control signal can be defined as:

$$U_F = W\left(p, F_{d,},\ \tau_{ext}\right) K_F(F_d - J^{-T}K(\hat{pot} - \nabla\hat{q}(\gamma_d)) \tag{4.29}$$

where K_F is a diagonal gain matrix and $W(p, F_d, \tau_{ext})$ is a time-varying diagonal weight-matrix defined as:

$$W\left(p, F_d,\ \tau_{ext}\right) = \begin{cases} 0, & F_d = 0 \ and \ \tau_{ext} = 0 \\ \alpha I, & F_d = 0 \ and \ \tau_{ext} > 0 \\ \alpha I, & F_d > 0 \ and \ \tau_{ext} = 0 \\ (1-\alpha)\, I, & F_d > 0 \ and \ \tau_{ext} > 0 \end{cases} \tag{4.30}$$

where I is an identity matrix and $\alpha(p)$ is given by Lippiello et al. (2013),

$$\alpha(p) = \frac{1+\underline{\alpha}}{2} + \frac{1-\underline{\alpha}}{2} tanh(k_1\pi\frac{p-\delta w}{\Delta w - \delta w} - k_2\pi) \tag{4.31}$$

where $\alpha \in [\underline{\alpha}, 1]$ and δw and Δw ($\Delta w > \delta w$) are distance thresholds corresponding to $\alpha \cong 1$ and $\alpha \cong \underline{\alpha}$ respectively. The gains k_1 and k_2 are used to modify the behavior of the function. With $W(p, F_d, \tau_{ext})$ is possible to achieve the performance in the three cases described previously. Basically, the function $W(p, F_d, \tau_{ext})$ works as a state machine identifying each case and modifying the controller gains, e. g. if the end-effector is in a desired position and an external force acts over the arm, the control gains (initially to zero) increase according to the position error increases. It allows the arm to find a zero-force position and protecting the system. If this force disappears the arm recovers the desired position. Another case is when the arm has to apply a desired force in a desired position, in this case the force control acts while the arm is closed to the desired position. If during this case an external torque appears the function inverts its behavior adapting the joint position to reject the external torque

while trying to hold the desired force. Now, the force control can be introduced in the control law 4.24:

$$u = J^{-T}(\bar{\gamma})U_\tau - K_d\dot{q} + g(\gamma_d) \tag{4.32}$$

The compliant robotic arm designed uses Herkulex smart servos as actuators. A torque controller cannot be used with these servos. Thus the control strategy should generate a desired servo angular position to control both the end effector position and the applied force. Therefore, the control law 4.32 must be rewritten in order to obtain a desired servo position, q_d. Using the equilibrium equation 4.22, equation 4.32 can be rewritten as:

$$q_d = K^{-1}(J^T(\bar{\gamma})U_\tau - K_d\dot{q} + g(\gamma_d)) + \gamma_0 \tag{4.33}$$

where γ_0 is a joint position in an equilibrium point. Supposing that the robotic arm has rigid joints then γ_0 can be calculated by integrating the joint velocity obtained by the inverse Jacobian and an end effector pose error,

$$\dot{\gamma}_0 = J^{-1}k_p(p_{EE_d} - p_{EE}) \tag{4.34}$$

where k_p is a diagonal gain matrix.

4.2.4 Experiments

One of the tasks in structural inspection is the measurement of the deflection of the bridge's girder over time. To accomplish enough measurement accuracy, the topographic prism must hold in the desired position for a certain time. To complete the task, some measurements along the girder should carry out. Therefore, the aerial manipulator designed for the fulfilment of these tasks should be able to hold a desired position and force in a contact point during the time needed to attain sufficient accuracy by the sensor (see Figure 4.17).

In order to evaluate the system designed and the controller proposed both testbench and flying experiments have been done. First, the results of the testbench experiments

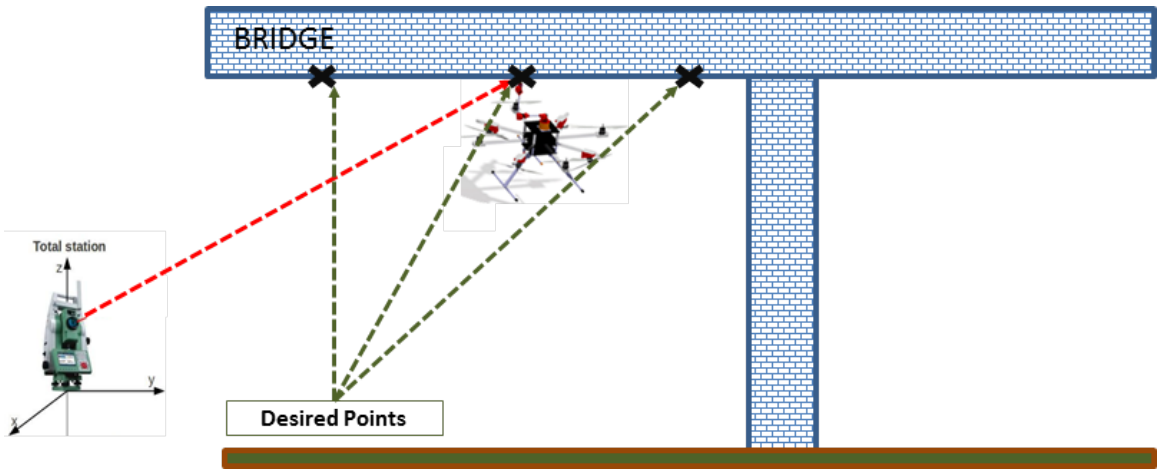

Figure 4.17: Illustration of steps followed in an experiment to achieve the beam deflection using the system developed.

will be presented. Second, we will present the results of a flying experiment in which the aerial platform carries out a real subtask necessary to achieve the measurement of the deflection of a bridge's girder.

Testbench Experiments

The arm controller should present a good performance in the following identified cases:

1. The arm is in a desired position and an external force is applied.
2. The arm reaches a desired position and applies a desired force.
3. The arm reaches a desired position, applies a desired force while an external force acts over it.

The external forces applied in cases 1 and 3 can be generates generated by the oscillations of the aerial platform while is flying over a desired altitude. The controller performance has been tested for each proposed case. The first case results have been represented in Figure 4.18.

In this case, the robotic arm was in a desired position and an external force was applied. In this experiment an external force has been applied three times and the

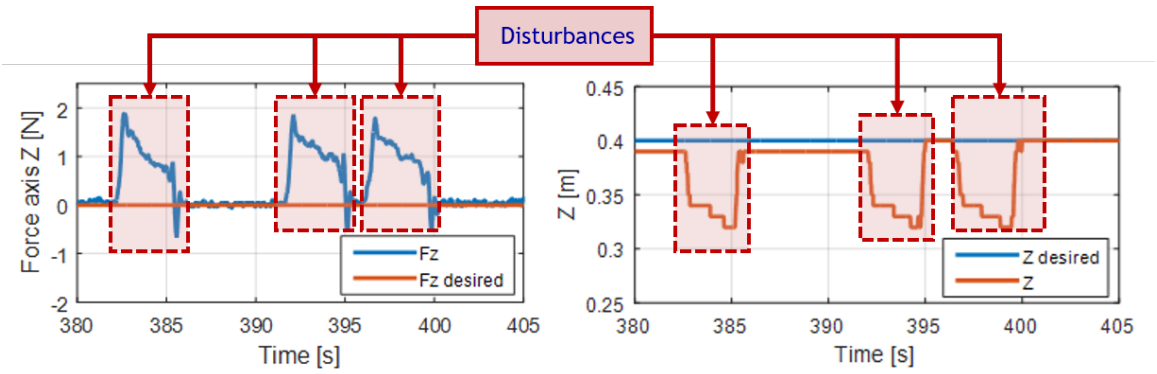

Figure 4.18: Evolution of the force and position z-axis during the first case test.

results are similar each time. When the force was applied the springs absorbed a percentage of it, then the controller acted to try to reduce the force induced over the servos. The result is a change in the position servos and therefore in the end effector position. In addition, The results demonstrate the system performance when the position of the end effector change and the external force is absorbed and viceversa, when the external force disappears the end effector recovers it desired position. The results of the second and third cases are shown in Figure 4.19. In these cases, first the arm reaches a desired position and applies a desired force and then an external force perturbation is applied over the arm while it is exercising a desired force.

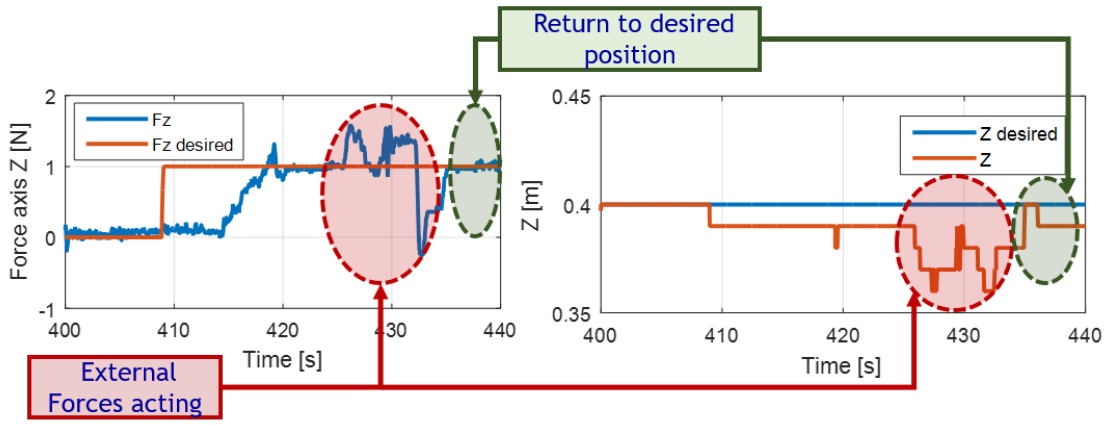

Figure 4.19: Evolution of the end-effector z-axis position during the second and third cases test.

Figure 4.19 (right) shows as the force applied by the end effector reaches the desired force. At the second 425 approximately, an external force appears and thanks to the controller implemented it can be rejected. This external force increases and then it disappears. For this reason, the figure shows an oscillation at second 432 until the arm recovers the desired position and force. Figure 4.19 (left) shows the position in z-axis during the experiment. It possible to analyze as the desired Z position changes when the perturbation external force appears and when the end-effector returns to the desired position at the same moment in which the perturbation disappears.

Flight Experiments

The goal of these experiments is to use the aerial manipulator developed to perform the above operation, holding the topography prism in a desired position in contact with the girder. Figure 4.20(Left) shows the force in z-axis applied by the end-effector in the girder surface. During the experiment, the multirotor aircraft has taken off and has been commanded to hold a desired altitude (see Figure 4.20)(Right). When the platform has reached the desired altitude the robotic arm starts to move until the end-effector has contacted with the surface of the girder and reaches the desired force. This experiment can be related to the third case mentioned in the controller subsection. In this case, the external torque has been generated by the altitude oscillations while the end-effector was contacting with the surface of the girder.

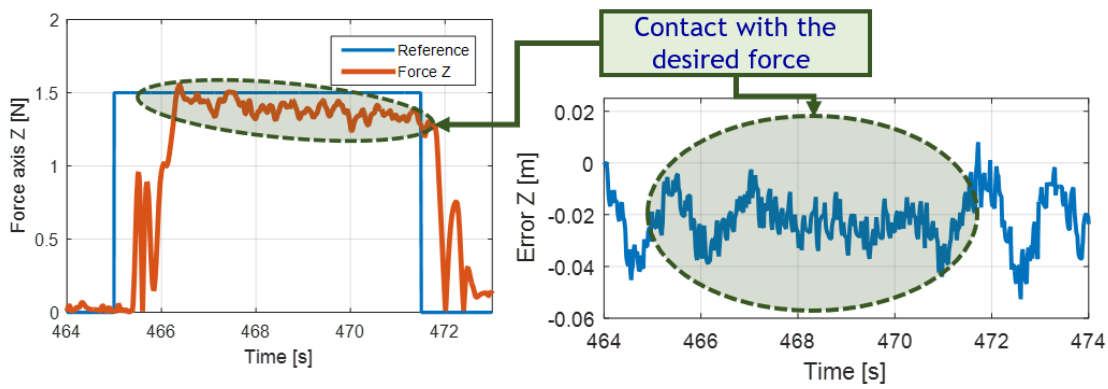

Figure 4.20: (Left)Z axis force reference and estimation.(Right)Z error estimation.

4.3 Application 3 AEROBI - Quadrotor with environment interaction for structure inspection

Case 2 presents a solution for the bridge inspection using aerial manipulators. The proposed prototype includes a compliant arm with the capability to measure the contact forces. This approach with more development can be considered as a more general solution, it can be used to carry out bridge girders and abutments inspections. In this case, we present a prototype also designed to bridge inspection but focusing on the task consisting of the measurement of the girder deflections. Furthermore, Thanks to the design proposed, the aerodynamic effects that arise flying close to the bridge, can be exploited to improve the main performances of the aircraft, such as, the power consumption and the accuracy during the inspection task. A prototype developed is shown in Figure 4.21.

Figure 4.21: CAD of the aerial platform designed (ARBI) and the real platform developed

In the following sections, we introduce the designed proposed. Then, we derive the equation os motion of the system including the ceiling effect. This aerodynamic effect

was presented and modelling in chapter 2. Using this model, we propose a control strategy that it will be validated through the flight experiments shown in the last subsection.

4.3.1 System Description

To done the main task of this aerial manipulation application, this aerial platform has been specially designed and implemented with the goal of maximizing the benefits of the ceiling effect (see Figure 4.21). This platform consists of a cross layout quadrotor with the propulsive system and the avionics onboard covered in a full carbon filter frame. The propulsive system consists of DJI 231E rotors with 9" propellers DJI and 420Lite ESC. The onboard avionics consist of a custom autopilot code running in a Raspberry PI 3 Model B connected to the Emlid's sensors shield Navio2. The aerial platform and the Ground Control Station (GCS) are connected by Wi-Fi Technology. A range sensor model SF11/C has been also mounted in the platform. This platform is also equipped with a passive link which has a reflector prism. This prism is used to accomplish the measurements during the inspection and to estimate the position of the aircraft during the flight in the position control loop. These measurements are carrying out with a robotic total station model Leica Geosystem MS50. The accuracy of these measurements is about 1 cm in flight and increasing during the contact inspections to 0.1 mm. The maximum frequency of the measures is 20 Hz.

The hardware/software architecture is presented in Figure 4.22. This scheme shows that the autopilot is connected to the GCS through Wi-Fi link. The robotic Total station is also connected to the GCS through a serial port. The GCS receives the prism position and sends it to the aerial platform, acting as a bridge between the robotic total station and the aerial platform. However, the measurements of the Total station are treated and filtered onboard for safety conditions.

The autopilot used in this work is the GRVCautopilot which has been also developed during this thesis. This autopilot allows us to implement control techniques using MATLAB/Simulink. Then, using MATLAB Code Generator and Simulink External Mode, the controllers run in the aerial platform while the sensor data are synchronized

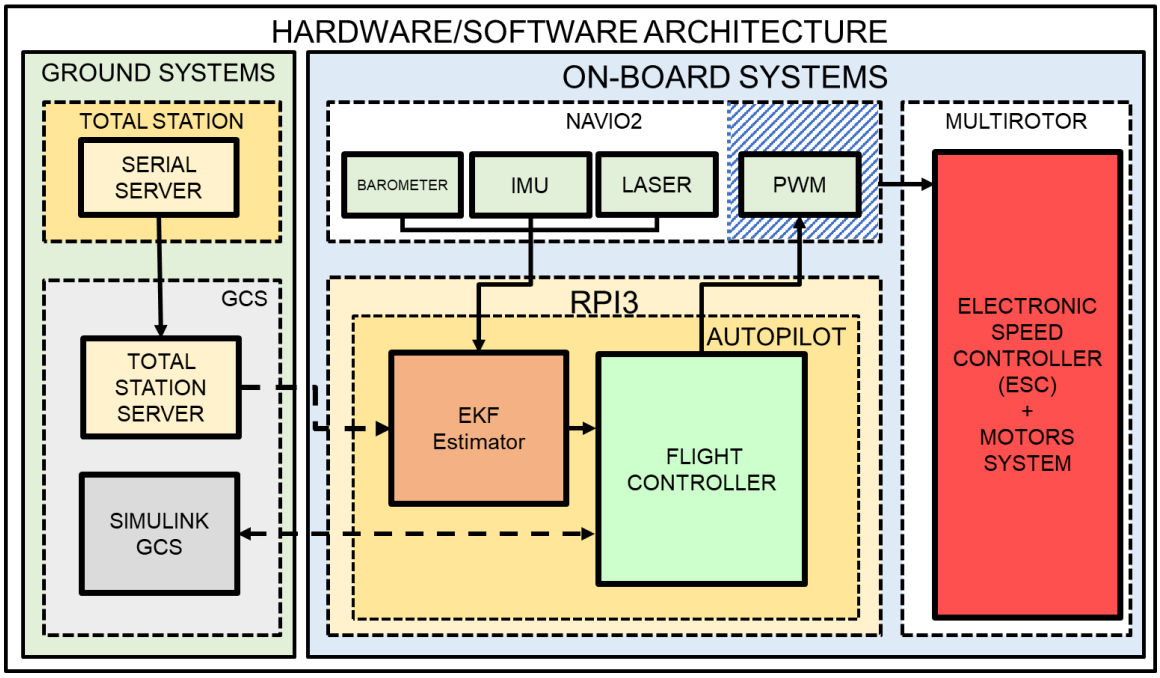

Figure 4.22: Hardware/software architecture. WiFi communication is represented by dashed arrows and wired communication by the bold arrows.

and visualized in the ground station in Real-Time. Parameters like control gains can be also modified without any recompilation. More details about the autopilot implemented can be seen in the appendix B.1.

4.3.2 Modelling

The dynamic model of this system has been derived using the Newton-Euler formalism introduced in chapter 2. Thus, defining a set of generalized coordinates as $\varphi = [x, y, z, \phi, \theta, \psi]^T$, the equations of motion are given by

$$\ddot{\varphi} = \begin{bmatrix} 0 \\ 0 \\ -g \\ \dot{\theta}\dot{\psi}\frac{I_y - I_z}{I_x} - \frac{J_r}{I_x}\dot{\theta}\Omega \\ \dot{\psi}\dot{\psi}\frac{I_z - I_x}{I_y} - \frac{J_r}{I_y}\dot{\phi}\Omega \\ \dot{\theta}\dot{\phi}\frac{I_x - I_y}{I_z} \end{bmatrix} + \begin{bmatrix} \frac{1}{I_m}I_3 & 0 \\ 0 & \sigma\mathbb{I}^{-1} \end{bmatrix} F(\varphi) + F_{ext} \tag{4.35}$$

with

$$\sigma = \begin{bmatrix} d & 0 & 0 \\ 0 & d & 0 \\ 0 & 0 & 1 \end{bmatrix} \qquad \mathbb{I} = \begin{bmatrix} I_x & 0 & 0 \\ 0 & I_y & 0 \\ 0 & 0 & I_z \end{bmatrix} \qquad I_3 = \begin{bmatrix} 1 & 0 & 0 \\ 0 & 1 & 0 \\ 0 & 0 & 1 \end{bmatrix} \qquad \Omega = \Omega_1 - \Omega_2 + \Omega_3 - \Omega_4 \tag{4.36}$$

Here d is the distance between the geometric center of the platform and the center of a rotor, I_i $(i = x, y, z)$ are diagonal terms of the inertia matrix, m is the aerial vehicle total mass and J_r is the rotor moment of inertia. F_{ext} includes external and torques which are not known or modelled, such as contact forces or wind disturbance. Last, vector $F(\varphi) \in \mathbb{R}^6$ encompasses actuator forces and torques exerted by the rotors. These forces and torques depend on the state of the multirotor due to the aerodynamic effects and can be calculated as

$$F\varphi = \begin{bmatrix} R(\phi, \theta, \psi)e_3 T(\varphi) \\ \tau_\phi(\varphi) \\ \tau_\theta(\varphi) \\ \tau_\psi(\varphi) \end{bmatrix} \tag{4.37}$$

Defining the total thrust $T(\varphi)$, as $T(\varphi) = \sum_4^{i=4} T_i(\varphi)$, and taking into account that the platform is a quadrotor in cross configuration, there is a direct correspondence between the four generalized moments and the angular velocities of rotors in which the vector $F(\varphi)$ follows the ceiling effect model introduced in chapter 2 and it is given

by

$$\begin{bmatrix} T \\ \tau_\phi \\ \tau_\theta \\ \tau_\psi \end{bmatrix} = \begin{bmatrix} K_c(z_{c_1})C_T & K_c(z_{c_2})C_T & K_c(z_{c_3})C_T & K_c(z_{c_4})C_T \\ -K_c(z_{c_1})C_T & K_c(z_{c_2})C_T & K_c(z_{c_3})C_T & -K_c(z_{c_4})C_T \\ K_c(z_{c_1})C_T & -K_c(z_{c_2})C_T & K_c(z_{c_3})C_T & -K_c(z_{c_4})C_T \\ C_D & C_D & -C_D & -C_D \end{bmatrix} \begin{bmatrix} \Omega_1^2 \\ \Omega_2^2 \\ \Omega_3^2 \\ \Omega_4^2 \end{bmatrix} \tag{4.38}$$

where z_{c_i} is the distance from the i-rotor to the ceiling surface defined as follows:

$$\begin{bmatrix} z_{c_1} = z_c - \frac{\sqrt{2}}{2}d(sin(\theta) - cos(\theta)sin(\phi)) \\ z_{c_2} = z_c - \frac{\sqrt{2}}{2}d(-sin(\theta) + cos(\theta)sin(\phi)) \\ z_{c_3} = z_c - \frac{\sqrt{2}}{2}d(sin(\theta) + cos(\theta)sin(\phi)) \\ z_{c_4} = z_c - \frac{\sqrt{2}}{2}d(-sin(\theta) - cos(\theta)sin(\phi)) \end{bmatrix} \tag{4.39}$$

Herein z_c is the distance from the center of gravity of the multirotor to the ceiling surface.

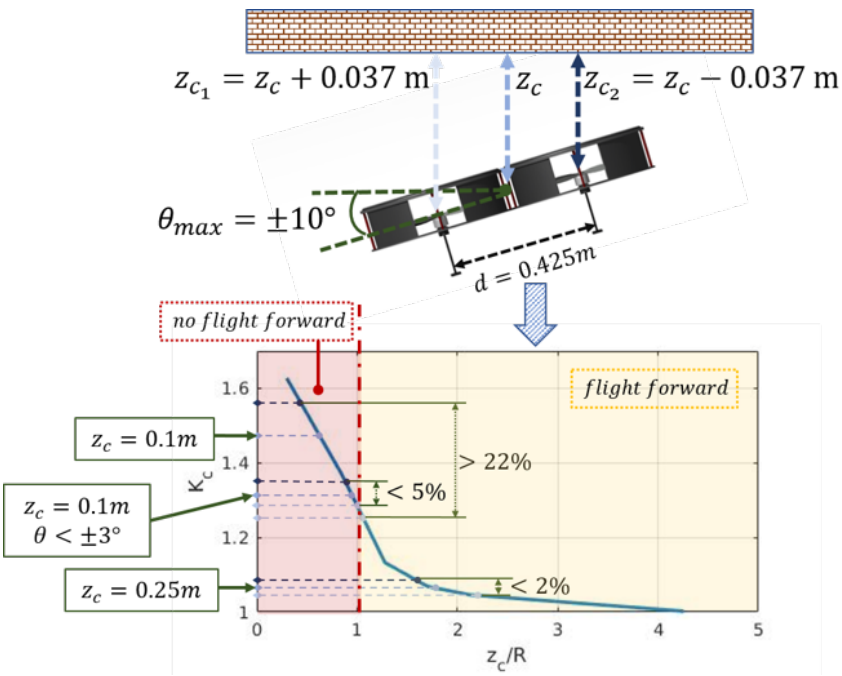

Figure 4.23: Response of a multirotor in ceiling effect and safety flight envelope.

4.3.3 Controller

In this section, we present a nonlinear Lyapunov-based attitude, altitude and position controllers for bridge inspection flights. The main goal of the designed controller is that the quadrotor can fly very close to the beams and carry out contact tasks with safety and accuracy. The ceiling effect is the most critical aerodynamic effect occurring during these inspection tasks. In the previous section, the ceiling effect has been modelled and introduced in the system's equations of motion. The relationship between the control inputs and the angular velocities of the rotors have been shown in equation 4.38. In this expression, the z_{c_i} of each rotor has been calculated to obtain the ceiling effect for each one. Depending of the multirotor attitude, the ceiling effect is different in each rotor. As Figure 4.23 shows, if the aircraft has a pitch angle about ± 10 degrees (flight forward), the aerodynamic ceiling effect is approximately a 22% higher in one rotor than in the other when $z_c = 0.1m$. However, it decreases to 5% when the attitude angles are about ± 3 degrees. Furthermore, it decreases to 2% when $z_c = 0.25m$. This result implies that it is possible to make the following assumptions to increase safety during the operation:

Assumption 2 *A forward flight will be done to a minimum distance of* $0.25m$ *to the ceiling surface.*

Assumption 3 *The only operation allowed for distances less than* $0.25m$ *will be the hover until reaching the contact with the surface.*

Taking into account these assumptions, the equation 2.40 is linearized in intervals in which the difference between the aerodynamic effects is less than 5% and therefore $z_c \sim z_{c_1} \sim z_{c_2} \sim z_{c_3} \sim z_{c_4}$. Thus, the expression for the control inputs 4.38 can be simplified as follows:

$$U = \begin{bmatrix} K_c(z_c) & 0 & 0 & 0 \\ 0 & K_c(z_c) & 0 & 0 \\ 0 & 0 & K_c(z_c) & 0 \\ 0 & 0 & 0 & 1 \end{bmatrix} = \begin{bmatrix} C_T & C_T & C_T & C_T \\ -C_T & C_T & C_T & -C_T \\ C_T & -C_T & C_T & -C_T \\ C_D & C_D & -C_D & -C_D \end{bmatrix} \begin{bmatrix} \Omega_1^2 \\ \Omega_2^2 \\ \Omega_3^2 \\ \Omega_4^2 \end{bmatrix} \tag{4.40}$$

Then

$$\begin{bmatrix} T \\ \tau_\phi \\ \tau_\theta \\ \tau_\psi \end{bmatrix} = \begin{bmatrix} K_c(z_c) & 0 & 0 & 0 \\ 0 & K_c(z_c) & 0 & 0 \\ 0 & 0 & K_c(z_c) & 0 \\ 0 & 0 & 0 & 1 \end{bmatrix} \begin{bmatrix} U_z \\ U_\phi \\ U_\theta \\ U_\psi \end{bmatrix} \tag{4.41}$$

Attitude Controller

Following the control strategy introduced in chapter 2, let defined the angular and rate tracking error as

$$\begin{aligned} e_\phi &= \phi - \phi_d & e_{\dot\phi} &= \dot\phi - \dot\phi_d + k_\phi e_\phi \\ e_\theta &= \theta - \theta_d & e_{\dot\theta} &= \dot\theta - \dot\theta_d + k_\theta e_\theta \\ e_\psi &= \psi - \psi_d & e_{\dot\psi} &= \dot\psi - \dot\psi_d + k_\psi e_\psi \end{aligned} \tag{4.42}$$

Thus the control inputs are given by

$$\begin{aligned} U_\phi &= \frac{I_x}{dK_c(z_c)}(\dot\theta\dot\psi(\frac{I_y - I_z}{I_x}) - \frac{J_r}{I_x}\dot\theta\Omega + P_\phi e_\phi - D_\phi e_{\dot\phi}) \\ U_\theta &= \frac{I_y}{dK_c(z_c)}(\dot\phi\dot\psi(\frac{I_z - I_x}{I_y}) - \frac{J_r}{I_y}\dot\phi\Omega + P_\theta e_\theta - D_\theta e_{\dot\theta}) \\ U_\psi &= I_z(\dot\phi\dot\theta(\frac{I_x - I_y}{I_z}) + P_\psi e_\psi - D_\psi e_{\dot\psi}) \end{aligned} \tag{4.43}$$

Altitude Controller

In the first step designing the proposed altitude controller, the tracking error and the speeds tracking error are defined as follows:

$$\begin{aligned} e_z &= z - z_d \\ e_{\dot z} &= \dot z - \dot z_d + k_z e_z \end{aligned} \tag{4.44}$$

Thus the control input is given by

$$U_z = \frac{m}{cos(\phi)cos(\theta)K_c(z_c)}(g + P_z e_z - D_z e_{\dot{z}}) \tag{4.45}$$

The first one is to keep the altitude during a flight forward when $R/zc > 1$ and therefore $Kc(zc) \approx 1$. The second one is during a contact mission. In this case, the attitude angles, roll and pitch, should be small and when the multirotor is flying close to the ceiling, the function $Kc(zc)$ should increase and the multirotor should be able to keep the altitude as well as reducing the thrust input and therefore, minimizing the energy consumption.

Position Controller

Following the control strategy introduced in chapter 2, let defined the position and speed tracking error as

$$\begin{aligned} e_x &= x - x_d \qquad & e_{\dot{x}} &= \dot{x} - \dot{x}_d + k_x e_x \\ e_y &= y - y_d \qquad & e_{\dot{y}} &= \dot{y} - \dot{y}_d + k_y e_y \end{aligned} \tag{4.46}$$

Thus the control inputs are given by

$$\begin{aligned} U_x &= \frac{m}{U_z}(P_x e_x - D_x e_{\dot{x}}) \\ U_y &= \frac{m}{U_z}(P_y e_y - D_y e_{\dot{y}}) \end{aligned} \tag{4.47}$$

The generated position and control signals are used to obtain the desired roll, ϕ_d, and pitch angles, θ_d.

4.3.4 Experiments

First experiments, which were carried out piloted by a human, show that the aircraft is very unstable at the end of the contact phase. The results in Figure 4.24 show that the pilot must significantly decrease the thrust signal at least until 40% less than the thrust hover to finish the contact task. This situation leads to conditions in which the

aircraft critically loses its altitude and could generate a dangerous flight condition. Then, it becomes clear the need for implementing an automatic control strategy to fix this behavior. This is one of the main conclusions of this work.

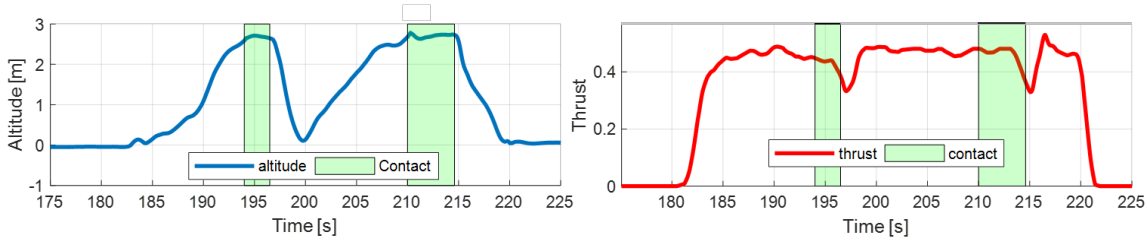

Figure 4.24: Altitude telemery results during in manual flight.

The next experiment was accomplished with the automatic control strategy proposed in the controller subsection. In this case, the results of Figure 4.25 and Figure 4.26 show the altitude controller result, as well as, the values of the thrust, the aerodynamic ceiling effect estimation and the vertical velocity. These results reveal that the controller implemented allows the platform to fly in safe conditions when it approaches and moves away from the bridge surface. Moreover, Figure 4.25 also shows how the controller acts during the contact and in the second result, which is about the thrust commanded, it can be seen that, despite the oscillations due to the error in the state estimation, the mean value of thrust (represented with the red dashed line) decreases as a consequence of taking into account the ceiling effect in the nonlinear controller.

It is important to remark that one of the most important benefits of this nonlinear control appears in the z-velocity controller. The result of Figure 4.26 shows that the nonlinear controller is faster and the un-stick command is followed in a more efficient way. For instance, this result clearly shows that the nonlinear controller easily follows the reference without a remarkable delay ($< 1s$) while a standard PID controller needs to integrate and accumulate too much error for following the reference ($4s$) because this one does not take into account the aerodynamic ceiling effect.

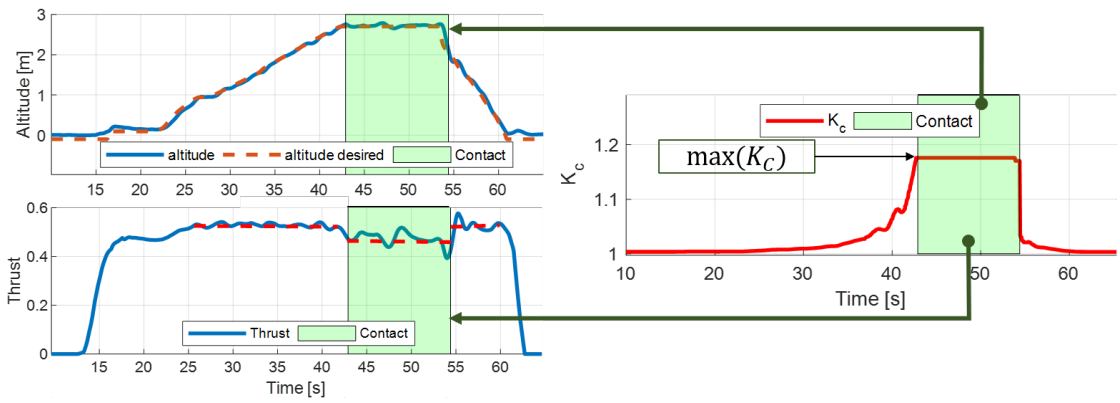

Figure 4.25: Altitude nonlinear controller results. Altitude vs altitude reference control, thrust and mean value during the flight and contact (red dashed), and estimation of the ceiling effect factor (K_c) during the flight.

Autonomous Inspection

Last experiments consisted of accomplishing a full inspection by contact in autonomous mode. These results, which are presented in Figure 4.27 clearly show that the system is able to navigate between different contact points in safety conditions.

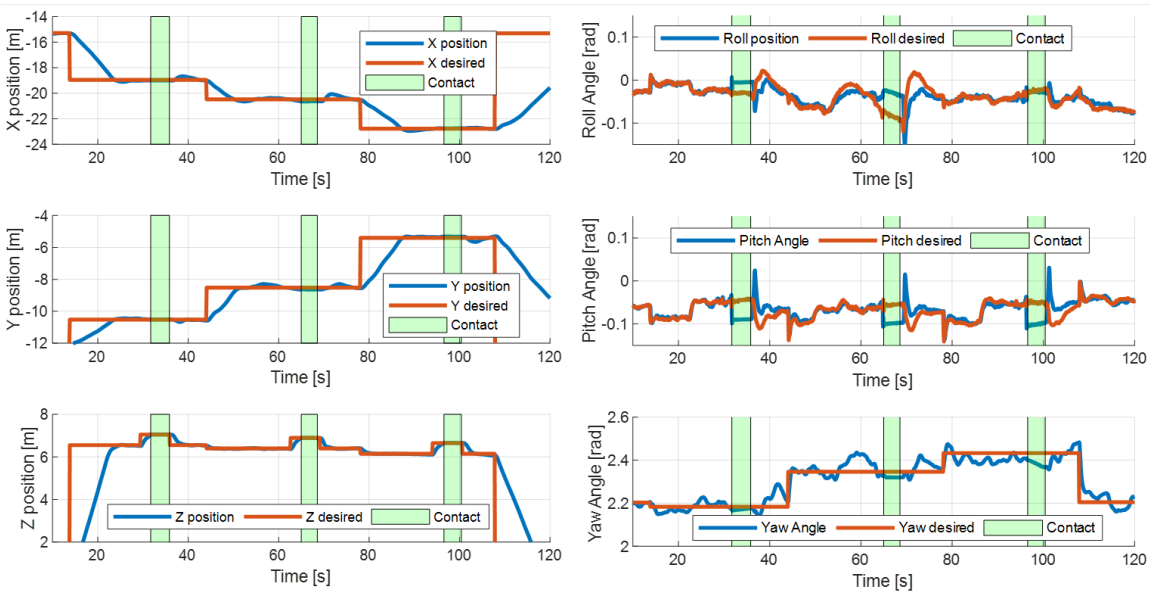

Figure 4.27: (Left)Position controller results during an autonomous mission.(Right)Attitude controller results during an autonomous mission.

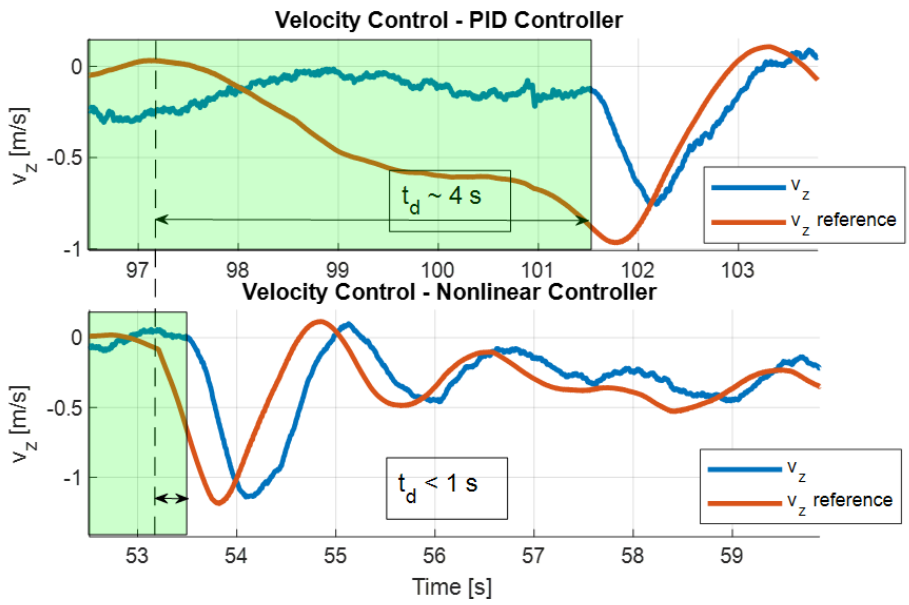

Figure 4.26: PID vs Nonlinear altitude controller comparison. Green backgrounds represent the contact condition.

In Figure 4.28 a sequence of pictures of an experiment can be seen. This figure shows which are the steps followed by the aerial platform to carry out a contact an achieve a deflection measurement in a goal point of the beam.

Future work related to this research will be focused on the end-user of this technology and the inspection application. The aims of these works will be: increase the applicability of this technology, increase its the Technology Readiness Level (TRL), and, turn it in a competitive option in commercial exploitation.

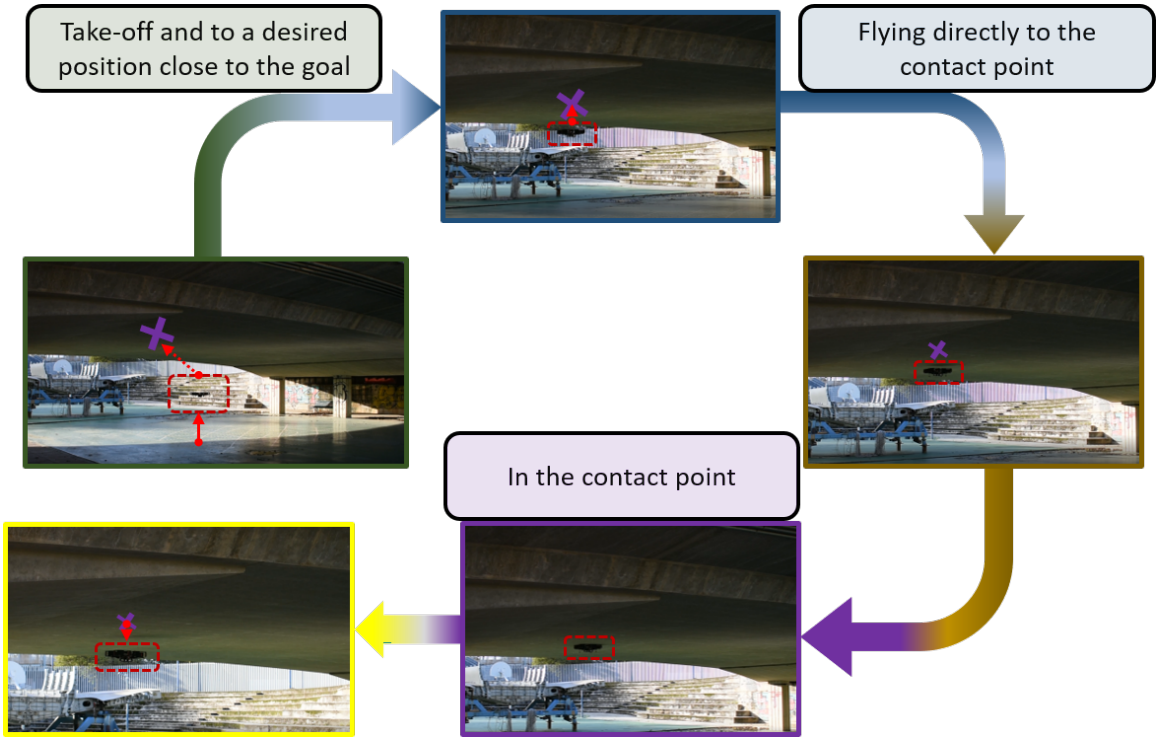

Figure 4.28: Sequence of picture of an experiment.

Chapter 5

Conclusions and future works

5.1 Conclusions

An aerial manipulator system is an aerial platform equipped with one or multiple robotic arm. The main objective in the development of this technology is to achieve the realization of operations or manipulation tasks in high altitude or in areas which the access could be difficult or dangerous for humans. Thanks to the development of functional aerial manipulators, the cost in time and resources typically dedicated in civil or industrial structure inspections could be reduced. Applications of these aerial robots for chemical plants, wind turbines or power lines could be a reality in few years and this can be seen in the continuous growth of the community research interest and the number of European projects allocated to the development of this technology. However, the aerial platforms typically used, multirotors or helicopters, still present limitations in payload and time flight, moreover the interaction with the environment and the arm movement generate coupled disturbances which affect to the accuracy in operation tasks and presenting a big challenge in the robotic research field.

This thesis has presented the theoretical study, design, development and experimental tests of several prototypes of aerial manipulators, demonstrating their validation in real outdoor scenarios for the most cases. The theoretical study presented has involved since the typical methods used to obtain the dynamic equations of mechanical systems from the study of the aerodynamic forces, designing an effective control strategy

suitable for the different kinds of aerial manipulators studied in this thesis. In each prototype designed we have taken into account the equipment needed to achieve the best result for it application case, keeping in mind the weight, payload, sensors needed, flight time and arm reach to carry out each goal task of each prototype.

Addressing the issues of the aerial manipulation in outdoor scenarios is a challenge due to the integration of the hardware needed to achieve it. Thanks to the design and implementation of AMUSE prototype, we have learned to choose the correct motorization for each platform, the integration of a commercial robotic arm in a multirotor and the best location of each hardware included in the platform without generating any electromagnetic interference between them and centering the center of mass of the system. One example of the problems which we have addressed could be the typical electromagnetic interference between the magnetometers and ESCs or how the hard disk and communication buses of a PC can affect to the GPS-RTK radio links. these and other problems have been solved and the results like grasping of objects in autonomous flight mode for outdoor scenarios have been shown in chapter 3. In this chapter, an adaptation for the control strategy presented in AMUSE was implemented for a helicopter equipped with the same commercial arm, deriving the dynamic model of the system through Kane's method and validating the controller using a high-fidelity Modelica simulator.

To carry out the task of structure inspections using aerial robots, three aerial manipulator systems have been presented in this thesis. The first two have been octorotors equipped with two different custom robotic arms. The third is a quadrotor specifically designed to carry out the bridge inspection by contact. The first aerial manipulator system presented was equipped with a robust and heavy arm specially designed to withstand contact forces. Its end effector can be endowed with an ultrasonic sensor to measure structural crash. The dynamic model of the system and a control scheme have been shown and several experimental tests in a real bridge have been done. This first prototypes served us to lead the way in the use of aerial manipulators in the structure inspections. For the purpose of improving the time flight and the system behavior in operations which require a direct interaction with the environment, we decide to design a lightweight custom robotic arm to achieve more

time flight reducing the system total weight. Furthermore, a compliant mechanism was implemented and added for each joint to be able the capability of measuring torques and contact forces, and therefore to increase the safety and system behavior during the contact operations. This compliant arm has been integrated into a novel configuration multirotor and experiments in a real bridge have been presented to validate the robotic arm designed and the position-force controller proposed. In this second prototype, the idea was located a topographic prism in the end effector to measure the deflection of girder and at the same time using the position of this prism as a positioning system for the platform. Although this prototype was designed to carry out not only deflection measurements of ceiling girders, but also horizontal girders, to accomplish the task of measuring the deflection of ceiling girders the aerial system can be simplified resulting in the third prototype presented in chapter 4. This aerial system consists in a quadrotor specially designed to draw on of the ceiling effect. A controller has been proposed to take into account the ceiling effect, optimizing the time flight of the platform and the stability when the ceiling effect is acting. The topographic prism is also used as a positioning system and to measure the deflection of the ceiling girders of a bridge. Experiments in a real bridge are shown to test the controller proposed. To implement the whole control of the platform, a new autopilot system has been developed using a Raspberry pi 3 with a Navio 2. The details in the hardware and software architecture of this new autopilot have been also presented in the appendix section.

In conclusion, this thesis has presented the design, development and implementation of several aerial manipulators prototypes, which have been tested in real outdoor scenariosto grasp objects and perform structural inspection. Solving the hardware and software architecture problems of these systems. The dynamics model of the whole systems have been also obtained and controllers have been proposed and validated.

This thesis has been completed in the framework European Projects as ARCAS, AEROBI and AEROARMS. Helping and advancing in the development of the aerial manipulator technology.

5.2 Future works

In the future, the main goal of the aerial manipulator systems should be achieving that these aerial robots become in fully autonomous systems. To accomplish this task becomes necessary to lighten the hardware, and moreover the use of accuracy and speed sensors. For example, the autopilot used in AMUSE had a weight of 750 gr. while the GRVC autopilot described in Appendix has a weight of about 150 gr or comparing the Novatel GPS-RTK weight used in AMUSE (about 500 gr.) with the new Emlid Reach plus (about 50 gr.). With these changes we could improve significantly the time flight of the platform. The data frequency of the sensors is also needed to obtain a good state estimation and thus improving the loop control. For example, the Novatel GPS-RTK has 10 Hz while the Emlid Reach plus has 14 Hz. The use of these new hardware should improve the results obtained with AMUSE. Other pending work is the more integration of visual servoing for the AMUSE case to improve the repeatability of the experiments and increase the dexterity of the full system. The use of a platform like the presented in the chapter 4 section 2 should also improve the behavior of the system, moreover including a force sensor to increase the safety in contact operations and furthermore decreasing the crashes or collisions.

In the compliant aerial manipulator case, the use of variable stiffness actuators will improve the accuracy, robustness and reliability of the manipulator system. Furthermore the implementation of an aerial platform with the same configuration but with smaller size could improve the capabilities in bridge inspection due to the increment of the system manoeuvrability. Another improvement will consist of the development of a positioning system based not just in the Total Station but also in vision, including a stereo camera system.

In the case of the ARBI system, the next step is the use of the Leica Total Station to obtain a 3D map of the structure or bridge and the development of a software which the inspectors could choose the points in the bridge where take measurements. Then, these points should be communicated to the aerial platform for the generation of the trajectory for the inspection. Adding a vision system, the inspectors could have more information about structural health.

Appendix A

A.1 Rigid Body Motions

The kinematics of a robot gives the relationship between each degrees of freedom (DOF) of the system and the motion of rigid bodies which form the system. In this thesis, the **Special Euclidean group** $SE(3)$, or the group of rigid-body motions have been considered to represent the orientation and position of a rigid body in a combined form. The $SE(3)$ is defined as the set of all 4×4 real matrices, g defined as,

$$g = \begin{bmatrix} R & p \\ 0 & 1 \end{bmatrix} \tag{A.1}$$

where $R \in SO(3)$ and $p \in \mathbb{R}^3$ represent the rotation and position respectively. A matrix $g \in SE(3)$ is also called a homogeneous transformation matrix and it can also denoted by (p, R). The homogeneous transformation matrices are commonly used to represent the configuration of a rigid body, to change the reference frame in which a vector or frame is represented and to displace a vector or a frame.

A.1.1 Twists

Now, it is needed to calculate the twist, ξ_i, for each joint which corresponds to screw motion for the ith joint with all other joint held fixed at zero. For a revolute joint,

the twist ,ξ_i has the form

$$\xi_i = \begin{bmatrix} -\omega_i \times q_i \\ \omega_i \end{bmatrix} \tag{A.2}$$

where $\omega_i \in \mathbb{R}^3$ is a unit vector in the direction of the twist axis and $q_i \in \mathbb{R}^3$ is any point on the axis. For a prismatic joint,

$$\xi_i = \begin{bmatrix} v_i \\ 0 \end{bmatrix} \tag{A.3}$$

where $v_i \in \mathbb{R}^3$ is a unit vector pointing in the direction of translation.

A.1.2 The product of exponentials formula

The product of exponentials formula (Murray, 2017) has been a method used to describe the kinematics of several aerial manipulators studied during this thesis. The product of exponentials formula provides a geometric description of the kinematics leveraging that the motion of a joint is generated by a twist associated with the joint axis. Let define ξ as a twist, then the rigid motion related with rotating and translating along the axis of the twist is given by

$$g_{ab}(\theta) = e^{\hat{\xi}\theta} g_{ab}(0) \tag{A.4}$$

where $\theta \in \mathbb{R}$ represents the amount of translation if ξ is a prismatic joint and however $\theta \in \mathbb{S}^1$ is the angle of rotation about the axis if ξ is a rotation joint.

A.2 Kinematics of an aerial manipulator

First of all, it is necessary to define the frames of the system. In the case of an open-chain robot manipulator, we must define at least a reference frame fixed to the base of the robot (first link) and a frame in the tool or end-effector of the manipulator (last link). An aerial manipulator is defined as an aerial vehicle equipped with one or multiple robots manipulators. In the case of multiple arms, the forward kinematics

must be calculated for each arms. Therefore, we must define at least an inertial reference frame, S, an aerial vehicle body frame, B_0, attached to its center of mass or to the geometric center of the vehicle and, finally, both the frames in each arm's base, $B_i(i = 1, ..., k)$, and the frames, $E_i(i = 1, ..., k)$, attached to each end-effector of the k robots manipulators composing the system (see Figure A.1). Furthermore, the aerial vehicle will be considered as a six DOF joint (three for translation and three for rotation) and each arms as an open-chain manipulator. Then, analyzing the system's joint coordinates, an aerial manipulator will have three translation joints, $p = (x, y, z)^T \in \mathbb{R}^3$, and three revolute joints, $\eta = (\phi, \theta, \psi)^T \in \mathbb{R}^3$, which represent the six DoF of the aerial vehicle plus the joints of each robot manipulator, $\gamma^i = (\gamma_1^i, ..., \gamma_{r_i}^i) \in \mathbb{R}^{r_i}(i = 1, ..., k)$. Thus, the system's joint coordinates is given by

$$\varphi = (p, \eta, \gamma^1, ..., \gamma^k) \in \mathbb{R}^N \; with \; N = 6 + \sum_{i=1}^{k} r_i \tag{A.5}$$

To simplify the notation in the following equations, we will use φ_n $(n = 1, ..., N)$ to refer us a specific joint of φ where the index i represents the position of the joint in the coordinates' vector, for example, $\varphi_3 = z$ or $\varphi_6 = \psi$ and $\varphi_9 = \gamma_3^1$. Now, we can define $\dot{p}$ as the absolute linear velocity of the aerial platform w.r.t. the inertial frame S, and it is given by,

$$\dot{p} = R(\eta)\dot{p}_{B_0} \tag{A.6}$$

where $R(\eta) \in SO(3)$ is a rotation matrix and $\dot{p}_{B_0}$ describes the linear velocity of the aerial platform w.r.t to the frame B_0. On the other hand, the absolute rotational velocity, ω, can be calculated as

$$\omega = T(\eta)\dot{\eta} \tag{A.7}$$

where $T(\eta) \in \mathbb{R}^{3\times3}$ is a transformation matrix between the time derivative of η and ω. Following the proceeding shown in (Lippiello and Ruggiero, 2012) and (Siciliano et al., 2010), The direct kinematics for an aerial vehicle is defined by the Homogeneous Transformation matrix presented in A.1,

$$g_{sb_0} == \begin{bmatrix} R(\eta) & p \\ 0 & 1 \end{bmatrix} \tag{A.8}$$

And transformation matrix for each arm of the aerial manipulator system w.r.t to B_0 can be obtained in the form,

$$g_{b_0 e_k} == \begin{bmatrix} n_{e_k}(\gamma) & s_{e_k}(\gamma) & a_{e_k}(\gamma) & p_{e_k}(\gamma) \\ 0 & 0 & 0 & 1 \end{bmatrix} \tag{A.9}$$

with n_{e_k}, s_{e_k}, a_{e_k} and p_{e_k} are the unit vectors of the frame attached to the k-th end-effector. Then, the pose of the k-th manipulator w.r.t the inertial frame S is given by

$$g_{se_k}(\varphi) = g_{sb_0} g_{b_0 e_k} \tag{A.10}$$

Now, if we define the position and orientation of the k-th end effector as x_{e_k}, then x_{e_k} can be calculated through a function $f(\varphi)$ and the kinematic can be also written as

$$x_{e_k} = f(\varphi) \tag{A.11}$$

and the Jacobian, J, can be calculated via differentiation of $f(\varphi)$ and the linear mapping between time derivative of x_{e_k} and $\dot{\varphi}$ is given by

$$\dot{x}_{e_k} = J\dot{\varphi} \tag{A.12}$$

A.2.1 Kinematics using POE

To derive the kinematics of a robot, other method widely used is the Product of Exponentials (POE). This method was introduced in (Brockett, 1984) and presents several advantages such as, for instances, to allow an uniform treatment of rotation and prismatic joints (Lynch and Park, 2017) and to process by computer easier,(Murray, 2017).

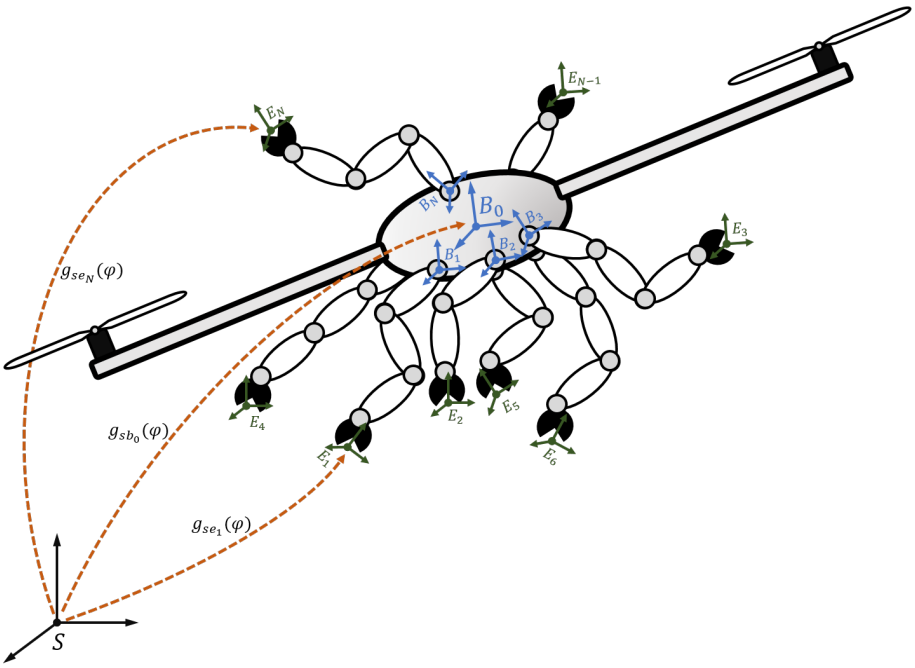

Figure A.1: Definition frames

A first step in POE method is to determinate the kinematic configuration,$g_{se} \in SE(3)$, of the end-effector when the joint coordinates are in a zero position relative to the inertial frame, S. Note that, in the multiple arm's case, we must establish it for each arm, $g_{se_i}(0) \in SE(3)$ $(i = 1, ..., k)$. Then, we must construct each twist, ξ_n $(n = 1, ..., N)$ for the joints of each manipulator (see A.1). Finally, the forward kinematics map for each manipulator is given by the combination of each robot arm's joint motions plus the aerial platform's joint motions and they can be expressed as

$$
\begin{aligned}
g_{se_i}(\varphi) &= e^{\hat{\xi}_x x} e^{\hat{\xi}_y y} e^{\hat{\xi}_z z} e^{\hat{\xi}_\phi \phi} e^{\hat{\xi}_\theta \theta} e^{\hat{\xi}_\psi \psi} e^{\hat{\xi}_{\gamma_1^i} \gamma_1^i} ... e^{\hat{\xi}_{\gamma_{r_i}^i} \gamma_{r_i}^i} g_{se_i}(0) \ \in \ SE(3) \ (i = 1, ..., k) \\
g_{se_i}(\varphi) &= (\prod_{n=1}^{6} e^{\hat{\xi}_n \varphi_n})(\prod_{n=7}^{N} \alpha_{i,n}) g_{se_i}(0) \ \in \ SE(3) \ (i = 1, ..., r_i)
\end{aligned}
\tag{A.13}
$$

where the function $\alpha_{i,n} \in SE(3)$ is defined as

$$\alpha_{i,n} = \begin{cases} e^{\hat{\xi}_n \varphi_n} & if\ \varphi_n \in \gamma^i \\ I_{4\times4} & if\ \varphi_n \notin \gamma^i \end{cases} \tag{A.14}$$

Herein $I_{4\times4} \in \mathbb{R}^{4\times4}$ represents an identity matrix. Note that, these equations are true if and only if $B_0 = B_i$ $(i = 1, ..., k)$. Otherwise, the transformation matrices for the relationship between B_0 and the manipulators' bases frame B_i must be included for each forward kinematics. Each equation represents in A.13 is called the product of exponentials formula for each arm forward kinematics of the aerial manipulator (see A.1). Using, this method is also possible to obtain the kinematics relationship between the end-effector of two manipulators. One advantage in the use of the POE is the possibility of obtain both the spatial and body manipulator Jacobian in a more explicit and elegant formulas.Then, the spatial body Jacobian for the ith end-effector of the aerial manipulator is given by:

$$J^s_{se_i}(\varphi) = [\xi_1 \ldots \xi_6\ \xi'_{i,n} \ldots \xi'_{i,r_i}] \tag{A.15}$$

with

$$\xi'_{i,j} = Ad_{(e^{\hat{\xi}_1\varphi_1}\ldots e^{\hat{\xi}_6\varphi_6} e^{\hat{\xi}_n\varphi_n}\ldots e^{\hat{\xi}_{j-1}\varphi_{j-1}} e^{\hat{\xi}_j\varphi_j})}\xi_j \tag{A.16}$$

where $Ad \in \mathbb{R}^{6\times6}$ is the adjoint transformation and is given by

$$Ad_g = \begin{bmatrix} R & \hat{p}R \\ 0 & R \end{bmatrix} \tag{A.17}$$

Then, the inverse of Ad can be calculated as

$$Ad_g^{-1} = \begin{bmatrix} R^T & -R^T\hat{p} \\ 0 & R^T \end{bmatrix} \tag{A.18}$$

Using A.17 it is also possible to calculate the body manipulator Jacobian for the ith end-effector of the aerial manipulator as,

$$J^b_{se_i}(\varphi) = [\xi^\dagger_1 \dots \xi^\dagger_6 \, \xi^\dagger_{i,n} \dots \xi^\dagger_{i,r_i}] \tag{A.19}$$

with

$$\xi^\dagger_{i,j} = Ad^{-1}_{(e^{\hat{\xi}_{\varphi(j)}\varphi(j)} e^{\hat{\xi}_{\varphi(j+1)}\varphi(j+1)} \dots e^{\hat{\xi}_{\varphi(r_i)}\varphi(r_i)})} \xi_{\varphi_j} \tag{A.20}$$

The columns of J correspond to the joint twist written with respect to the tool frame at the current configuration. The spatial and the body Jacobian are related by an adjoint transformation:

$$J^s_{se_i}(\varphi) = Ad_{g_{se_i}(\varphi)} J^b_{se_i}(\varphi) \tag{A.21}$$

A.2.2 Example: kinematics of a 2 DOF arm aerial manipulator using POE

Now, consider the aerial manipulator shown in Figure A.2. It consists of an aerial vehicle equipped with a robotic arm. In this case, the manipulator is composed by two revolute joints. The aerial vehicle frame and the manipulator's base frame are coincident.

Then, the coordinate joints vector is given by $\varphi = (x, y, z, \phi, \theta, \psi, \gamma_1, \gamma_2)^T \in \mathbb{R}^8$ and when the system is in a zero position, $\varphi = 0$, the homogeneous transformation matrix between the inertial frame and the end-effector frame is given by

$$g_{se}(\varphi) = \begin{bmatrix} I & p(0) \\ 0 & 1 \end{bmatrix}, \qquad p(0) = \begin{bmatrix} 0 \\ 0 \\ -l_1 - l_2 \end{bmatrix} \tag{A.22}$$

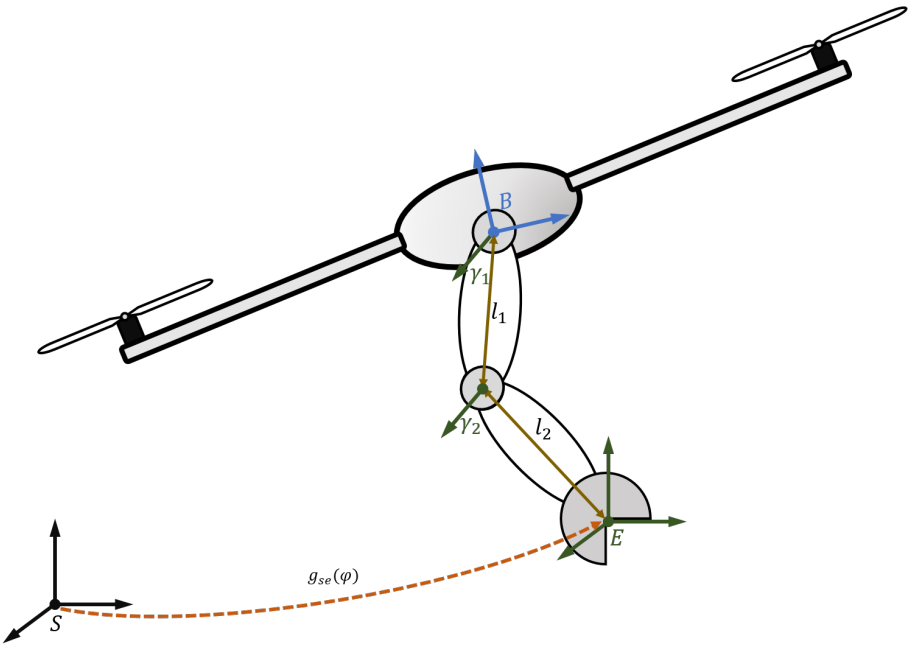

Figure A.2: Aerial manipulator with 2 DOF arm

wherein $I \in \mathbb{R}^{3\times3}$ is an identity matrix. Now, we construct the twist for the aerial vehicle, for instance, note that

$$\omega_\phi = \begin{bmatrix}1\\0\\0\end{bmatrix}, \omega_\theta = \begin{bmatrix}0\\1\\0\end{bmatrix}, \omega_\psi = \begin{bmatrix}0\\0\\1\end{bmatrix}, q_\phi = q_\theta = q_\psi = \begin{bmatrix}0\\0\\0\end{bmatrix}, v_x = \begin{bmatrix}1\\0\\0\end{bmatrix}, v_y = \begin{bmatrix}0\\1\\0\end{bmatrix}, v_z = \begin{bmatrix}0\\0\\1\end{bmatrix} \tag{A.23}$$

We assume the origin $(0, 0, 0)$ as axis point for the three orientation joints. That way, we define the aerial vehicle as a one rigid body with six DOF. Then, the twists for the

aerial vehicle are given by

$$\xi_x = \begin{bmatrix} 0 \\ 0 \\ 0 \\ 1 \\ 0 \\ 0 \end{bmatrix}, \quad \xi_y = \begin{bmatrix} 0 \\ 0 \\ 0 \\ 0 \\ 1 \\ 0 \end{bmatrix}, \quad \xi_z = \begin{bmatrix} 0 \\ 0 \\ 0 \\ 0 \\ 0 \\ 1 \end{bmatrix} \quad \xi_\phi = \begin{bmatrix} 1 \\ 0 \\ 0 \\ 0 \\ 0 \\ 0 \end{bmatrix} \quad \xi_\theta = \begin{bmatrix} 0 \\ 1 \\ 0 \\ 0 \\ 0 \\ 0 \end{bmatrix} \quad \xi_\psi = \begin{bmatrix} 0 \\ 0 \\ 1 \\ 0 \\ 0 \\ 0 \end{bmatrix} \tag{A.24}$$

Next step is obtain the twists of each manpulator's joint as following

$$\xi_{\gamma_1} = \begin{bmatrix} 0 \\ 0 \\ 0 \\ 0 \\ -1 \\ 0 \end{bmatrix}, \quad \xi_{\gamma 2} = \begin{bmatrix} l_1 \\ 0 \\ 0 \\ 0 \\ 1 \\ 0 \end{bmatrix} \tag{A.25}$$

Now, it is possible to apply POE method to obtain the forward kinematics for the end-effector. Note that, to define the orientation of the aerial vehicle, we choose a XYZ configuration,

$$g_{se}(\varphi) = e^{\hat{\xi}_x x} e^{\hat{\xi}_y y} e^{\hat{\xi}_z z} e^{\hat{\xi}_\phi \phi} e^{\hat{\xi}_\theta \theta} e^{\hat{\xi}_\psi \psi} e^{\hat{\xi}_{\gamma_1} \gamma_1} e^{\hat{\xi}_{\gamma_2} \gamma_2} g_{se}(0) \tag{A.26}$$

Analyzing the homogeneous transformation matrix resulted, we have obtained,

$$g_{se}(\varphi) = \begin{bmatrix} R(\phi, \theta, \phi) R(\gamma_1, \gamma_2) & p(x, y, z) + R(\phi, \theta, \phi) p(\gamma_1, \gamma_2) \\ 0 & 1 \end{bmatrix} \tag{A.27}$$

with

$$p(x,y,z) = \begin{bmatrix} x \\ y \\ z \end{bmatrix}, \qquad p(\gamma_1,\gamma_2) = \begin{bmatrix} l_1 sin(\gamma_1) + l_2 sin(\gamma_1 - \gamma_2) \\ 0 \\ -l_1 cos(\gamma_1) - l_2 cos(\gamma_1 - \gamma_2) \end{bmatrix} \tag{A.28}$$

where $R(\phi,\theta,\phi) \in SO(3)$ is the rotation matrix of the aerial vehicle in XYZ configuration and has the form

$$R(\phi,\theta,\phi) = \begin{bmatrix} cos(\psi)cos(\theta) & -sin(\psi)cos(\theta) & sin(\theta) \\ cos(\phi)sin(\psi) + cos(\psi)sin(\phi)sin(\theta) & cos(\phi)cos(\psi) - sin(\psi)sin(\phi)sin(\theta) & -sin(\phi)cos(\theta) \\ sin(\phi)cos(\psi) - cos(\psi)cos(\phi)sin(\theta) & cos(\phi)sin(\psi) + sin(\psi)cos(\phi)sin(\theta) & cos(\phi)cos(\theta) \end{bmatrix} \tag{A.29}$$

The term $R(\gamma_1,\gamma_2) \in SO(3)$ is the rotation matrix of the manipulator and is given by

$$R(\gamma_1,\gamma_2) = \begin{bmatrix} cos(\gamma_1 - \gamma_2) & 0 & -sin(\gamma_1 - \gamma_2) \\ 0 & 1 & 0 \\ sin(\gamma_1 - \gamma_2) & 0 & cos(\gamma_1 - \gamma_2) \end{bmatrix} \tag{A.30}$$

A.2.3 Kinematics using Denavit-Hartenberg

The Denavit-Hartenberg (DH) convention is commonly used in robotics applications for selecting frames references. In this convection, the homogeneous transformation matrix A.1 for each frame is obtained by four transformation parameters (DH parameters), which quantities are represented by θ_i, a_i, d_i and α_i. The names generally associated to these parameters are link length, link twist, link offset, and joint angle, respectively (Spong et al., 2006). An algorithm to define these parameters for each frame of a robot is presented in (Baturone, 2005). Using these parameter, the transformation matrix relating the frame i w.r.t. the frame $i-1$ is given by:

$$g_{i-1,i} = \begin{bmatrix} cos(\theta_i) & -sin(\theta_i)cos(\alpha_i) & sin(\theta_i)sin(\alpha_i) & a_i cos(\theta_i) \\ sin(\theta_i) & cos(\theta_i)cos(\alpha_i) & -cos(\theta_i)sin(\alpha_i) & a_i sin(\theta_i) \\ 0 & sin(\alpha_i) & sin(\alpha_i) & d_i \\ 0 & 0 & & 1 \end{bmatrix} \tag{A.31}$$

Then, in the same way of POE method, the kinematics for an end-effector of the aerial manipulator system can be calculated as the product each transformation matrix:

$$g_{se}(\varphi) = g_{sb_0}(\varphi) g_{b_0 b_1}(\varphi) ... g_{b_{r_k} e}(\varphi) \tag{A.32}$$

The DH parameters can be related with the twist corresponding of each joint of a robotic system. A discussion about this relationship can be found in (Murray, 2017).

Appendix B

B.1 GRVC Autopilot

In robotic research field, the design of a theoretical control strategies can be as important as the implementation in a real system. To validate these theoretical control strategies, MATLAB/Simulink is widely used by the researchers due to the powerful of this software and their facilities to generate simulation environments. After testing the CATEC autopilot (see chapter 3 section 1), we decide to create our own autopilot system based on MATLAB/Simulink for the implementation of control strategies in real aerial robotic systems. It was named GRVC Autopilot. To facility its use inside the researcher community, we determinate to implement the system inside a commercial and cheaper devices like a Raspberry Pi 3B with a Navio 2 sensor cape. Raspberry Pi 3B is a powerful single-board computer developed in the United Kingdom by the Raspberry Pi Foundation. The main goal of this device is to promote the teaching of computer science the academic environment and it is widely used inside the researcher community. In the other hand, Navio 2 is a hat for Raspberry Pi, which providing the sensors and hardware needed to create an autopilot system. In fact, Ardupilot and PX4 have been adapted to run in this hardware. An example of the hardware architecture that could be implemented with the GRVC Autopilot can be seen in Figure B.1. This Figure shows as the GRVC autopilot can be connected with several sensors (PX4Flow, GPS, imu, lidars, etc), thanks to the ports enabled by the Navio (I2C, UART, ADC, etc.); with others computer boards, i.e. to implemented positioning systems based on cameras. Moreover, in an aerial

manipulation system case, the full control system can be executed inside the raspberry pi, avoiding communication delays or problems arising from the implementation of both controller systems (aerial platform and robotic arm) in detached devices.

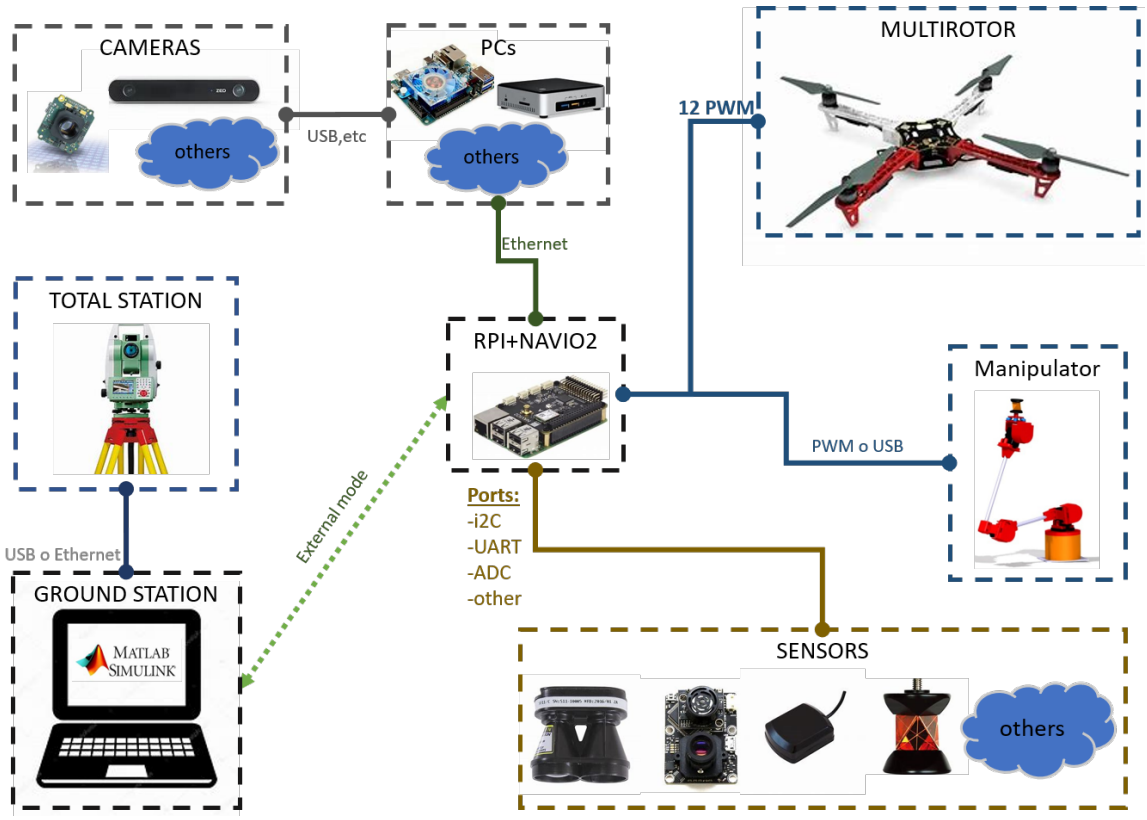

Figure B.1: Hardware scheme

B.1.1 A brief Software Description

The main idea inside the GRVC autopilot is to help the aerial robotic researchers to implement and test novel control strategies in real aerial platforms. In the GRVC autopilot, the developer can design the full control system in MATLAB/Simulink model. This Simulink model is compiled and charged inside the Raspberry Pi, and thanks to external mode, the model is can be used like a ground station with the advantages of modification gain parameters and visualization of data sensors and signals online when the system is running. To catch and communicate the sensors

data with the Simulink model, a Shared Memory Communication System (SHCS) has been designed. This is communication system based on POSIX shared memory. Thanks to SHCS the interface between the Simulink model and the other process can be carry out. A process called *bridge_navio* have been created to manage the communication between the different sensors used and the Simulink model. Moreover, *bridge_navio* is charged of the safety system. The PX4 estimator (EKF2) can be also used in the GRVC autopilot. A custom PX4 version can parallel run in the system to benefit the advantages of the EKF2. This custom PX4 version is communicated with the whole system thanks to the SHCS. A brief scheme of how the software works can be seen in Figure B.2.

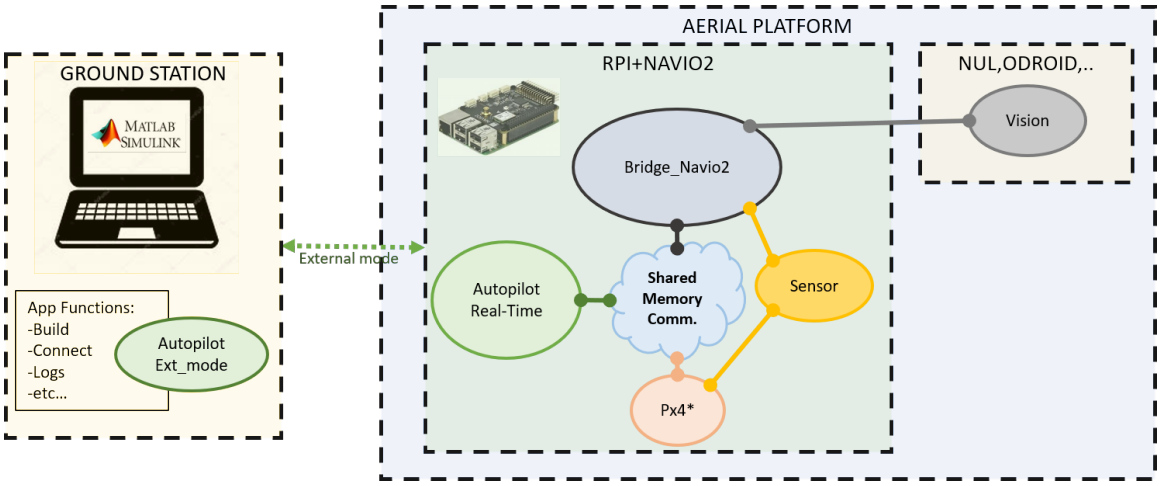

Figure B.2: Scheme of how the GRVC autopilot has been implemented.

An *app* using MATLAB GUI has been also developed facilitating users the control of the system. The Figure B.3 shows an example of a ground station developed with the GRVC autopilot system. In the left part of the figure, we can see the Simulink model implemented. This model has been used in the experiments shown in the chapter 4 section 3. The input and output interfaces remarked are communicated through SHCS with the *bridge_navio* process to catch the sensor data. And in the output case, to send the PWM signals to each rotor of the aerial platform. Moreover, the state of the system is also submitted to log the data inside the aerial platform and to visualize flight mode through the app. In the right part, we can see the *appAEROBI*

designed to control the process of this model. Each *appAEROBI* button launch a function of the system like: compile and charge, connect, start, etc.

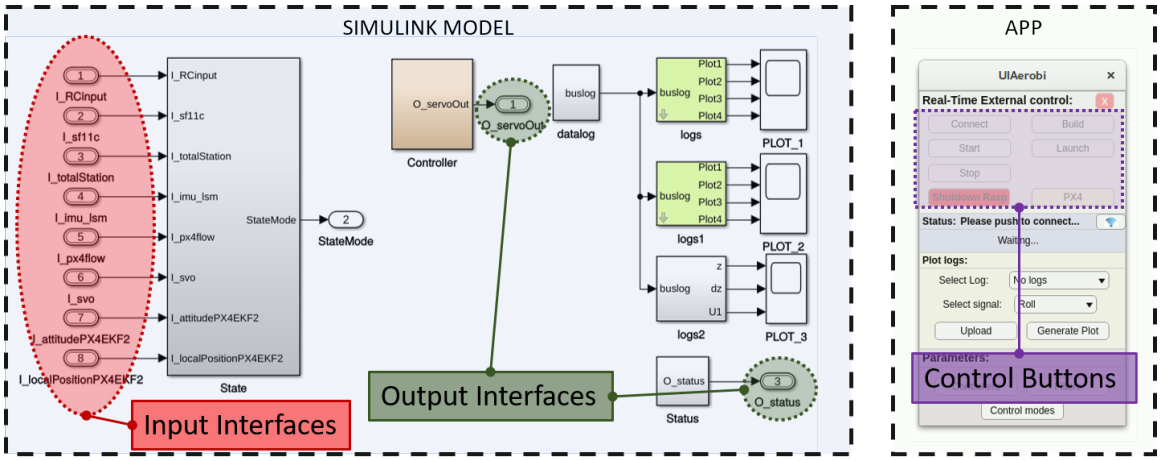

Figure B.3: Example of the GRVC autopilot ground station developed for AEROBI project.

Bibliography

AEROARMS-project (2016). Aerial robotic system integrating multiple arms and advanced manipulation capabilities for inspection and maintenance (aeroarms). https://aeroarms-project.eu/.

AEROBI-project (2016). Aerial robotic system for in-depth bridge inspection by contact (aerobi). http://www.aerobi.eu/.

AEROWORKS-project (2015). Collaborative aerial robotic workers. http://www.aeroworks2020.eu/.

Albu-Schaffer, A., Ott, C., and Hirzinger, G. (2005). Constructive energy shaping based impedance control for a class of underactuated euler-lagrange systems. In *Proceedings of the 2005 IEEE International Conference on Robotics and Automation*, pages 1387–1393. IEEE.

Amazon (2016). Amazon prime air. http://www.amazon.com/b?node=8037720011.

Antonelli, G., Cataldi, E., Giordano, P. R., Chiaverini, S., and Franchi, A. (2013). Experimental validation of a new adaptive control scheme for quadrotors mavs. In *2013 IEEE/RSJ International Conference on Intelligent Robots and Systems*, pages 2439–2444. IEEE.

ARCAS-project (2013). Aerial robotics cooperative assembly system (arcas). http://www.arcas-project.eu.

Backus, S. B., Odhner, L. U., and Dollar, A. M. (2014). Design of hands for aerial manipulation: Actuator number and routing for grasping and perching. In *2014*

IEEE/RSJ International Conference on Intelligent Robots and Systems, pages 34–40. IEEE.

Bartelds, T., Capra, A., Hamaza, S., Stramigioli, S., and Fumagalli, M. (2016). Compliant aerial manipulators: Toward a new generation of aerial robotic workers. *IEEE Robotics and Automation Letters*, 1(1):477–483.

Baturone, A. O. (2005). *Robótica: manipuladores y robots móviles.* Marcombo.

Bellens, S., De Schutter, J., and Bruyninckx, H. (2012). A hybrid pose/wrench control framework for quadrotor helicopters. In *2012 IEEE International Conference on Robotics and Automation*, pages 2269–2274. IEEE.

Bernard, M., Kondak, K., Maza, I., and Ollero, A. (2011). Autonomous transportation and deployment with aerial robots for search and rescue missions. *Journal of Field Robotics*, 28(6):914–931.

Bonvini, M. and Leva, A. (2011). Object-oriented sub-zonal modelling for efficient energy-related building simulation. *Mathematical and Computer Modelling of Dynamical Systems*, 17(6):543–559.

Bristeau, P.-J., Martin, P., Salaün, E., and Petit, N. (2009). The role of propeller aerodynamics in the model of a quadrotor uav. In *2009 European Control Conference (ECC)*, pages 683–688. IEEE.

Brockett, R. W. (1984). Robotic manipulators and the product of exponentials formula. In *Mathematical theory of networks and systems*, pages 120–129. Springer.

Cano, R., Pérez, C., Pruano, F., Ollero, A., and Heredia, G. (2013). Mechanical design of a 6-dof aerial manipulator for assembling bar structures using uavs. In *2nd RED-UAS 2013 workshop on research, education and development of unmanned aerial systems.*

Cheeseman, I. and Bennett, W. (1957). The effect of the ground on a helicopter rotor. *R and M*, 3021.

Chen, Q.-Z., Mo, Y.-F., and Meng, G. (2006). Dymola-based modeling of srd in aircraft electrical system. *IEEE transactions on aerospace and electronic systems*, 42(1):220–227.

Chiacchio, P., Chiaverini, S., Sciavicco, L., and Siciliano, B. (1991). Closed-loop inverse kinematics schemes for constrained redundant manipulators with task space augmentation and task priority strategy. *The International Journal of Robotics Research*, 10(4):410–425.

Chmaj, G., Buratowski, T., Uhl, T., Sewerin, K., Banaszkiewicz, M., and Sasiadek, J. (2013). The dynamics influence of the attached manipulator on uav. In *Aerospace Robotics*.

Cruz, P. and Fierro, R. (2014). Autonomous lift of a cable-suspended load by an unmanned aerial robot. In *2014 IEEE Conference on Control Applications (CCA)*, pages 802–807. IEEE.

Danko, T. W., Chaney, K. P., and Oh, P. Y. (2015). A parallel manipulator for mobile manipulating uavs. In *2015 IEEE international conference on technologies for practical robot applications (TePRA)*, pages 1–6. IEEE.

Darivianakis, G., Alexis, K., Burri, M., and Siegwart, R. (2014). Hybrid predictive control for aerial robotic physical interaction towards inspection operations. In *2014 IEEE International Conference on Robotics and Automation (ICRA)*, pages 53–58. IEEE.

Delgado, J. P., Soria, P. R., Arrue, B. C., and Ollero, A. (2017). Bridge mapping for inspection using an uav assisted by a total station. In *Iberian Robotics conference*, pages 309–319. Springer.

Diolaiti, N., Melchiorri, C., and Stramigioli, S. (2005). Contact impedance estimation for robotic systems. *IEEE Transactions on Robotics*, 21(5):925–935.

Elmqvist, H., Mattsson, S. E., and Otter, M. (1999). Modelica-a language for physical system modeling, visualization and interaction. In *Proceedings of the 1999*

IEEE international symposium on computer aided control system design (Cat. No. 99TH8404), pages 630–639. IEEE.

Featherstone, R. (2014). *Rigid body dynamics algorithms*. Springer.

Fink, J., Michael, N., Kim, S., and Kumar, V. (2011). Planning and control for cooperative manipulation and transportation with aerial robots. *The International Journal of Robotics Research*, 30(3):324–334.

for Robotics in Europe, T. P. (2013). The strategic research agenda. `http://roboproject.h2214467.stratoserver.net/cms/upload/PPP/SRA2020_SPARC.pdf`.

Forte, F., Naldi, R., Macchelli, A., and Marconi, L. (2012). Impedance control of an aerial manipulator. In *2012 American Control Conference (ACC)*, pages 3839–3844. IEEE.

Fumagalli, M., Naldi, R., Macchelli, A., Carloni, R., Stramigioli, S., and Marconi, L. (2012). Modeling and control of a flying robot for contact inspection. In *2012 IEEE/RSJ International Conference on Intelligent Robots and Systems*, pages 3532–3537. IEEE.

GeoSocial (2014). Geosocial science and media. `http://www.geosocial.net/?p=829`.

Hara, N., Handa, Y., and Nenchev, D. (2012). End-link dynamics of redundant robotic limbs: The reaction null space approach. In *2012 IEEE International Conference on Robotics and Automation*, pages 299–304. IEEE.

Heredia, G., Jimenez-Cano, A., Sanchez, I., Llorente, D., Vega, V., Braga, J., Acosta, J., and Ollero, A. (2014). Control of a multirotor outdoor aerial manipulator. In *2014 IEEE/RSJ International Conference on Intelligent Robots and Systems*, pages 3417–3422. IEEE.

Huber, F., Kondak, K., Krieger, K., Sommer, D., Schwarzbach, M., Laiacker, M., Kossyk, I., Parusel, S., Haddadin, S., and Albu-Schäffer, A. (2013). First analysis

and experiments in aerial manipulation using fully actuated redundant robot arm. In *2013 IEEE/RSJ International Conference on Intelligent Robots and Systems*, pages 3452–3457. IEEE.

HYFLIERS-project (2018). Hybrid flying-rolling with-snake-arm robot for contact inspection (hyfliers). `https://www.oulu.fi/hyfliers/`.

Jiang, Q. and Kumar, V. (2013). The inverse kinematics of cooperative transport with multiple aerial robots. *IEEE Transactions on Robotics*, 29(1):136–145.

Jimenez-Cano, A., Braga, J., Heredia, G., and Ollero, A. (2015). Aerial manipulator for structure inspection by contact from the underside. In *2015 IEEE/RSJ international conference on intelligent robots and systems (IROS)*, pages 1879–1884. IEEE.

Jimenez-Cano, A., Heredia, G., Bejar, M., Kondak, K., and Ollero, A. (2016). Modelling and control of an aerial manipulator consisting of an autonomous helicopter equipped with a multi-link robotic arm. *Proceedings of the Institution of Mechanical Engineers, Part G: Journal of Aerospace Engineering*, 230(10):1860–1870.

Jimenez-Cano, A., Martin, J., Heredia, G., Ollero, A., and Cano, R. (2013). Control of an aerial robot with multi-link arm for assembly tasks. In *2013 IEEE International Conference on Robotics and Automation*, pages 4916–4921. IEEE.

Jimenez-Cano, Antonio, S.-C. P. G. P., Heredia, G., and Ollero, A. (2019). Contact-based bridge inspection multirotors: Design, modelling and control considering the ceiling effect. *Robotic and Automation Letter*, 2019.

Kane, T. R. and Levinson, D. A. (1985). *Dynamics, theory and applications*. McGraw Hill.

Kane, T. R., Likins, P. W., and Levinson, D. A. (1983). Spacecraft dynamics. *New York, McGraw-Hill Book Co, 1983, 445 p.*

Kannan, S., Olivares-Mendez, M. A., and Voos, H. (2013). Modeling and control of aerial manipulation vehicle with visual sensor. *IFAC Proceedings Volumes*, 46(30):303–309.

Kemper, M. and Fatikow, S. (2006). Impact of center of gravity in quadrotor helicopter controller design. *IFAC Proceedings Volumes*, 39(16):157–162.

Khatib, O. (1987). A unified approach for motion and force control of robot manipulators: The operational space formulation. *IEEE Journal on Robotics and Automation*, 3(1):43–53.

Kim, S., Choi, S., and Kim, H. J. (2013). Aerial manipulation using a quadrotor with a two dof robotic arm. In *2013 IEEE/RSJ International Conference on Intelligent Robots and Systems*, pages 4990–4995. IEEE.

Kondak, K., Krieger, K., Albu-Schaeffer, A., Schwarzbach, M., Laiacker, M., Maza, I., Rodriguez-Castano, A., and Ollero, A. (2013). Closed-loop behavior of an autonomous helicopter equipped with a robotic arm for aerial manipulation tasks. *International Journal of Advanced Robotic Systems*, 10(2):145.

Korpela, C. M., Danko, T. W., and Oh, P. Y. (2012). Mm-uav: Mobile manipulating unmanned aerial vehicle. *Journal of Intelligent & Robotic Systems*, 65(1-4):93–101.

Leica (2019). Leica geosystems ag - part of hexagon. `https://leica-geosystems.com/`.

Li, M., Wang, Y., Li, F., Li, H., and Meng, G. (2013). Modelica-based object-orient modeling of rotor system with multi-faults. *Chinese Journal of Mechanical Engineering*, 26(6):1169–1181.

Lindsey, Q., Mellinger, D., and Kumar, V. (2011). Construction of cubic structures with quadrotor teams. *Proc. Robotics: Science & Systems VII*.

Lippiello, V., Mebarki, R., and Ruggiero, F. (2013). Visual coordinated landing of a uav on a mobile robot manipulator. In *2013 IEEE International Symposium on Safety, Security, and Rescue Robotics (SSRR)*, pages 1–7. IEEE.

Lippiello, V. and Ruggiero, F. (2012). Cartesian impedance control of a uav with a robotic arm. *IFAC Proceedings Volumes*, 45(22):704–709.

Lippiello, V. and Ruggiero, F. (2012). Exploiting redundancy in cartesian impedance control of uavs equipped with a robotic arm. In *2012 IEEE/RSJ International Conference on Intelligent Robots and Systems*, pages 3768–3773. IEEE.

Lynch, K. M. and Park, F. C. (2017). *Modern Robotics*. Cambridge University Press.

Mattino, I. (2014). Il mattino benevento. `http://www.ilmattino.itBENEVENTO/benevento-drone-cerreto-sannita/notizie/1122700.shtml`.

Mellinger, D., Lindsey, Q., Shomin, M., and Kumar, V. (2011). Design, modeling, estimation and control for aerial grasping and manipulation. In *2011 IEEE/RSJ International Conference on Intelligent Robots and Systems*, pages 2668–2673. IEEE.

Mellinger, D., Shomin, M., Michael, N., and Kumar, V. (2013). Cooperative grasping and transport using multiple quadrotors. In *Distributed autonomous robotic systems*, pages 545–558. Springer.

Mersha, A. Y., Stramigioli, S., and Carloni, R. (2014). Exploiting the dynamics of a robotic manipulator for control of uavs. In *2014 IEEE International Conference on Robotics and Automation (ICRA)*, pages 1741–1746. IEEE.

Michael, N., Fink, J., and Kumar, V. (2011). Cooperative manipulation and transportation with aerial robots. *Autonomous Robots*, 30(1):73–86.

Munoz-Salinas, R. (2012). Aruco: a minimal library for augmented reality applications based on opencv. *Universidad de Córdoba*.

Murray, R. M. (2017). *A mathematical introduction to robotic manipulation*. CRC press.

Nandakumar, G., Srinivasan, A., and Thondiyath, A. (2018). Theoretical and experimental investigations on the effect of overlap and offset on the design of a novel quadrotor configuration, voops. *Journal of Intelligent & Robotic Systems*, pages 1–14.

Nguyen, H.-N., Ha, C., and Lee, D. (2015). Mechanics, control and internal dynamics of quadrotor tool operation. *Automatica*, 61:289–301.

Nguyen, H.-N. and Lee, D. (2013). Hybrid force/motion control and internal dynamics of quadrotors for tool operation. In *2013 IEEE/RSJ International Conference on Intelligent Robots and Systems*, pages 3458–3464. IEEE.

Nikou, A., Gavridis, G. C., and Kyriakopoulos, K. J. (2015). Mechanical design, modelling and control of a novel aerial manipulator. In *2015 IEEE International Conference on Robotics and Automation (ICRA)*, pages 4698–4703. IEEE.

Orsag, M., Korpela, C., and Oh, P. (2013). Modeling and control of mm-uav: Mobile manipulating unmanned aerial vehicle. *Journal of Intelligent & Robotic Systems*, 69(1-4):227–240.

Palunko, I. and Fierro, R. (2011). Adaptive control of a quadrotor with dynamic changes in the center of gravity. *IFAC Proceedings Volumes*, 44(1):2626–2631.

Palunko, Ivana; Cruz, P. F. R. (2012). Agile load transportation: Safe and efficient load manipulation with aerial robots. *IEEE robotics and automation magazine*, 19(3):69–79.

Papachristos, C., Alexis, K., and Tzes, A. (2014). Efficient force exertion for aerial robotic manipulation: Exploiting the thrust-vectoring authority of a tri-tiltrotor uav. In *2014 IEEE International Conference on Robotics and Automation (ICRA)*, pages 4500–4505. IEEE.

Papadopoulos, E. and Moosavian, S. A. A. (1994). Dynamics and control of space free-flyers with multiple manipulators. *Advanced robotics*, 9(6):603–624.

Papadopoulos, E. G. (1990). *On the dynamics and control of space manipulators*. PhD thesis, Massachusetts Institute of Technology.

Park, J. and Khatib, O. (2005). Multi-link multi-contact force control for manipulators. In *Proceedings of the 2005 IEEE International Conference on Robotics and Automation*, pages 3613–3618. IEEE.

Pounds, P. E., Bersak, D. R., and Dollar, A. M. (2011). Grasping from the air: Hovering capture and load stability. In *2011 IEEE international conference on robotics and automation*, pages 2491–2498. IEEE.

Pounds, P. E., Bersak, D. R., and Dollar, A. M. (2012). Stability of small-scale uav helicopters and quadrotors with added payload mass under pid control. *Autonomous Robots*, 33(1-2):129–142.

Pulecchi, T., Casella, F., and Lovera, M. (2010). Object-oriented modelling for spacecraft dynamics: Tools and applications. *Simulation Modelling Practice and Theory*, 18(1):63–86.

Quigley, M., Conley, K., Gerkey, B., Faust, J., Foote, T., Leibs, J., Wheeler, R., and Ng, A. Y. (2009). Ros: an open-source robot operating system. In *ICRA workshop on open source software*, volume 3, page 5. Kobe, Japan.

Rajappa, S., Ryll, M., Bülthoff, H. H., and Franchi, A. (2015). Modeling, control and design optimization for a fully-actuated hexarotor aerial vehicle with tilted propellers. In *2015 IEEE International Conference on Robotics and Automation (ICRA)*, pages 4006–4013. IEEE.

Ruggiero, F., C. J. S. H. and Lippiello, V. (2015). Passivity-based control of vtol uavs with a momentum-based estimator of external wrench and unmodeled dynamics. *Robotics and Autonomous Systems*, 72(1):139–151.

Ruggiero, F., Lippiello, V., and Ollero, A. (2018). Aerial manipulation: A literature review. *IEEE Robotics and Automation Letters*, 3(3):1957–1964.

Ruggiero, F., Trujillo, M. A., Cano, R., Ascorbe, H., Viguria, A., Peréz, C., Lippiello, V., Ollero, A., and Siciliano, B. (2015). A multilayer control for multirotor uavs equipped with a servo robot arm. In *2015 IEEE international conference on robotics and automation (ICRA)*, pages 4014–4020. IEEE.

Sanchez, M. I., Acosta, J. A., and Ollero, A. (2015). Integral action in first-order closed-loop inverse kinematics. application to aerial manipulators. In *2015 IEEE*

International Conference on Robotics and Automation (ICRA), pages 5297–5302. IEEE.

Sanchez-Cuevas, P., Heredia, G., and Ollero, A. (2017a). Characterization of the aerodynamic ground effect and its influence in multirotor control. *International Journal of Aerospace Engineering*, 2017.

Sanchez-Cuevas, P., Heredia, G., and Ollero, A. (2017b). Multirotor uas for bridge inspection by contact using the ceiling effect. In *2017 International Conference on Unmanned Aircraft Systems (ICUAS)*, pages 767–774. IEEE.

Sandino, L. A., Bejar, M., and Ollero, A. (2011). On the applicability of linear control techniques for autonomous landing of helicopters on the deck of a ship. In *2011 IEEE international conference on mechatronics*, pages 363–368. IEEE.

Sandino, L. A., Santamaria, D., Bejar, M., Kondak, K., Viguria, A., and Ollero, A. (2016). First experimental results on enhancing hovering performance of unmanned helicopters by using a tethered setup. *Robotics and Autonomous Systems*, 79:147–155.

Siciliano, B. and Khatib, O. (2016). *Springer handbook of robotics*. Springer.

Siciliano, B., Sciavicco, L., Villani, L., and Oriolo, G. (2010). *Robotics: modelling, planning and control*. Springer Science & Business Media.

Spong, M. (1989). Modeling and control of elastic joint robots. *Mathematical and Computer Modelling*, 12(7):912.

Spong, M. W., Hutchinson, S., Vidyasagar, M., et al. (2006). *Robot modeling and control*.

Sreenath, K. and Kumar, V. (2013). Dynamics, control and planning for cooperative manipulation of payloads suspended by cables from multiple quadrotor robots. In *2013 Conference: Robotics: Science and Systems*. RSS Proceedings.

Stoneking, E. (2013). Implementation of kane's method for a spacecraft composed of multiple rigid bodies. In *AIAA Guidance, Navigation, and Control (GNC) Conference*, page 4649.

Suarez, A., Heredia, G., and Ollero, A. (2015). Lightweight compliant arm for aerial manipulation. In *2015 IEEE/RSJ International Conference on Intelligent Robots and Systems (IROS)*, pages 1627–1632. IEEE.

Suarez, A., Heredia, G., and Ollero, A. (2016). Compliant and lightweight anthropomorphic finger module for aerial manipulation and grasping. In *Robot 2015: Second Iberian Robotics Conference*, pages 543–555. Springer.

Suarez, A., Heredia, G., and Ollero, A. (2018a). Design of an anthropomorphic, compliant, and lightweight dual arm for aerial manipulation. *IEEE Access*, 6:29173–29189.

Suarez, A., Jimenez-Cano, A., Vega, V., Heredia, G., Rodriguez-Castano, A., and Ollero, A. (2017). Lightweight and human-size dual arm aerial manipulator. In *2017 International Conference on Unmanned Aircraft Systems (ICUAS)*, pages 1778–1784. IEEE.

Suarez, A., Jimenez-Cano, A., Vega, V., Heredia, G., Rodriguez-Castano, A., and Ollero, A. (2018b). Design of a lightweight dual arm system for aerial manipulation. *Mechatronics*, 50(10):30–44.

Suarez, A., Sanchez-Cuevas, P., Fernandez, M., Perez, M., Heredia, G., and Ollero, A. (2018c). Lightweight and compliant long reach aerial manipulator for inspection operations. In *2018 IEEE/RSJ International Conference on Intelligent Robots and Systems (IROS)*, pages 6746–6752. IEEE.

Tognon, M. and Franchi, A. (2017). Dynamics, control, and estimation for aerial robots tethered by cables or bars. *IEEE Transactions on Robotics*, 33(4):834–845.

Tognon, M., Testa, A., Rossi, E., and Franchi, A. (2016). Takeoff and landing on slopes via inclined hovering with a tethered aerial robot. In *2016 IEEE/RSJ International Conference on Intelligent Robots and Systems (IROS)*, pages 1702–1707. IEEE.

Tsukagoshi, H., Watanabe, M., Hamada, T., Ashlih, D., and Iizuka, R. (2015). Aerial manipulator with perching and door-opening capability. In *2015 IEEE International Conference on Robotics and Automation (ICRA)*, pages 4663–4668. IEEE.

Villani, L., Natale, C., Siciliano, B., and de Wit, C. C. (2000). An experimental study of adaptive force/position control algorithms for an industrial robot. *IEEE Transactions on Control Systems Technology*, 8(5):777–786.

Yüksel, B., Mahboubi, S., Secchi, C., Bülthoff, H. H., and Franchi, A. (2015). Design, identification and experimental testing of a light-weight flexible-joint arm for aerial physical interaction. In *2015 IEEE International Conference on Robotics and Automation (ICRA)*, pages 870–876. IEEE.